2014-12-08

Control Unit for an Opitcal Switch to Extend the Axial Range of a Spectral-Domain Optical Coherence Tomography System

Carolina P. de Freitas
University of Miami, caro.defreitas@gmail.com

UNIVERSITY OF MIAMI

CONTROL UNIT FOR AN OPTICAL SWITCH TO EXTEND THE AXIAL RANGE OF A SPECTRAL-DOMAIN OPTICAL COHERENCE TOMOGRAPHY SYSTEM

By

Carolina de Freitas

A THESIS

Submitted to the Faculty
of the University of Miami
in partial fulfillment of the requirements for
the degree of Master of Science

Coral Gables, Florida
December 2014

UNIVERSITY OF MIAMI

A thesis submitted in partial fulfillment of
the requirements for the degree of
Master of Science

CONTROL UNIT FOR AN OPTICAL SWITCH TO EXTEND THE AXIAL RANGE OF A SPECTRAL-DOMAIN OPTICAL COHERENCE TOMOGRAPHY SYSTEM

Carolina de Freitas

Approved:

_____
Marco Ruggeri, Ph.D.
Research Assistant Professor of
Ophthalmology

_____
Fabrice Manns, Ph.D.
Professor
Biomedical Engineering and
Ophthalmology

_____
Jean-Marie Parel, Ph.D.
Henri and Flore Lesieur Chair in
Ophthalmology, Research Associate
Professor of Ophthalmology and
Biomedical Engineering

_____
M. Brian Blake, Ph.D.
Dean of the Graduate School

_____
Jorge Bohorquez, Ph.D.
Associate Professor in
Practice of Biomedical Engineering

DE FREITAS, CAROLINA (M.S., Biomedical Engineering)

Control Unit for an Optical Switch to Extend the Axial Range of a Spectral-Domain Optical Coherence Tomography System (December 2014)

Abstract of a thesis at the University of Miami.

Thesis supervised by Professor Marco Ruggeri.
No. of pages in text. (109)

The goal of this thesis is to design and develop control electronics to integrate and synchronize a Spectral-Domain Optical Coherence Tomography (TD-OCT) system with an optical switch and an accommodation stimulus unit. The optical switch is implemented into the reference arm of the SD-OCT and is intended to change the length of the reference arm of the system after every frame-acquisition by a known distance. Combining consecutive frames into a single image can produce images with extended axial range while maintaining high axial and lateral resolution and high speed for *in vivo* imaging. The control unit also triggers a change in accommodation stimulus to the subject during imaging. In the implementation described, the range of the imaging device is extended to include the entire anterior segment and the retinal boundary. From these successive images, biometric measurements on the dynamic response of the eye to a step change in accommodation stimulus can be made.

This work is dedicated to my mother, Fatima Pestana, who has been steadfast and unwavering in her support and enthusiasm. Thanks, mom.

Acknowledgements

I would like to first and fore most extend my most sincere gratitude to my committee chair, Marco Ruggeri, Ph.D. This work would have been impossible without his guidance, instruction, and unending patience.

I would like to thank my supervisors, Jean-Marie Parel Ph.D. and Fabrice Manns Ph.D. for encouraging me and then providing the opportunity for me to pursue a Master's Degree in Biomedical Engineering through the Ophthalmic Biophysics Center (OBC) at Bascom Palmer Eye Institute while maintaining a full-time position. Dr. Parel and Dr. Manns have supported me with patience, guidance and dedication throughout my career.

I would like to extend a thank you to Dr. Jorge E. Bohorquez, Ph.D., for his willingness to participate and review this thesis.

I would like to acknowledge the rest of the team at the Ophthalmic Biophysics Center, past and present, for their support and comradery. Current Ph.D. students; Mariela Aguilar, M.S.B.M.E., Victor Hernandez, M.S.B.M.E., Bianca Maceo, B.S.B.M.E., Heather Durkee, M.S.B.M.E. and Siobhan Williams, B.S.B.M.E., and former students; Alejandro Arboleda, M.S.B.M.E. and Karam Alawa, B.S.B.M.E.. I would like to thank Florence Cabot M.D., Cor Rowaan B.S.E.M., Alex Gonzalez, B.A., Varona Sargent, B.S., Esdras Arrieta, M.D., and Billy Lee for their technical support. I would like to thank former students Judith Birkenfield, Ph.D., Krystal Sotolongo B.S.B., Ryan McClure, B.S.B.M.E. and Stephanie Delgado, M.S.B.M.E. for their support beyond their tenure at the OBC. I would like to acknowledge our collaborators in Australia at the Brien Holden Vision Institute, especially Arthur Ho, Ph.D. and Brien Holden, Ph.D..

I would like to acknowledge financial support from the Australian Government CRC Scheme (Vision CRC), Florida Lions Eye Bank, Dr. K.R. Olsen and Dr. M.E. Hildebrandt, NIH grants 2R01EY14225 and 1R01EY021834 and from an unrestricted grant from Research to Prevent Blindness to the Department of Ophthalmology, P30EY14801 NIH (Center Grant).

Table of Contents

List of Figures

List of Tables

Chapter 1

Aims of the Study

Within the eye, the crystalline lens acts as a focusing element, capable of changing shape and power to allow the eye to focus on objects both near and far: this process is called accommodation[1, 2]. With age, the crystalline lens gradually loses accommodative power; this condition leads to the loss of near-vision function in adults. This is called presbyopia. Presbyopia is universal and unavoidable. There are multiple mechanisms at work within the eye that contribute to the loss of accommodation, and several research and development projects at the Ophthalmic Biophysics Center (OBC) at the University of Miami's Bascom Palmer Eye Institute are focused on understanding, through a multi-disciplinary approach, why presbyopia happens and what can be done to reverse its effects. Part of this investigation requires acquiring images and biometric measurements of the changing shape of the human crystalline lens *in vivo* during accommodation. To this effect, an Optical Coherence Tomography (OCT) device was developed at the OBC to acquire high-resolution cross-sectional *in vivo* real-time images of the eye non-invasively.

In Spectral-Domain OCT (SD-OCT) imaging, there exists a trade-off between speed, depth and axial resolution. Clinical OCT systems traditionally have an imaging depth of 1-3 mm. In order to truly understand the mechanisms at work during accommodation, and imaging depth of at least 15 mm is necessary to image the entire anterior segment of the eye including the crystalline lens[3]. OCT technology is well-suited for this kind of study since it is non-contact, non-invasive and fast enough to provide real-time high-resolution images of the eye *in vivo.*

The team at the OBC have addressed this need by developing an SD-OCT system with an unprecedented imaging depth of 10.4 mm in air and implementing an optical switching technique that extends the imaging depth threefold[3]. Integrating an optical switch into the reference arm of the OCT system allows the device to quickly alternate imaging depth and acquire images at different depths within the eye. The system combines custom hardware with commercial software and a control unit that was purchased to accelerate development. Interfacing the optical switch with this commercial system has proven challenging due to the limited number of accessible output signals from the commercial system. The optical switch requires precise timing to correctly synchronize the device with existing image acquisition software to ensure that the system is properly aligned for each frame and the transient states are not imaged.

The purpose of this project is to develop an electronic control unit that will interface the optical switch with the SD-OCT system for the acquisition of images with extended axial range.

The aims of the study are:

AIM 1: Design and implement an electronic control unit that synchronizes the operation of the existing SD-OCT system with, as well as providing control for, the optical switch.

AIM 2: Validate the developed control unit by imaging the *in-vivo* accommodative response of the eye in real-time.

Chapter 2

Background and Significance

2.1 Lens Accommodation

One of the research objectives at the Ophthalmic Biophysics Center (OBC) is the understanding of the mechanism of accommodation and what factors contribute to the onset of presbyopia; the loss of near vision with age. It is of particular interest to the group to quantify how the geometry of the crystalline lens changes dynamically with accommodation as it provides insight into building more accurate optical and mechanical models of the accommodative response[2, 4, 5] as well as providing a method to evaluate phaco-ersatz, a surgical technique to restore accommodation originally proposed by Parel et al[6] and currently under development at the OBC in collaboration with the Brien Holden Vision Institute in Sydney, Australia.

The quantification of changes in intraocular distances dynamically with accommodation has been done with several imaging modalities: modified retinoscopy[4], ultrasonography[1, 2, 7, 8], partial coherence interferometry[9] and Scheimpflug imaging[10-12]. Optical Coherence Tomography (OCT) provides the unique advantage of 3D imaging capability, high resolution and fast acquisition speeds over other methods.

2.2 Optical Coherence Tomography (OCT)

Optical Coherence Tomography derives information about the structural organization of semi-transparent tissue from backscattered or back-reflected light at interfaces between regions of different optical properties[13]. It is similar in operation to ultrasound: measuring the echo delay and intensity of backscattered light from internal tissue microstructure[14].

OCT has proven effective for high-speed cross-sectional, high-resolution (3-5 μm axial resolution) imaging of the eye due to the semi-transparent nature of ocular tissue. OCT is preferable over other imaging modalities because it is capable of producing high-resolution images *in vivo* and in real time without disrupting or damaging or making contact with the tissue. At the OBC, OCT is used, among other applications, to non-invasively study the accommodative response of the crystalline lens both *in vivo* and *in vitro*. The goal of these studies is to better understand the structure and function of the crystalline lens during accommodation and to evaluate the outcome of surgery designed to restore accommodation. OCT is based on low coherence interferometry (LCI), and classic implementations are based on the Michelson interferometer (Figure 1): light from a low-coherence light source is directed towards a beam splitter. The low-coherence light is split into a reference and sample arms of length l_r and l_s, respectively. Light reflects off of the reference and sample mirrors and returns to the beam splitter, where it recombines and is directed towards the detector arm where a photo detector records the interference pattern generated by the light travelling from the reference and sample arms.

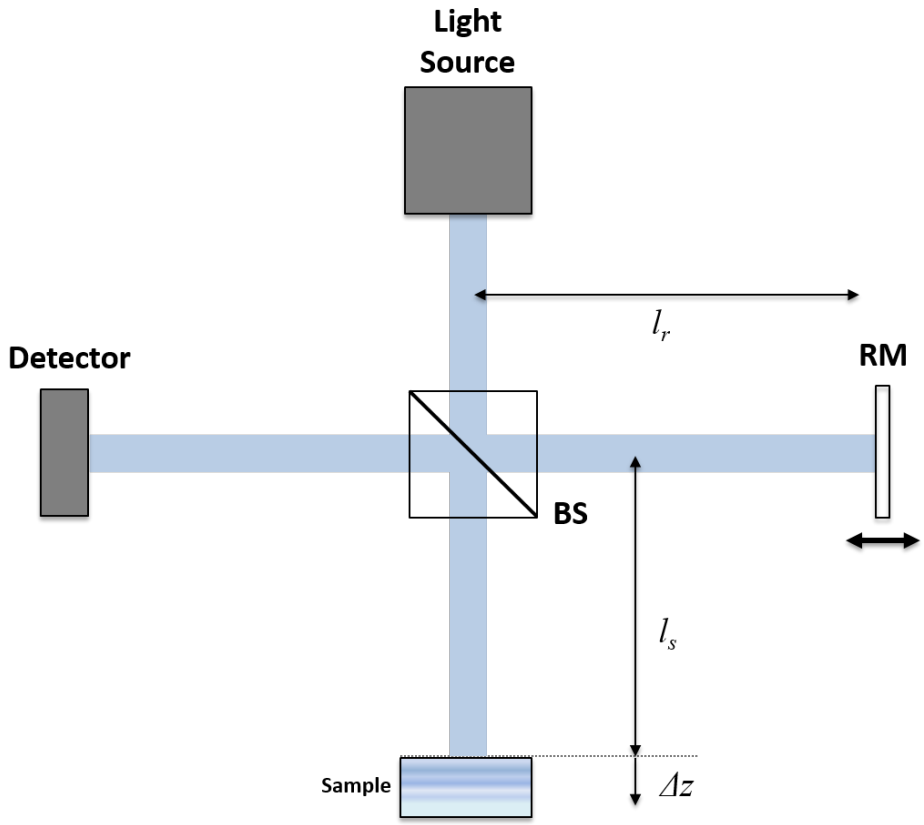

Figure 1 Basic interferometer operation of OCT is based on the Michelson interferometer. RM = reference mirror. BS = beam splitter. l_s = length of the sample arm, l_r = length of the reference arm. Δz = depth into the sample.

2.1.1 Time-Domain OCT

In Time-Domain OCT (TD-OCT), the length of the reference arm is modulated in time to allow the device to focus on different depths of the sample. The reference mirror is moved in the *z* direction to obtain a single axial scan (A-line) containing the total interference signal at a specific transverse location on the sample. The intensity profile is then displayed in grey scale to represent the axial reflectivity profile of the sample at a single transverse location. Several A-lines are acquired and displayed adjacent to each other to make up an image.

For every transverse location the TD-OCT collects a single A-line, which represents a single vertical line in the final cross-sectional image (B-Scan). The beam is moved transversally by employing a series of moving mirrors and optics to deliver the OCT beam across the sample. In Figure 2 a schematic for a TD-OCT is shown with a moveable reference mirror (RM) and a single galvanometer-mounted mirror (GX) for transversal scanning. In general, TD-OCT implementations also include a second transversal scanning mirror for scanning the Y direction.

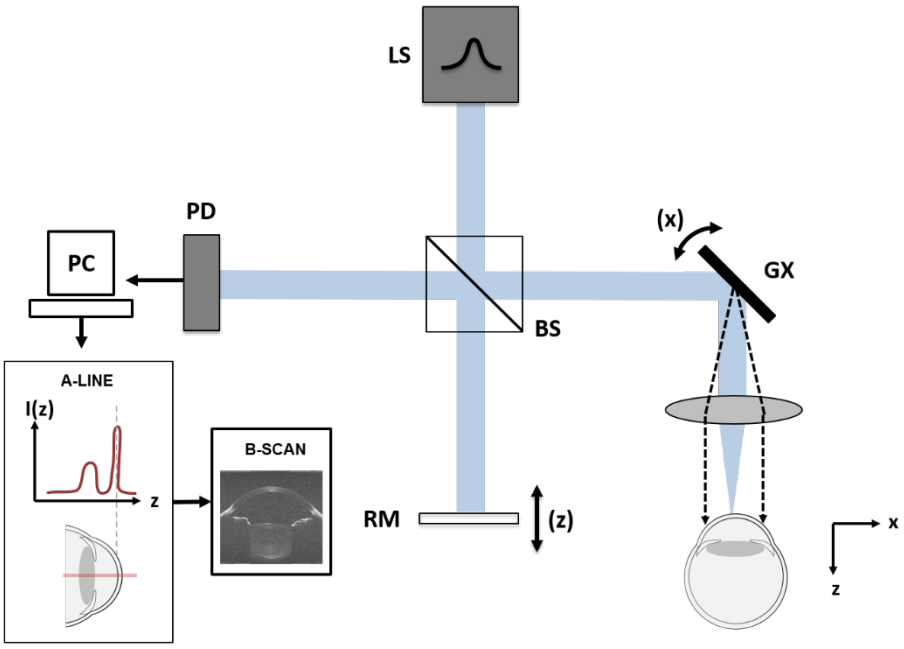

Figure 2 Schematic of a Time-Domain OCT. The LS (low-coherence light source) serves as the light source. Light is sent through the BS (beam splitter) towards a reference mirror (RM) and towards a galvanometer-mounted scanning mirror (GX). The reference mirror moves to modulate the scanning location in z (depth) and the GX rotates to modulate the scanning position in x. The backscattered light from the object is reflected back through the BS to the photodetector (PD) and sent to the computer.

The intensity of the detected interference signal is a function of the wavelength of the light source, λ, the depth into the sample, $\Delta z = l_s - l_r$, and the intensities of the reflected signal from the reference arm and sample arms ($i_s(k)$ and $i_r(k)$, respectively). We express the wavelength in terms of the wave-number, $k = 2\pi/\lambda$:

$$I(k,z) = i_s(k) + i_r(k) + 2\sqrt{i_s(k)i_r(k)}\cos\left[2k(\Delta z)\right]. \qquad (1)$$

Integrating the interferences over all the spectral components yields the total interference signal as proportional to the sum of a DC term and twice the real part of Fourier transform of the power spectrum of the source, *S(k),* modulated by a cosine term[15-17]:

$$I(z) \propto I_s + I_r + 2\Re[\mathcal{F}(S(k)][\cos(2k\Delta z)]) \quad (2)$$

Interference fringes occur at the maxima and minima of the cosine term, and are thus a function of the wave number, k and the optical path length difference between the two arms, Δz. Additionally, the fringes are only detected when they lie within the coherence length of the light source, which presents as the width of the envelope of the modulated cosine term. The envelope of the coherence function is directly related to the axial resolution of the system (discussed in section 2.1.3, later).

Due to the TD-OCT's requirement to mechanically move the reference mirror to produce an axial scan, its acquisition speed is relatively slow; the typical speed of a TD-OCT is 2,000 A-lines/sec[18], which when imaging *in vivo* structures would make the images very prone to motion artifacts.

2.1.2 Spectral-Domain OCT

Spectral-Domain OCT (SD-OCT) provides a dramatic improvement in imaging speed. SD-OCT uses a spectrometer instead of a single-point photo detector: a diffraction grating is used to disperse the returned light into its spectral components which are then propagated to an array detector (Figure 3). In SD-OCT, individual spectral components of the interference signal are separately recorded by the elements of the array detector. Each interference peak generated at a specific depth in the space domain corresponds to a modulation at a different frequency of the detected spectrum. The inverse Fourier

transform of the recorded spectrum, $I(k)$ reveals the depth information without the need for a moving reference mirror.

$$I(z) = \mathcal{F}^{-1}[I(k)] \quad (3)$$

This allows the reference mirror to be fixed, removing the speed limitation induced by the movement of the reference mirror and therefore, higher imaging speeds than those produced with TD-OCT can be achieved. For example, our SD-OCT can operate at 20 kHz, recording a 400 A-line frame in 8 ms.

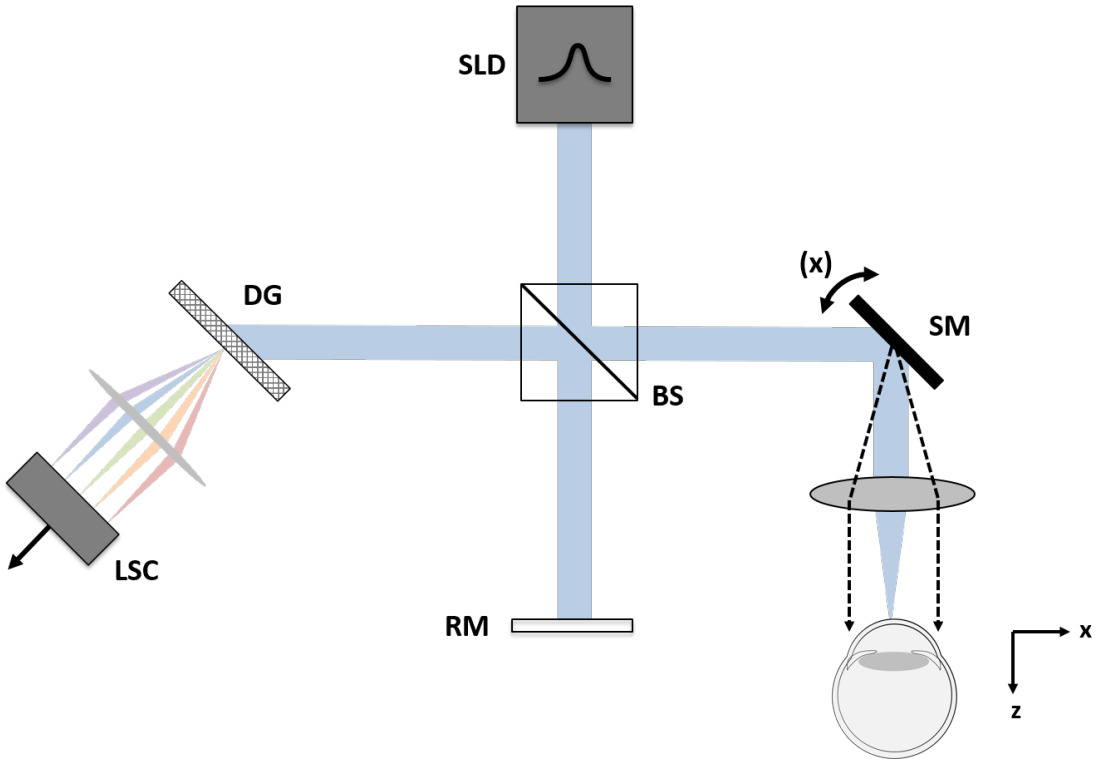

Figure 3 Scheme of a spectral-domain OCT. The SLD (super luminescent diode) is a broadband light source. Light is directed through the BS (beam splitter) towards a reference mirror (RM) and a scanning mirror (SM). The reference mirror does *not* move, while the SM still moves to modulate imaging location. The backscattered light travels back through the beam splitter to a diffraction grating (DG) where it is split into an array of beams of different wavelengths and each spectral slice is mapped to an individual pixel on the Line-Scan Camera (LSC).

2.1.3. Depth and Resolution Limitations of OCT

In order to achieve imaging of the entire anterior segment, we require high-contrast and high-resolution over the range of the cornea, anterior chamber and crystalline lens, which requires at least 15 mm of depth in air[3].

In OCT systems, resolution and depth are limited by the properties of the light source and the hardware implemented to detect the back-reflected light and perform the axial scan, respectively.

Lateral Resolution

The lateral or transverse resolution is determined by the optics in the beam delivery unit, which dictate beam waist size at the focus position. In the conventional telecentric scanning configuration used for anterior segment imaging, this is expressed as

$$\Delta x = \frac{4\lambda}{\pi}\frac{f}{d} \tag{4}$$

Where λ is the central wavelength of the light source, *f* is the focal length of the objective lens, and *d* is the diameter of the light beam on the objective lens[16].

Axial Resolution

Axial resolution in interferometry systems is dependent on the spectral characteristics of a light source. Conventionally, two distinct peaks in an interference pattern are considered resolved when the distance between their maxima is one FWHM (full-width, half –maximum) away from each other. This is referred to as the Rayleigh criterion. This value can be found by setting the envelope function of a Gaussian spectral distribution equal to ½[16].

$$\Delta_z = \frac{2ln2}{\pi}\frac{{\lambda_0}^2}{\Delta\lambda} \cong 0.44\frac{{\lambda_0}^2}{\Delta\lambda} \tag{5}$$

Where λ_0 is the central wavelength of the source, and $\Delta\lambda$ is the bandwidth.

Therefore, in order to improve the resolution, one can choose a light source with a wider bandwidth or smaller central wavelength.

Axial range

In TD-OCT applications, the axial range of the imaging device is determined by the range of movement of the reference mirror.

In Fourier domain, an interference peak generated at a larger depth, *z*, in the space-domain, is represented by modulation of the detected spectrum of higher frequency. The detectable depth is therefore relative to the maximum detectable modulation of the spectrometer.

The maximum depth can be expressed in terms of the central wavelength of the light source, λ_0, and the width of the spectral range that can be acquired by the photo detector array, $\Delta\Lambda$, and the number of pixels of the array, N [14] .

$$z_{max} = \frac{1}{2}\frac{N}{2}\frac{{\lambda_0}^2}{\Delta\Lambda} \qquad (6)$$

The axial range is dependent on the properties of the photo detector array and the arrangement of the spectrometer, which determines the spectral range, $\Delta\Lambda$. Line scan cameras exist with pixel densities ranging from 2k up to 12k[19]. The camera used in the SD-OCT system at the OBC is 4k.

In SD-OCT, there exists a trade-off between axial resolution and axial range[14, 20]. For optimal resolution, a larger bandwidth and smaller central wavelength are desired. For a larger axial range, the opposite is true: a larger central wavelength and smaller bandwidth are more desirable. Therefore there exists an inherent trade-off between

extending the axial range and maintaining high resolution. With the given hardware, one must be sacrificed to improve the other.

Sensitivity Decay with Depth

In SD-OCT, in addition to the limitations on axial range and resolution, there also exists a degradation of sensitivity with depth, which in turn, decreases the image quality at larger depths. This decrease of sensitivity is referred to as sensitivity "fall-off" or "roll-off" and is mainly due to optical limitations in the implementation of the spectrometer. Figure 4 shows an image of the anterior segment acquired with the existing SD-OCT system; the decrease of sensitivity with depth degrades the quality of the image and the structure deeper within the crystalline lens cannot be identified.

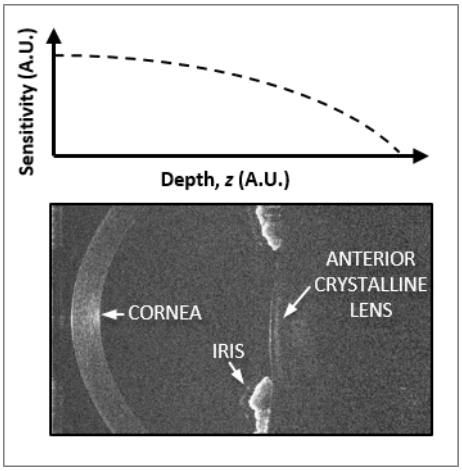

Figure 4 The effect of sensitivity "roll-off" with depth is shown. Deeper parts of the uncorrected image show very little contrast and almost no structure can be observed.

The sensitivity fall-off is a product of the design of the spectrometer and the finite size of the camera pixel and has several contributing factors discussed in literature [21-23].

2.2 Strategies to Extend the Axial Range

There are several proposed strategies to extend the axial range in SD-OCT imaging.

2.2.1 Dual-OCT Systems

Some groups have addressed the limited range by combining two OCT systems into a single delivery probe through the use of a beam-splitter, allowing each OCT to be tuned to a separate depth and used for simultaneous imaging of two different locations in the tissue. Using two separate OCT imaging systems enables increasing the axial range while maintaining high axial resolution. However, this method presents synchronization and alignment issues as well as being costly due to the requirement of two separate spectrometers and two separate light sources [24]. Moreover, in order to comply with light exposure safety standards, the power delivered by each arm of the OCT system must be decreased to lower overall light exposure to the eye, which in turn, decreases the overall sensitivity of the system.

2.2.2 Swept-Source OCT

Another form of OCT using spectrally encoded depth information (Fourier-Domain OCT or FD-OCT) uses a rapidly tunable laser light source (swept-source) to modulate the source wavelength by sequentially emitting very small instantaneous bandwidths at very high rates. The interference light is then sequentially detected by a single point detector and once all of the spectral information is completely acquired, the inverse Fourier transform is applied to obtain the reflectivity profile of the sample. The optical properties of Swept-Source OCT (SS-OCT) detection and the tunable light source in SS-OCT allow for imaging with an extended axial range with negligible fall off at high speed. For example, Potsaid *et al* developed a tunable Vertical Cavity Surface Emitting Laser (VCSEL) which can perform the frequency sweep needed for SS-OCT extremely quickly (100 kHz vs previously reported speeds of 10 kHz). The VCSEL allows them to

deliver an image with negligible sensitivity roll-off over about one centimeter of depth [25]. However, the trade-off between resolution and depth still exists.

2.2.3 Complex Conjugate Removal Methods

A drawback of the SD-OCT method is that when the spectrally encoded depth information is decoded with a Fourier Transform, positive and negative path differences with respect to the zero-delay position are indistinguishable (this is referred to as the complex conjugate ambiguity). The result is an image which appears mirrored about the zero-delay position with both positive and negative path difference sections of the image overlapping on the same frame, as shown in Figure 5 (left). For example, when imaging the anterior segment, the cornea appears to rest on the posterior surface of the crystalline lens if the zero position is set near the anterior surface of the crystalline lens.

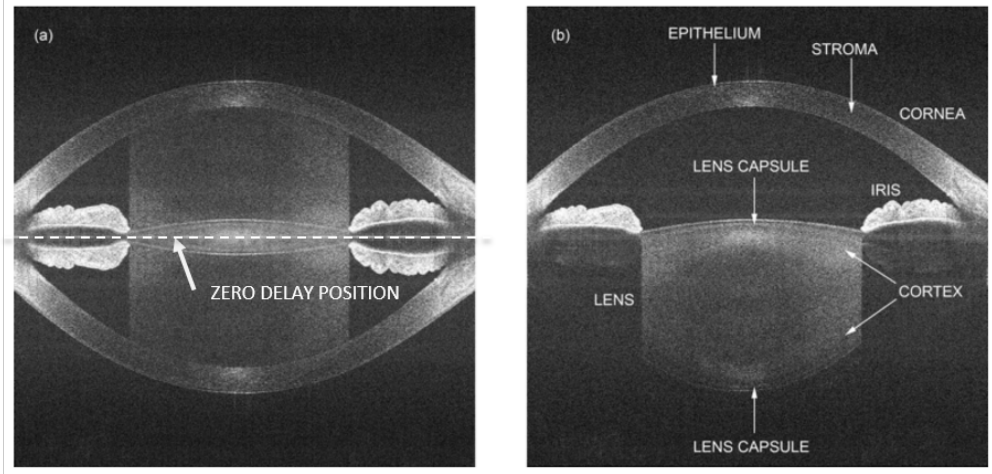

Figure 5 (left) Shows the complex conjugate ambiguity and demonstrates how the resulting image appears with one half super-imposed over the other. (Right) Shows the results of the Jungwirth et al's complex conjugate removal algorithm on the original image. Original images from "Extended *in vivo* anterior eye-segment imaging with full-range complex spectral domain optical coherence tomography" JBO Letters, 2009 [26].

One method to double the imaging depth is to remove the complex conjugate ambiguity so that the positive and negative frequency range contains depth information. Different techniques have been used which involve measuring the phase of the spectral

information by introducing a phase shift in the reference scan or the transversal scan [26-28]. Figure 5 shows the results of one group who used complex conjugate removal to create a cross-sectional image of the anterior segment, the original acquisition is shown on the left, and the final image is shown on the right. Complex conjugate removal methods, in general, require the acquisition of multiple images or more complex hardware and software to be implemented, adding complexity and cost to the OCT system or sacrificing imaging speed. Even when resolving the complex conjugate information; these images suffer from a decrease in image quality and the presence of artifacts[28].

2.2.4 Optical Switching Techniques

The effective imaging range of an SD-OCT has been increased using an optical switching technique. By placing a high-speed fiber switch in the reference arm, Wang et al. have shown a method to modulate the reference arm length between consecutive scans [29]. Figure 6 shows how the SD-OCT is configured with the optical switch alternating the reference arm between two reference mirrors, M1 and M2, at δx distance apart.

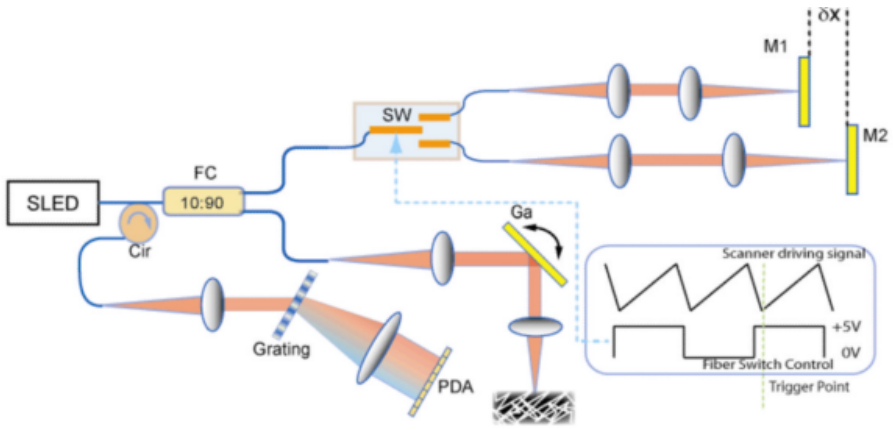

Figure 6 Schematic of Wang et al.'s SD-OCT with an integrated optical switch in the reference arm: Two reference arms with mirrors (M1 and M2) were separated by a distance of δ× and alternately accessed by a high speed fiber switch (SW). FC: fiber coupler; Cir: fiber circulator; Ga: galvanometer; PDA: InGaAs photo detector linear array; SLED: super luminescent diode. Image taken from "Extending the effective Imaging range of Fourier Domain OCT using a fiber optic switch" Optics Letters, 2008 [29]

The device alternated the length of the reference arm for every frame acquired, and thus the imaging depth for every other acquisition. This allows the system to acquire consecutive images of the same tissue with alternating areas of high sensitivity. In post-processing, consecutive images are concatenated into a single image with increased area of high-sensitivity throughout and thus a larger effective axial range without sacrificing resolution as shown in Figure 7 [29].This system, however, doubles the time required to acquire a single frame by requiring two images for each final frame.

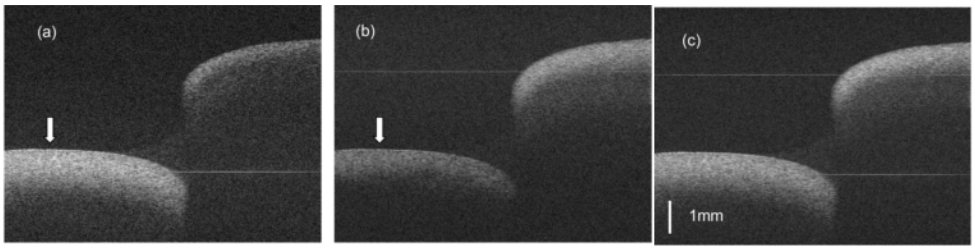

Figure 7 Image (a) and (b) show the individual OCT scans at each imaging depth of *ex vivo* dog endocrinal tissue with (a) showing high sensitivity towards the bottom and (b) showing higher sensitivity towards the top. Image (c) shows the final image combined in post-processing with high sensitivity across a larger depth. Images taken from "Extending the effective Imaging range of Fourier Domain OCT using a fiber optic switch" Optics Letters, 2008 [29]

2.3 The Existing SD-OCT System

The Spectral-Domain OCT device developed at the OBC has been designed to image 10.4 mm in air [3]. Figure 8 shows the overall design of the SD-OCT system. The system has been outfit with a custom-made optical switch with the intent to increase its axial range similar to what Wang et al proposed[29]. An accommodation stimulus device was placed in line with the delivery optics to allow for acquisition of images of the eye during stimulated accommodation.

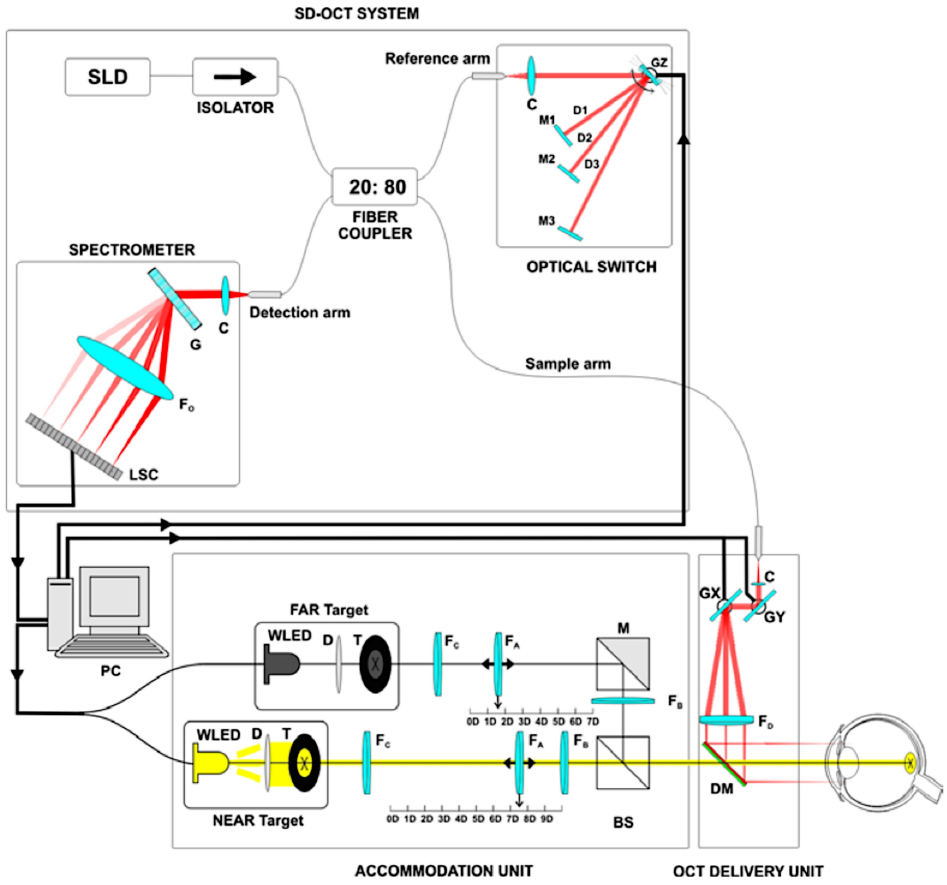

Figure 8 Schematic of the OBC's OCT system. The SD--OCT system is shown with the Optical Switch in the reference arm. SLD: Light source. LSC: Line-Scan camera. F_o: Objective lens of the spectrometer. C: collimator. G: Grating. M1, M2, M3: Mirrors, GZ: Axial galvanometer scanner. The accommodation module and the OCT delivery unit are also shown. GX and GY: Transversal galvanometer scanners. F_D: Objective lens of the OCT delivery unit. DM: Dichroic mirror. BS: Beam splitter. M: 45° Mirror. F_B: Badal lens. F_A: Auxiliary lens. F_C: Collimating lens. T: Target. D: diffuser. WLED: White light LED. Image taken from "Imaging and full length biometry of the eye during accommodation using spectral domain OCT with an optical Switch" Biomedical Optics Express, 2012 [3].

2.3.1 SD-OCT

The SD-OCT system consists of a super luminescent diode (SLD) centered at λ =840 nm with a FWHM bandwidth of $\Delta\lambda$ =50 nm. The light is passed through a 2x2 20/80 fiber coupler and sent to the sample and reference arms. The reference arm has been modified from the traditional SD-OCT through the addition of an optical switch. The light from the sample and reference arms is recombined through the fiber coupler and propagates to the spectrometer. The spectrometer consists of a collimating lens, an 1800 line/mm transmission grating, an achromatic imaging lens and a dual-line scan

camera with 4000 pixels operating at 140 kHz, CMOS camera operating in summing mode between two detector lines.

An image acquisition board acquires the image captured by CMOS camera and transfers it to a computer workstation for signal processing and real-time acquisition and display of the OCT data through commercial software. The measured axial range of the resultant image was 10.43 mm and the resolution for depths below 7 mm is 8 μm. Beyond the first 7 mm, the free-space axial resolution progressively degrades until it reaches 14 μm at the end of the axial range. The sensitivity decreases from 98 dB near the zero-delay position to 55 dB at 10 mm, as shown in Figure 9 [3].

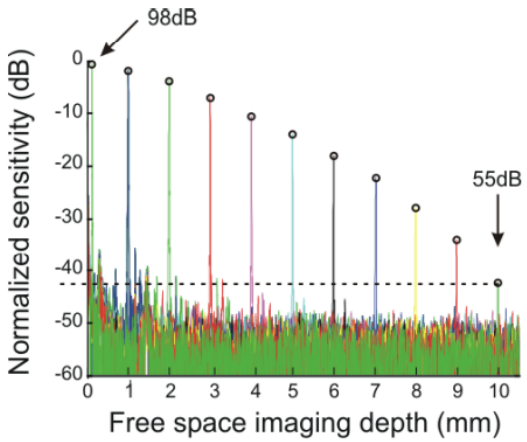

Figure 9 Plot of the sensitivity of the SD-OCT system as a function of depth in air. Image taken from "Imaging and full length biometry of the eye during accommodation using spectral domain OCT with an optical Switch" Biomedical Optics Express, 2012 [3].

2.3.2 OCT Delivery Unit

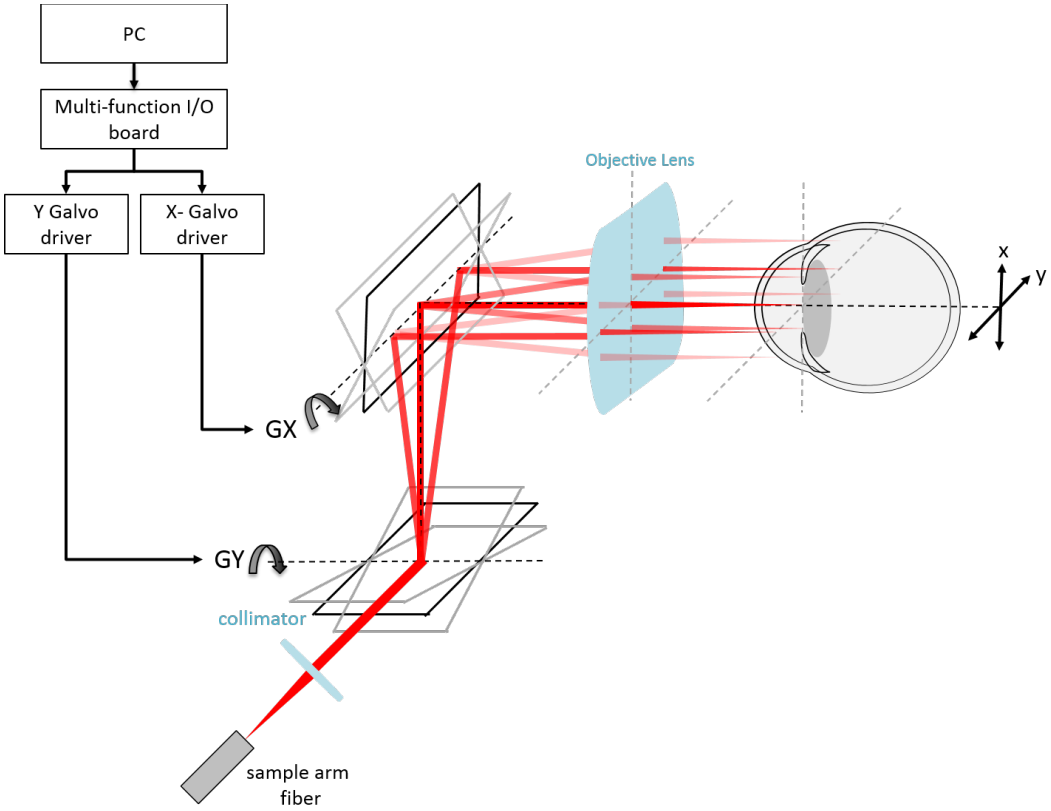

Figure 10 The delivery optics for the SD-OCT are configured in a telecentric configuration, and the transversal scanning block is controlled from the PC through the multi-function I/O board and the corresponding X and Y galvanometer drivers. Light is directed from the beam splitter, to a collimator and directed at one galvanometer-mounted mirror (GY) to shift the beam in the Y direction and then towards a second mirror (GX) to shift the beam in the X direction. The light then passes through a second lens to re-focus the beam onto the relevant plane in the eye.

In order to accomplish two and three dimensional scans, the OCT system features a beam delivery system with an X-Y galvanometer optical scanner. The scanner is set up in a telecentric configuration. Light exits the fiber of the sample arm and is collimated through a collimator. The light beam is then deflected by the two mirrors in the galvanometer optical scanner along the vertical and horizontal direction. As shown in Figure 10, the two galvanometer-mounted mirrors are positioned perpendicular to each other and are tilted to direct the beam to a location along the frontal imaging plane. As the mirrors rotate, the beam is translated in X and Y in the frontal plane. The angular

position of the transverse scanning mirrors is set by a voltage provided to the galvanometer driver boards from the computer through a multifunction I/O board.

The light is then focused through the objective lens which is mounted in a telecentric configuration to image the eye with scanning parallel beams. To ensure telecentric delivery of the beam in the horizontal plane, the objective lens is placed one focal length away from the X galvanometer mirror.

2.3.3 Accommodation Unit

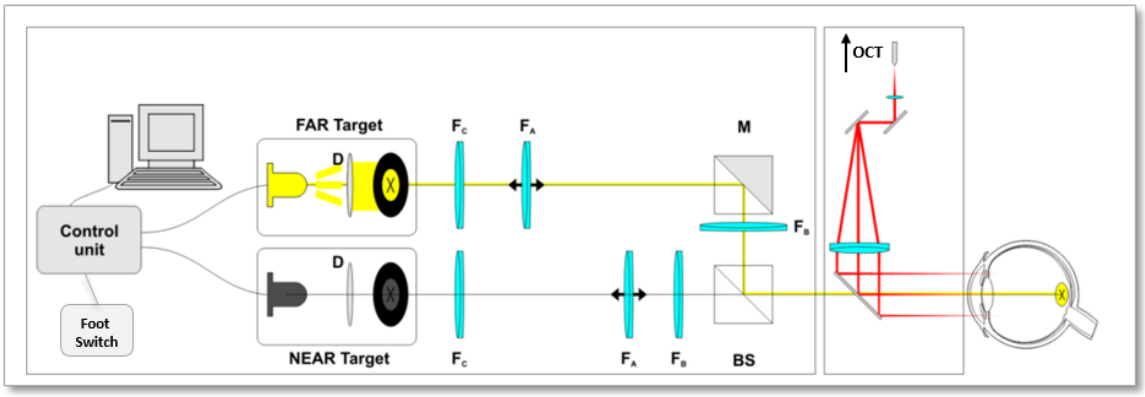

Figure 11 Accommodation Target schematic: The near and the far target can be adjusted by the user by moving the focusing lens, F_A. The retro illumination alternated between the near and far target when the footswitch is pressed, illuminating only one target at a time. Taken from "Imaging and full length biometry of the eye during accommodation using spectral domain OCT with an optical Switch" BOE, 2012 [3].

An adjustable switching accommodation target is installed along the optical axis of the eye allowing for step-change in accommodation stimulus (Figure 11). The target provides a monocular accommodation step stimulus. It consists of two independent modules based on the principle of a Badal optometer that have been coupled with an electronic control unit to ensure only one module is active at a time, with each module providing an adjustable level of accommodative stimulus. The amplitude of the step stimulus can be adjusted by the operator and ranges from 0 to 9.5 D by moving a set of lenses in-line with the target.

Each target is retro-illuminated by a diffuse light from a white light LED (WLED), and is only visible to the subject when it is illuminated. The device is connected to a foot-switch which allows the operator to switch the retro-illumination between the two targets; turning on only one WLED at a time and thus providing a step-change in accommodation stimulus. The accommodation module is coupled with the OCT delivery system using a dichroic mirror.

2.3.4 Optical Switch

The optical switch consists of an aspheric lens collimator, a galvanometer optical scanner and three free-space optical delay lines that are radially arranged around the axis of rotation of galvanometer mirror (GZ, Figure 12). A schematic of the optical switch set up is shown in Figure 12. The optical delay lines (D1, D2 and D3) use three mirrors (M1, M2 and M3), each mounted on precision linear stages with a positioning resolution of 1 µm. These mirrors have been positioned at calibrated distances relative to each other. This allows us to introduce an axial offset in the imaging depth by switching the reference arm light between each delay line. Each delay line is selected by rotating the angular position of the optical scanner, which is set by an analog input voltage to the servo driver in the same way the transversal scanners are set. The voltages that correspond to each radial position are known and discussed in the following chapter.

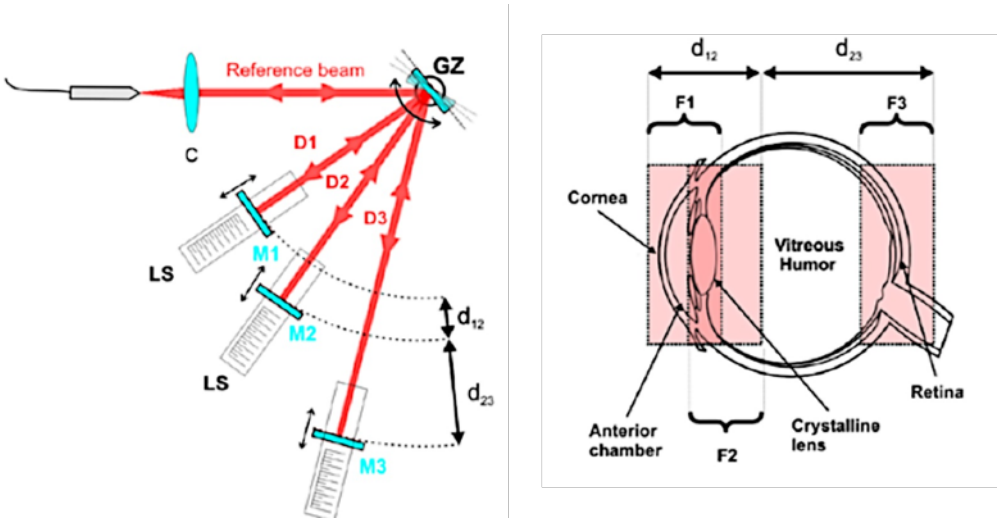

Figure 12 (Left) The modified reference arm of the SD-OCT featuring the Optical Switch. C: Collimating lens. GZ: galvanometer scanner. D1, D2 and D3: Delay lines 1, 2 and 3. M1, M2, and M3: mirrors 1, 2 and 3. LS: Linear stage. d_{12}: distance between M1 and M2. d_{23}: distance between M2 and M3. (Right) Shows the frames as acquired on an emmetropic eye and the corresponding tissue they are imaging. F1 corresponds to the frame acquired when the reference arm is transmitted through delay line D1, F2 through D2 and F3 through D3. D_{12} is marked as the distance between the anterior cornea and posterior lens because F2 is flipped in post-processing to allow the system to use the sensitivity roll-off to its advantage by overlapping the part of the images that have the lowest sensitivity to make up for the roll-off. Image taken from "Imaging and full length biometry of the eye during accommodation using spectral domain OCT with an optical Switch" Biomedical Optics Express, 2012 [3].

The optical switch implemented in the reference arm increases the scanning depth without sacrificing resolution; several images at different depths in the eye can be acquired and then recombined to produce a single seamless image of the entire anterior segment. Our method is similar to that which was presented by Wang et al. in 2008[29]. Instead of using a fiber-based optical switch, we implement a galvanometer-mounted mirror-based optical switch, shown in Figure 13.

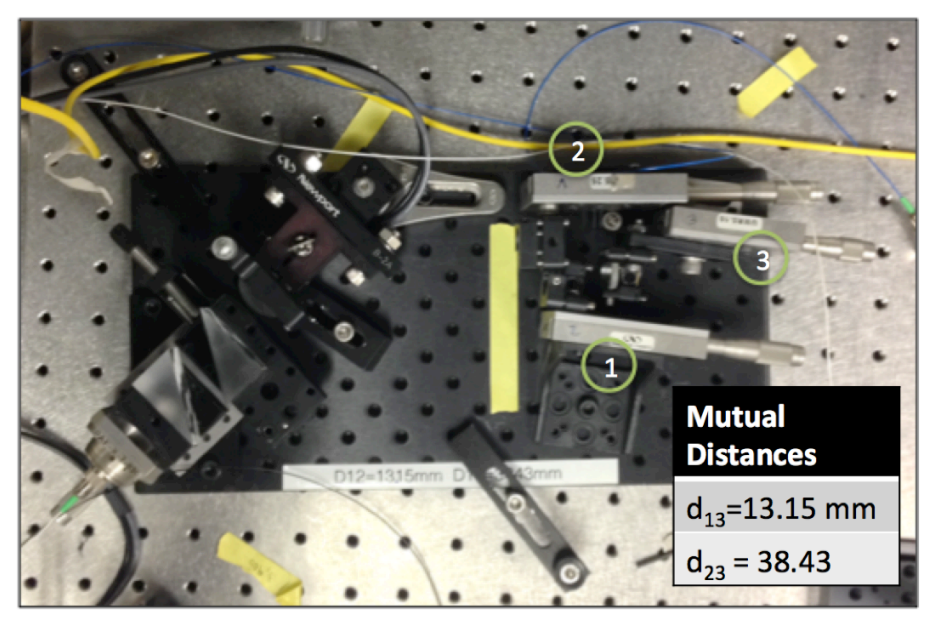

Figure 13 The physical set up of the optical switch is shown. Each reference mirror is mounted on a high-precision linear stage, and the optical path length distances between the mirrors is known. The mutual distance between mirror 1 and 2 is 13.15 mm in air and the mutual distance between mirror 2 and 3 is 38.42 mm in air.

The axial offsets are set to sequentially image the cornea, lens and retina of the eye by providing a fixed voltage to the servo driver. Figure 12 shows how the three reference, M1, M2 and M3 mirrors are radially distributed around the galvanometer-mounted mirror (GZ). Each mirror corresponds to the biological structures shown in Figure 12 (right).

Imaging separate frames at different depths produces multiple images with different areas of high-sensitivity. Figure 14 shows how this is done for two images; Frame A is acquired in the anterior chamber and shows the cornea and anterior crystalline lens with high sensitivity. Frame B is acquired in the crystalline lens and shows the middle to posterior lens with high-sensitivity throughout the depth. The images are cropped at the dotted red line, and recombined to produce Frame C: An image of the entire anterior segment with high sensitivity. This method was extended to three reference mirrors, with the third mirror positioned to image the retina at a known distance away from the anterior segment. This allows for axial biometric measurements along the length of the eye. Each additional delay line added to the switch increases the overall time required to acquire one frame, so it is preferable to minimize the number of delay lines used.

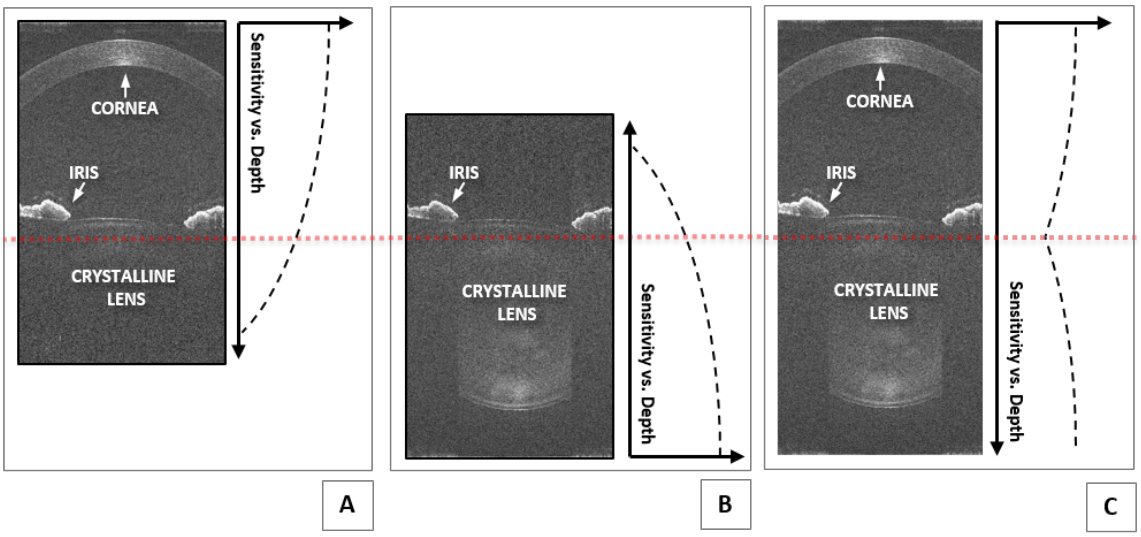

Figure 14 (A) shows the first frame acquired, focused in the anterior chamber (B) shows the second frame and corresponding sensitivity profile. (C) Shows the images combined into a single image of shown sensitivity.

2.3.5 Software Platform

The basic imaging process is monitored, executed and saved by a commercially developed software package called InVivoVue (Bioptigen, NC, USA). The software uses

a series of both analog and digital waveforms to control the components of the OCT system through an I/O board and image acquisition board, including a line-scan camera and the two galvanometer-mounted mirrors. The software platform features two operating modes: alignment preview and image acquisition,

The software is primarily responsible for setting and controlling the image scan parameters and controls the movement of the x-y galvanometer block in time allowing for complex transversal scanning routines including: linear, cylindrical, radial, volumetric, etc.

The operator defines the transversal dimensions of the scan and the user is shown an alignment preview, where the transversal scanning galvanometers scan the eye in a cross pattern displaying two perpendicular cross-sections of the eye (one sagittal and one horizontal). Once the user has aligned the subject, they can begin acquisition, wherein the transversal scanning galvanometers are controlled by the software through voltage-controlled servo drivers to execute the scanning pattern chosen by the user. After acquisition, the on board software stores and processes the images from the imaging session in an integrated database.

2.4 Project Need

The existing optical switch is currently controlled by sending a fixed voltage to the optical scanner control driver, which sets the position of the galvanometer-mounted mirror used to deflect the reference arm.

In principle, an image of the eye including the whole anterior segment and the retinal boundary can be obtained by sequentially providing at least three voltages over time. However, in order to effectively implement this technique, the switching of the

optical switch's galvanometer must be automated and synchronized with the image acquisition of the commercial software to acquire real-time *in vivo* cross-sectional OCT videos acquired with extended depth.

Increased imaging depth provided by the synchronization of the optical switch described will allow for the team at the OBC to image and quantify the dynamics of the accommodative response *in vivo*: once an extended-depth imaging system is in place, real-time video of the anterior segment and retina can be recorded as the subject is responding to a change in accommodative stimuli. From these videos, we aim to extrapolate biometric information on how the elements within the eye change in dimension throughout the process of accommodation.

The challenge presented in this thesis is providing a way for these different units to communicate in a dependable, synchronized and cost-efficient manner.

Chapter 3

Design of the Control Electronics for the Optical Switch

To extend the axial imaging range, we implement the optical switch in a manner that allows us to take consecutive frames at different imaging depths. We aim to acquire consecutive frames with extended depth over time to evaluate the dynamics of the anterior segment. This requires a precise control of the optical switch to ensure the switch changes the depth of acquisition at the end of a frame acquisition. It is critical this switch happens while the SD-OCT is not acquiring image information to preserve as much imaging power as possible. To accomplish this, the SD-OCT system, and the optical switch must be synchronized.

An electronic control unit is developed to synchronize the existing SD-OCT system with the galvanometer based optical switch.

3.1 Signal Specifications

The SD-OCT, Accommodation Stimulus and Optical Switch exist as independent entities. Enabling communication across them requires a thorough understanding of their output and input. The following section goes into detail characterizing the output from the SD-OCT that was used to create the control signal for the control unit as well as describing in further detail the signals required to control the accommodation unit, and optical switch, as well as providing a brief overview of the control software.

3.1.1 Galvanometer Control Signal

As described in section 2.3.2, the OCT delivery system uses two voltage-controlled galvanometer-mounted mirrors to direct the position of the beam transversally across the eye. As mentioned in Chapter 2, the SD-OCT is capable of several scanning

patterns. Each transversal scanning routine is accomplished by moving the transversal scanning mirrors in a precisely choreographed way. While performing rectangular scans, for example, the system modulates the X-galvanometer position quickly, and the Y-axis slowly. For every time the transversal scanning block completes a horizontal scan in X, it translates the beam vertically slightly and then repeats the scan in X. This is referred to as a "raster scan". By repeating this routine several times, a 3-dimensional representation of the sample can be acquired. We thusly refer to the X-axis as the fast axis, and the Y-axis as the slow axis.

When collecting images along the central horizontal axis, the Y galvanometer remains stationary and the X-galvanometer rotates to direct the light across the width of the acquisition area. This is referred to a "linear scan". To understand how the system scans the eye horizontally, we refer to the diagram in Figure 15: a galvanometer-mounted mirror (GX) rotates by a mechanical angle ϕ and deflects the imaging beam by an optical angle, θ. The optical angle determines the width, *D*, of the scan by the geometric relation,

$$D = 2f \tan\theta \qquad (7)$$

where *f* is the focal length of the objective lens (Figure 15). For small angles, θ, the width of the scan is directly proportional to the voltage of the X-galvanometer control signal. Due of the geometry of the optics, the optical angle, θ, is twice that of the mechanical angle ϕ. The mechanical angle is directly related to the voltage input to the galvanometer control board. In order to record a single frame, the X-galvanometer traverses from +ϕ to –ϕ.

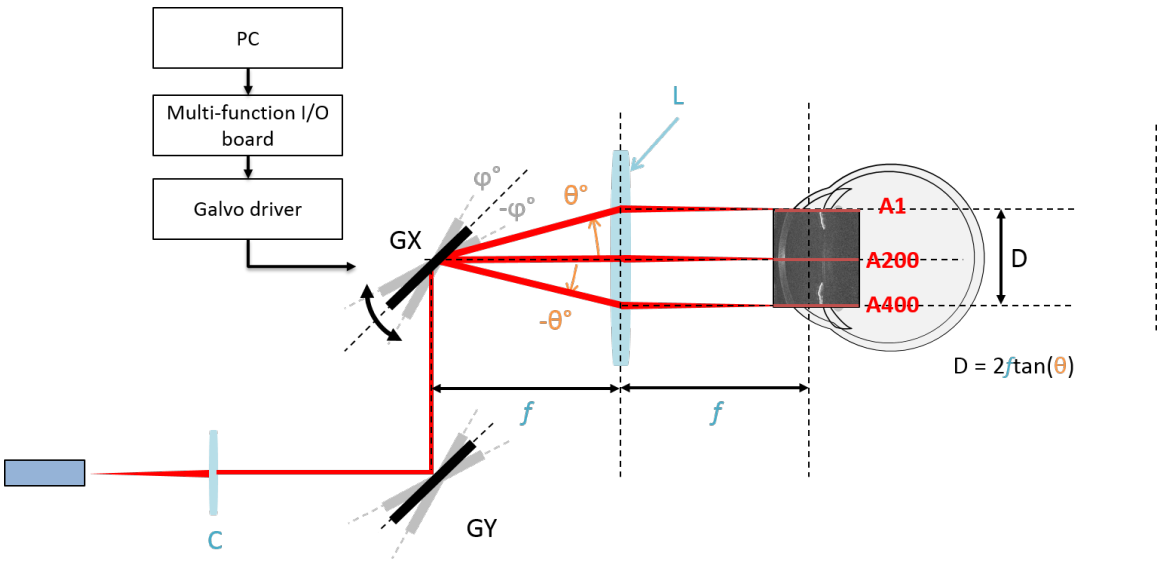

Figure 15 The width of the transversal scan, *D,* is a function of the geometrical properties of the beam optical deflection angle (θ), and the objective lens, *L,* and its focal length, *f.* The beam is centered on the central A-line of the image when the deflection angle is 0. For example, for a scan that has 400 A-lines, the first A-line, A1, is acquired at the positive radial deflection θ, and the last A-line is at negative radial deflection, -θ. The objective lens, L, is mounted in a telecentric configuration

The commercial software provided by Bioptigen (Durham, NC) controls the width, *D*, of the image and the number of A-lines for each B-Scan and thus controls the speed and rotations of the transverse galvanometer mirror by providing a voltage signal to the X galvanometer driver board.

Figure 16 shows a representation of how the X-galvanometer control signal is related to the final image acquired by the SD-OCT. The voltage of the X-galvanometer control signal changes as the system acquires several successive A-lines. The software modulates the voltage according to the dimensions of the scan and decreases the voltage from a maximum value as the image is acquired. As the signal voltage changes, the X-galvanometer rotates and the position of the A-line progresses horizontally. For every clock pulse of the line scan camera, a successive A-line is acquired. These A-lines are assembled into a B-scan of width *D*.

When the signal reaches its minimum value as determined by the software, it quickly rises to return to the maximum value. This time it takes to reset the mirror position is called the fly-back time. During the fly-back time, no images are recorded.

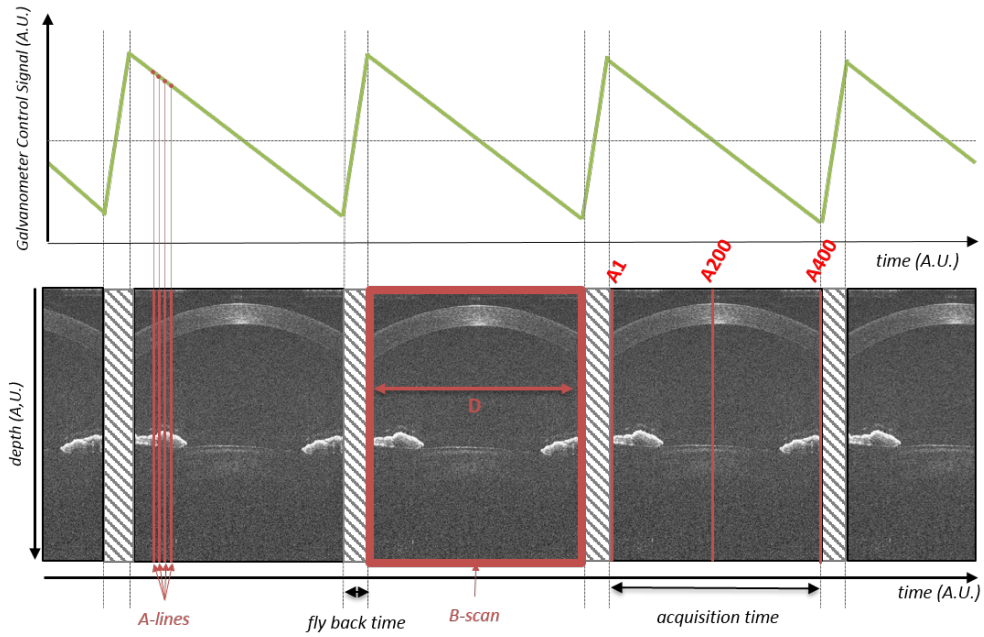

Figure 16 The waveform input to the X-galvonanometer driver board is a saw-tooth wave (top). For every pulse of the CLK signal, an A-line is aquired. These A-lines are stacked to create a B-scan as shown (bottom).

The commercial software follows the following order of operations:

1. The user defines imaging parameters including scan width, scan density, number of inactive A-lines between scans and scan pattern through the Parameters for New Scan window. A screen shot is shown in Figure 17.

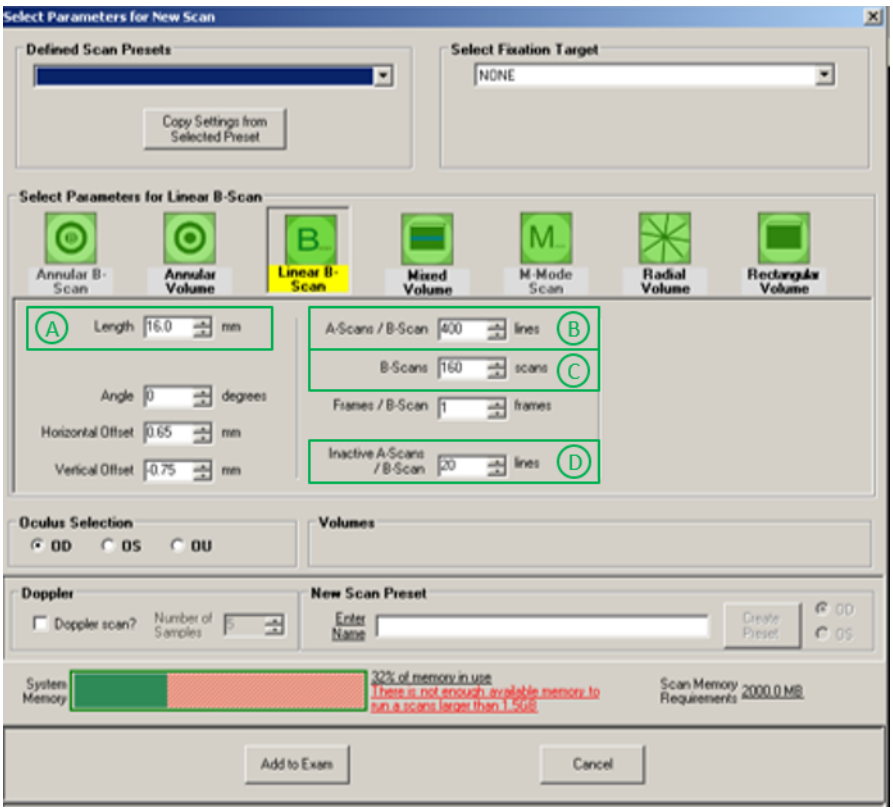

Figure 17 Parameter selection in the InVivoVue software allows the user to select the scanning width, *D*, (A), the scanning density (B), Number of successive B-Scans (C) and number of inactive A-scans per B-scan (D) among other parameters

2. User begins Alignment Mode by pressing the “Start Aiming” button (Figure 18). Two real-time perpendicular cross-sectional images of the imaging plane are continuously displayed on the screen to aid the user in aligning the subject.

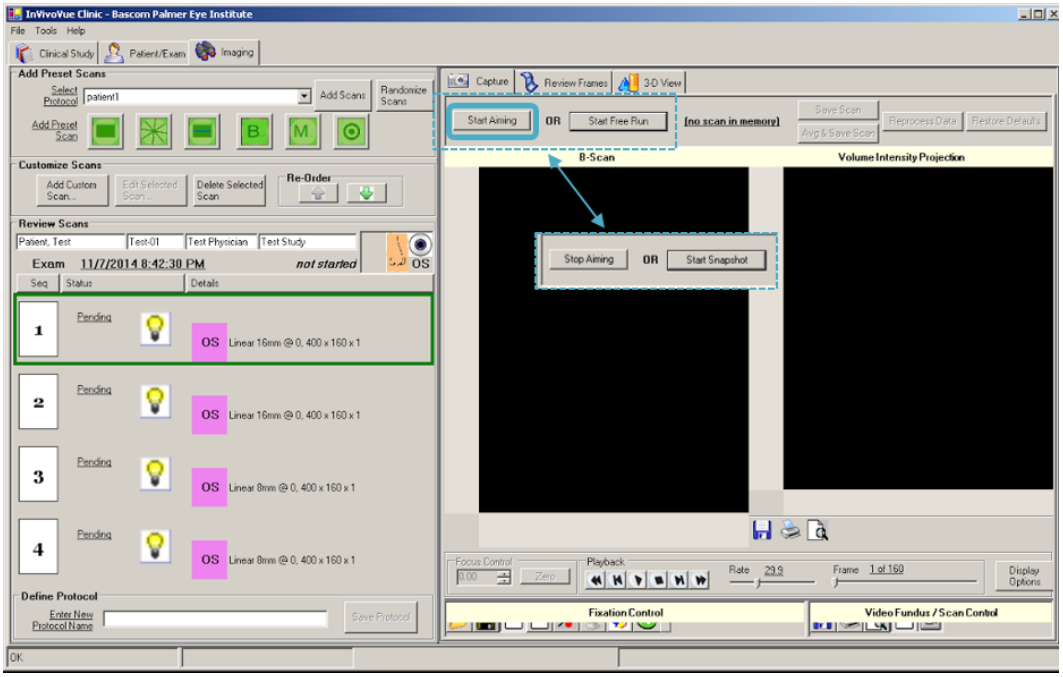

Figure 18 A screenshot of the InVivoVue software used for image acquisition, processing and storage. The Alignment procedure is started by pressing “Start Aiming”. Once the user is in alignment mode, the buttons at the top of the screen give the user the options to “Stop Aiming” and quit alignment mode or “Start Snapshot” which begins the Acquisition routine. The horizontal preview is displayed in the left window and the vertical preview in the right window.

In order to display the horizontal and vertical cross-sections, the galvanometers in the beam delivery unit are scanning the imaging plane in both X and Y directions. The corresponding galvanometer control waveforms for the X and Y galvanometers are shown in Figure 19.

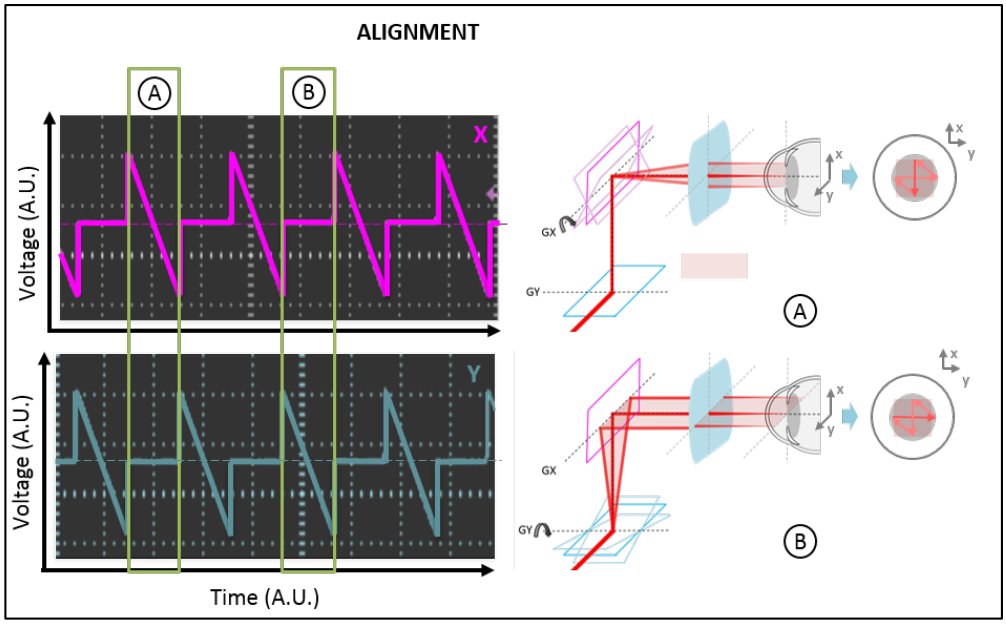

Figure 19 X (pink) and Y (blue) galvanometer control waveforms during alignment mode for a 4mm linear scan with 400 A-lines. Each white box represents 25 ms in time and 200 mV in V. During alignment, the signal is a saw-tooth shaped wave with a delay between each period. The signals are spaced so that only one mirror is moving at a time: A) shows a time when the system is scanning in X and not in Y. Conversely, (B) shows a time period where the system is scanning in Y and not in X.

3. User initiates acquisition through the software and the scanning pattern the user defined in step 1 is executed. For several linear B-Scans acquired consecutively in the horizontal plane, the X-galvanometer control signal sweeps from positive to negative voltages for every frame, consequently translating the light across the horizontal plane of the imaging plane. The corresponding X-galvanometer control waveform is shown in Figure 20.

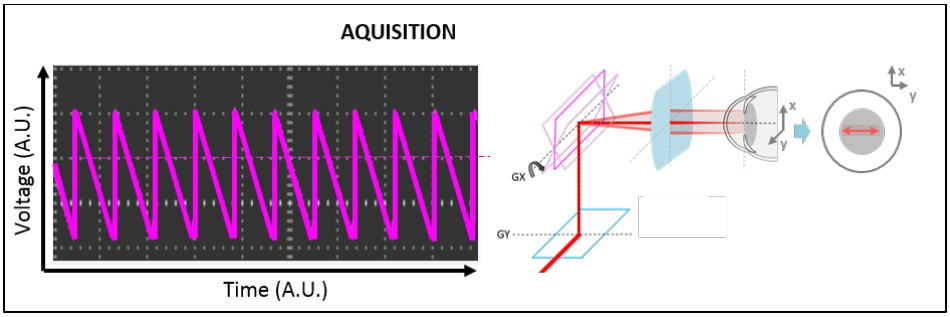

Figure 20 Measured X-galvanometer control signal waveform for acquisition mode for a 4mm linear scan with 400 A-lines. Each white box represents 25 ms in time and 200 mV in V. The acquisition routine signal is a saw-tooth wave with a sharp rising edge.

The amplitude of the X-galvanometer control signal is directly proportional to the width of the scan, the period is directly proportional to the number of A-lines. Several examples of how the scanning dimensions affect the signal are presented in Table 1 and Table 2. For example; a 4 mm line scan has a peak-to-peak amplitude of 600 mV, while for a 16 mm scan has a peak-to-peak amplitude 2.24 V. The scanning density affects the time required to acquire the frame, for example; a 400 A-line image with 20 inactive A-lines between each B-Scan acquisition can be recorded in 33.6 ms, while an image of the same dimensions and a scanning density of 1000 A-lines has a scanning recording period of 81.6 ms.

Table 1 Measured amplitudes of X-galvanometer control signal for different scanning widths

Scan dimensions	**4 mm**	**10 mm**	**16 mm**
Peak-to-peak Amplitude (V)	0.6 V	1.44 V	2.24 V

Table 2 Measured period of X-galvanometer control signal for different scanning densities (Clock speed = 12.5 kHz, Inactive A-lines = 20)

Scan density	400 A-lines	700 A-lines	1000 A-Lines
Period (ms)	33.6 ms	58.4 ms	81.6 ms

The image parameters including scanning density, length and number of inactive A-scans between each frame acquisition can be adjusted before image acquisition in the parameter selection window of the InVivoVue Software, shown in Figure 17.

We have chosen to have our control electronic respond to the X-galvanometer control signal. It is critical that the optical switch only move during the fly-back time of the scan (Figure 16). Otherwise the camera will record a series of A-lines as the optical switch is changing positions and not aligned with a reference mirror.

The fly-back time is an adjustable parameter with the InVivoVue software: the user can choose to increase the number of Inactive A-lines between each frame acquisition. The default parameter of 20 Inactive A-lines for acquisition is maintained since it is also the number of inactive A-lines during alignment. The number of inactive A-lines during alignment cannot be adjusted. Designing for this constraint makes the control system work for both alignment and acquisition modes without introducing extra complexity to the system.

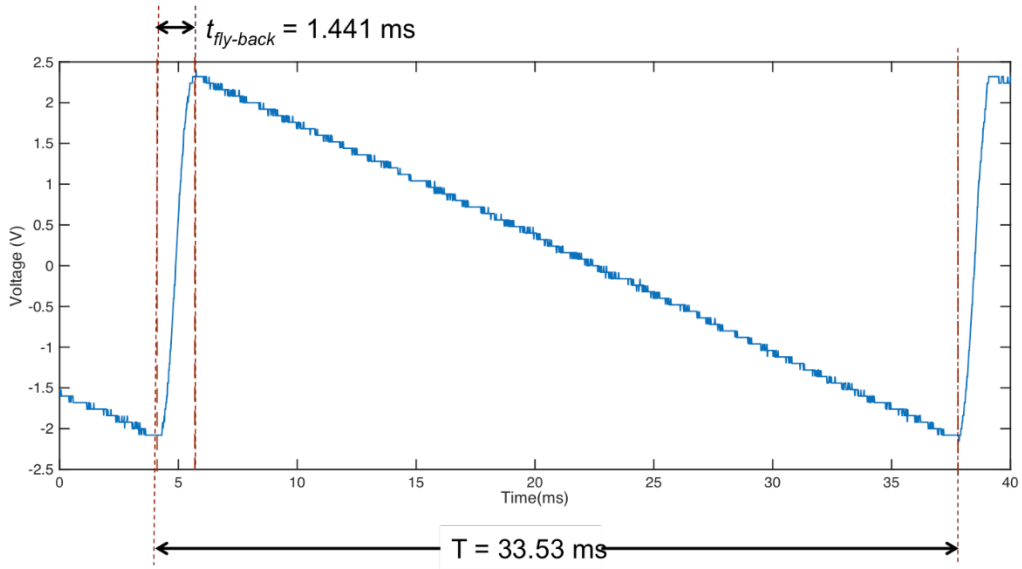

Figure 21 One acquisition waveform for a 400 A-lines/16 mm scan. The rise time of the waveform is marked as $t_{fly\text{-}back}$ and corresponds to the time during which the OCT system is not acquiring images. The fly-back time, $t_{fly\text{-}back,}$ is 1.441 ms, and the Period, T, is 33.53 ms (Camera speed = 12.5 kHz).

The fly-back time was measured for an acquisition of 400 A-lines and 20 inactive-A-lines; these parameters represent the shortest fly-back time the control unit will have to respond within, and thus the most aggressive constraint. With the camera set to an operating speed of 12.5 kHz, each A-line takes 80 microseconds to acquire: resulting in a 1.6 ms fly-back time for the previously mentioned dimensions. Measuring the fly-back time with an oscilloscope, results in a 1.441 ms fly-back time, which is sufficiently close to our theoretical calculation. The measured waveform is shown in Figure 21.

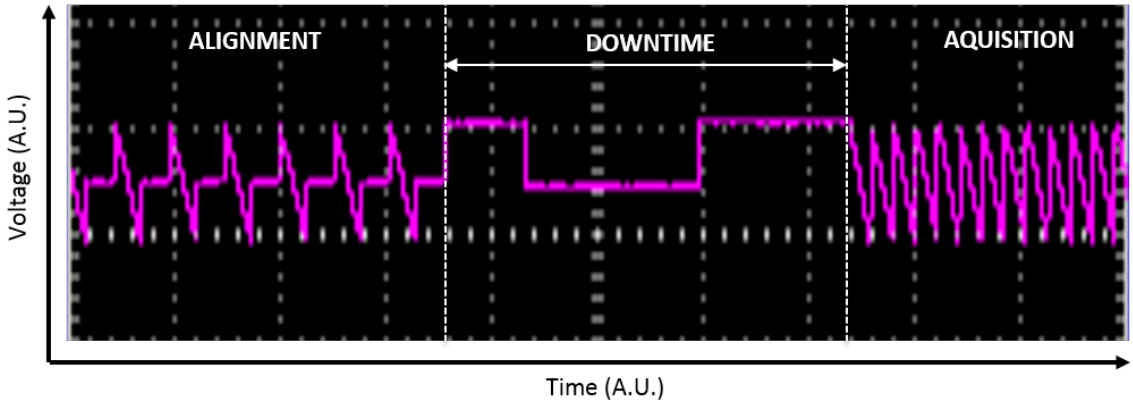

Figure 22 Waveform for alignment, then acquisition.

Another requirement for the control electronics is to differentiate between alignment and acquisition modes in order to trigger an accommodation stimulus change during alignment only. In alignment mode, the shape of the X-galvanometer control signal is different from the same signal during acquisition mode, as shown in Figure 19 and in Figure 20. Additionally, when the system switches from alignment to acquisition mode, there exists a "downtime" in the X-galvanometer control signal as shown in Figure 22. The length of time the downtime lasts varies among acquisitions, but is always measured between 300 ms and 1000 ms.

3.1.2 Optical Switch Input: Z- Galvo Control Board

The optical switch, shown in Figure 23, has been assembled to focus on three areas of interest in the eye: The cornea, the crystalline lens and the retina. In order to provide different depths of the imaging system, three reference mirrors were arranged radially about a mirror mounted on a precision galvanometer (Z-galvanometer).

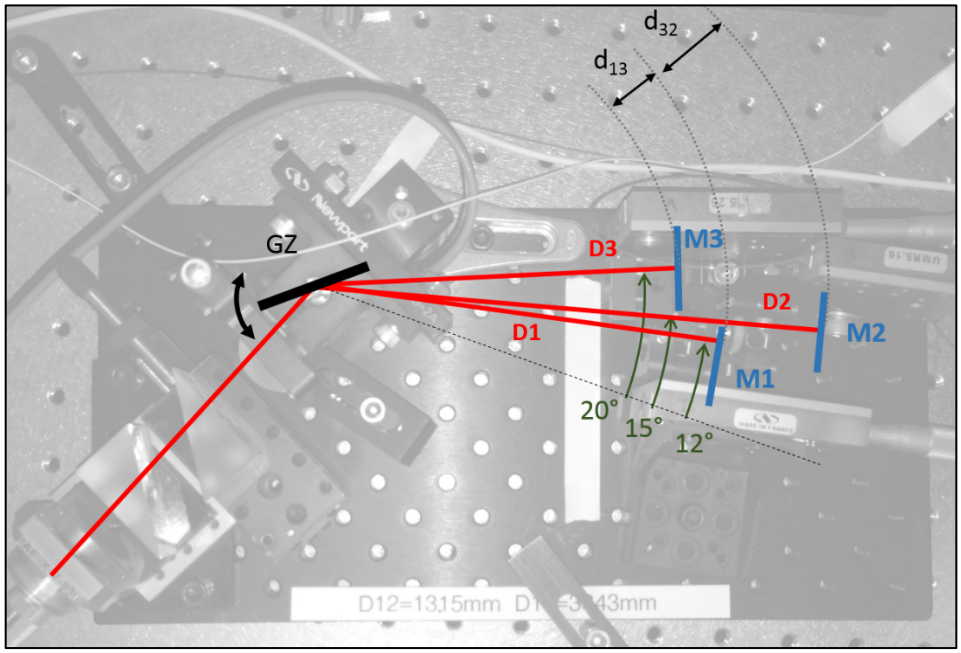

Figure 23 The reference mirrors (M1, M2 and M3) are radially distributed about the galvanometer-mounted mirror (GZ) and their respective delay lines are D1, D2 and D3. The Optical Path Difference (OPD) between each mirror is marked as d_{13}= 13.15 mm and d_{32} = 38.43mm. The values for these distances are given in section 2.3.4.

The Z-galvanometer used to control the galvanometer-mounted mirror assembly was purchased through Cambridge Technologies (6210H, Cambridge Technologies, Inc.) and is controlled by a Cambridge Technology Servo Driver (Model 67121, Cambridge Technologies, Inc.). The driver has a ± 10 V input range and position input scale factor of 0.5 volt/degrees; the driver can rotate a servo 40 degrees total with high precision. As in the transversal scanning block, the angular position is directly related to the input voltage to the servo driver.

During an acquisition, each reference mirror must be precisely aligned to maximize the light that is coupled back into the interferometer from the reference arm: in order to ensure the most efficient coupling, the reference mirror must be perpendicular to the light beam.

We want to determine the three exact voltages necessary to control the Z-galvanometer. To do so, an experiment was performed to measure the required voltage

input to the servo driver. A schematic of the experimental setup is shown in Figure 24. The reflected spectrum shown in the figure is recorded by the line scan camera and shows intensity on the Y axis and pixel number on the X axis; recall that in SD-OCT, the spectrometer uses a diffraction grating to disperse the light into spectral components and the line scan camera records the intensity of a discrete spectral range on each pixel. The sum of the intensities of each spectral component is directly proportional to the intensity of the light reflected into the interferometer.

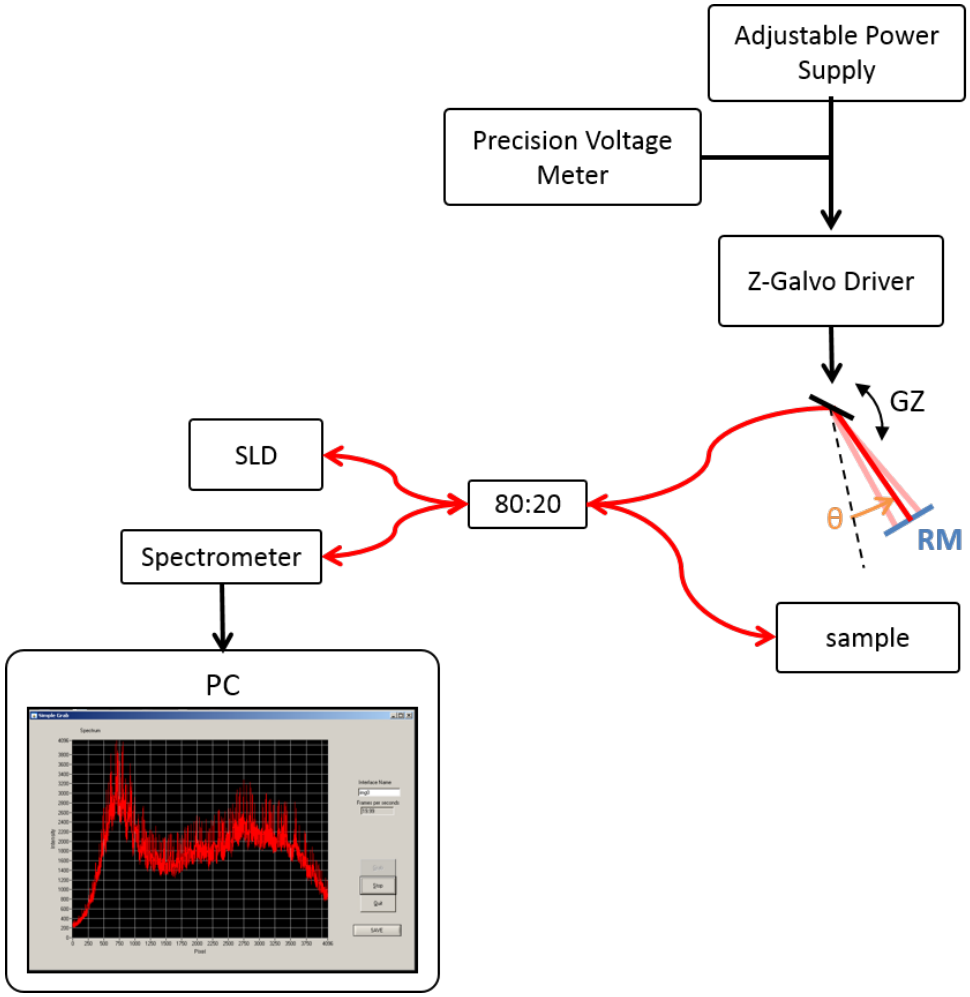

Figure 24 Schematic showing the setup of the experiment used to characterize the precision voltage inputs required to position the Z galvanometer mirror for the highest coupling efficiency. The precision voltage supply is adjusted manually, adjusting the angular position of the Z-galvanometer (GZ), which then translates the reference beam across the reference mirror (RM). The reflected spectrum from the reference mirror is recorded using a LabVIEW GUI on the PC.

- A precision manually adjustable voltage supply (HP 6236B Triple Output Power Supply) was used to power the Z-galvanometer Servo Driver and adjust the input voltage to the driver. The voltage was monitored with a Precision Volt Meter (RIGOL DM3068 Digital Multimeter, 6 ½ digit resolution, 0.35 mV precision)
- The reflected spectrum acquired by the camera was displayed on the computer and stored with custom-made LabVIEW software.
- The voltage was adjusted until a non-zero reflected spectrum was seen on the computer, the voltage was roughly adjusted until the spectrum was maximized, and this was recorded as a rough estimate of the voltage required for maximum coupling efficiency.
- 100 mV sampling window was set around the rough estimate of the maximum coupling efficiency with a sampling resolution of 2 mV.
- The reflected spectrum was recorded every 2 mV. The spectral components recorded have an amplitude related to the signal's intensity, and to that end, the spectral components were integrated over the length of the spectrum to produce a value of normalized intensity.
- Normalized intensity at each voltage input was plotted versus the input voltage to the Servo Driver and a Gaussian fit was applied to the plot. The recorded intensity distributions are found in Figure 25, Figure 26, and Figure 27.
- The voltages required to record the maximum normalized intensity as well as the voltages that allow for 90% and 95% of the voltage related to the

peak intensity were recorded and are listed in Table 3, Table 4, and Table 5.

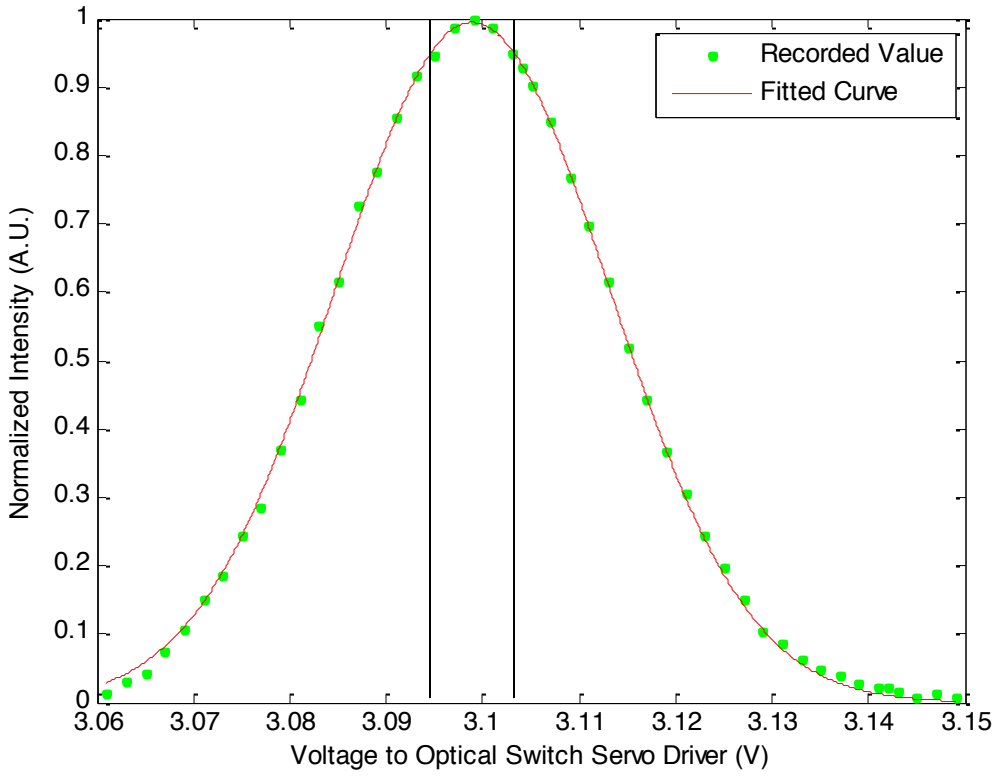

Figure 25 Reflected Intensity distribution for M3. Peak Intensity was recorded at V = 3.099 V The vertical lines correspond to the voltages at which the Gaussian fit of the normalized intensity is equal to 0.95.

Table 3 The recorded voltage input to the Optical Switch Servo Driver to achieve a 90% and 95% coupling efficiency for the reference mirror, M1.

M1 (Lens)	V ($I = I_{max}$)	Min	Max	Δ
90%	3.0989	3.0926	3.1053	0.0127
95%		3.0946	3.1032	0.0086

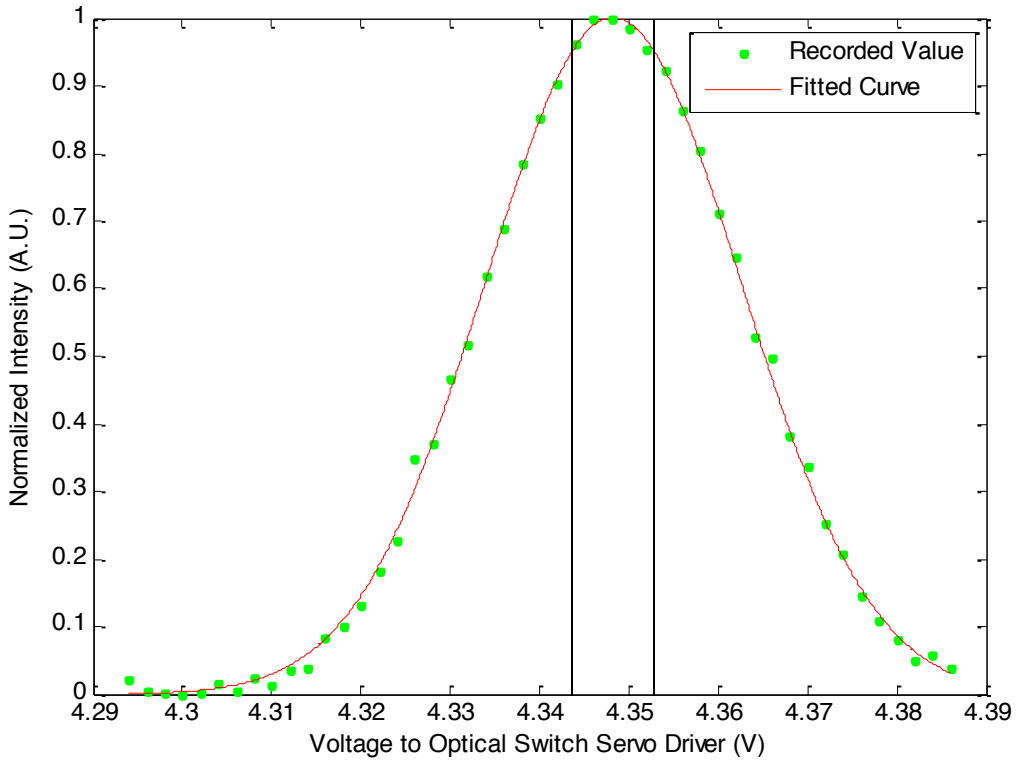

Figure 26 Reflected Intensity distribution for mirror, M2, associated with retina. Peak Intensity was recorded at V = 4.3482 V. The vertical lines correspond to the voltages at which the Gaussian fit of the normalized intensity is equal to 0.95.

Table 4 The recorded voltage input to the Optical Switch Servo Driver to achieve a 90% and 95% coupling efficiency for the reference mirror, M2.

M2 (retina)	V ($I = I_{max}$)	Min	Max	Δ
90%	4.3482	4.3416	4.3549	0.0133
95%		4.3436	4.3529	0.0093

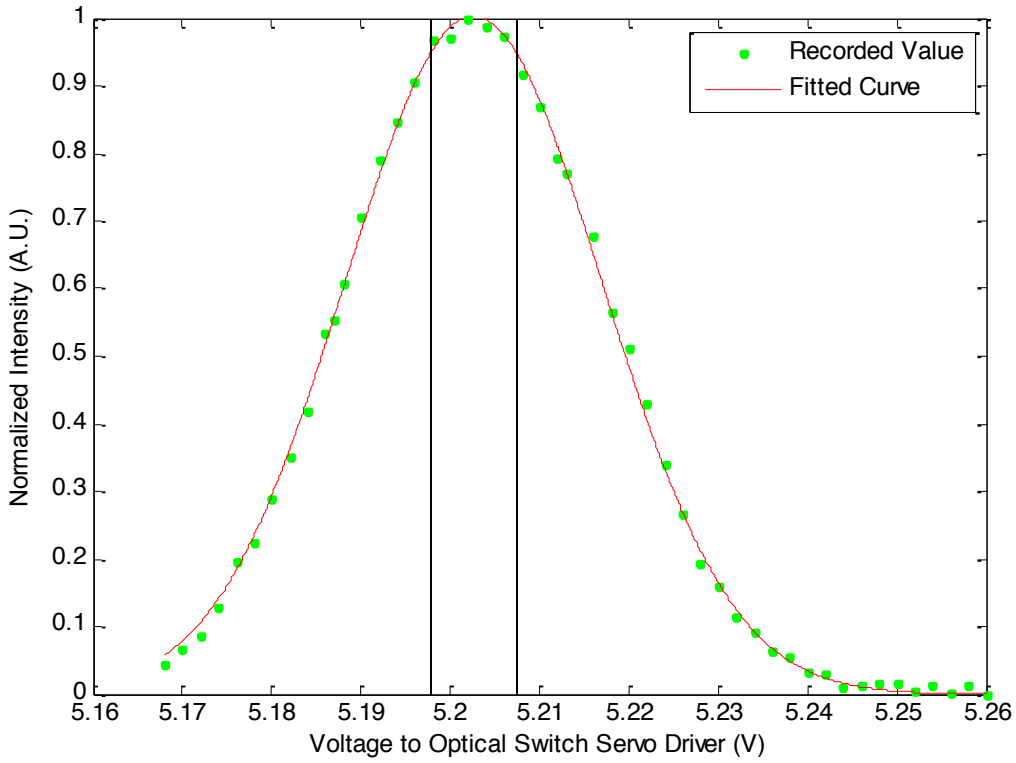

Figure 27 Reflected Intensity distribution for mirror, M1, associated with lens. Peak Intensity was recorded at V = 5.2026 V. The vertical lines correspond to the voltages at which the Gaussian fit of the normalized intensity is equal to 0.95.

Table 5 The recorded voltage input to the Optical Switch Servo Driver to achieve a 90% and 95% coupling efficiency for the reference mirror, M3.

M3 (Cornea)	V ($I = I_{max}$)	Min	Max	Δ
90%	5.2026	5.1959	5.2093	0.0134
95%		5.1979	5.2073	0.0095

Once each reference mirror was aligned, the corresponding control voltage was recorded in Table 6. The corresponding tolerances in the table correspond to the voltages which produce intensities that are at least 95% of the peak normalized intensity. This tolerance is chosen to maintain good image quality within the system.

Table 6 The input voltages required for the optical switch galvanometer driver board and the voltage tolerance allowed to ensure a 95% coupling efficiency back into the interferometer.

Area of Interest	Ideal Control	Voltage

	Voltage	tolerance (±V)
Lens (M1)	3.0989	0.0043 V
Retina (M2)	4.3482	0.00465 V
Cornea (M3)	5.2026	0.00475V

From these specifications, we want to design the output of our control unit to be a step-function alternating between three voltages that correspond to the mechanical degrees of the galvanometer in Table 6. For each scan along X, we need to maintain stable consecutive voltages to the galvanometer driver corresponding to the voltages in Table 6, within the tolerances listed. The control unit must switch between those voltages quickly enough so that the optical switch mirror is only moving during the X-galvanometer's fly-back time. A simulation of the signal desired is shown in Figure 28. The sequence of the signal and the number of mirrors used during the imaging process can be changed with software.

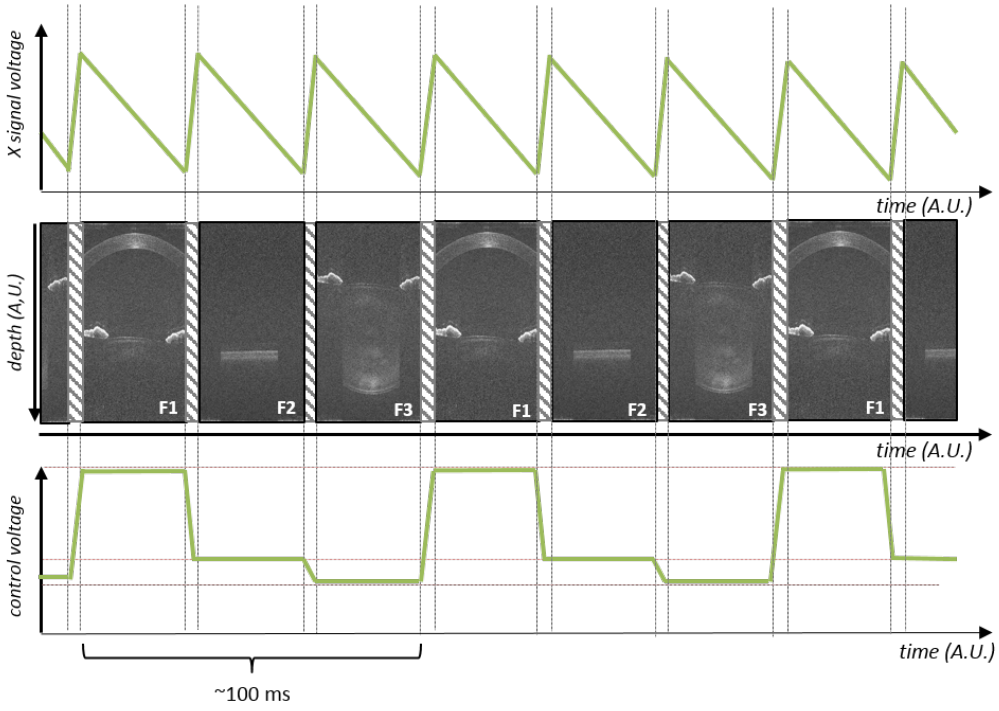

Figure 28 (Top) Schematic of the X-galvanometer control signal. (Middle) Corresponding frame acquisitions desired. F1 is the frame captured when the delay arm is positioned to reflect off of M1 in Figure 23. F2 corresponds to M2 and F3 correspoinds to M3. (Bottom) Schematic of the desired Optical Switch Control Signal voltage: Each delay mirror requires a stable voltage for the duration of acquisition.

3.1.3 Accommodation Stimulus Signal

As described in section 2.3.3 the system is outfit with an accommodation target capable of switching between two accommodation stimulus states. Currently, the electronic responds to the user pressing the foot pedal. The electronic can also be triggered by shorting the control input pins (Top right of Figure 29). In order to trigger the stimulus to change, we must require a signal that will short the input pins after a programmed number of frames acquired.

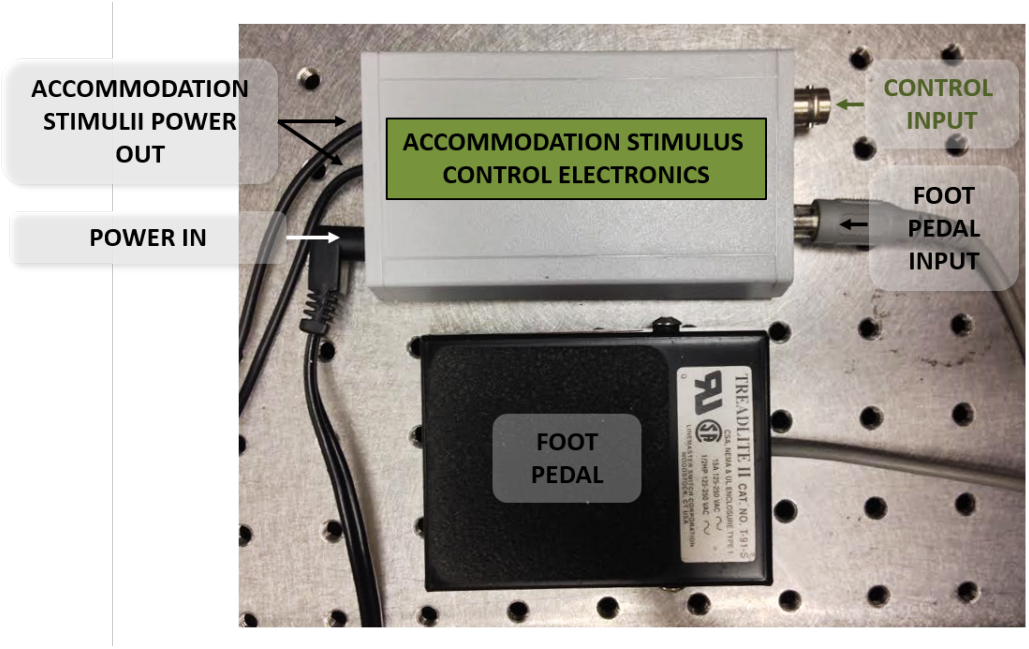

Figure 29 The existing accommodation stimulus control electronics. The accommodation stimulus unit switches accommodation stimuli by alternating the provided power to one of two LEDs which are used to retro-illuminate different targets. The switching can be triggered by pressing the foot pedal or by shorting the pins on the control input jack.

The Accommodation Stimulus electronics trigger a switch event by introducing a falling edge into a logic block by way of shorting the two input pins. A simple schematic is shown in Figure 30; one pin is connected to a pull-up resistor while the other pin is connected to ground.

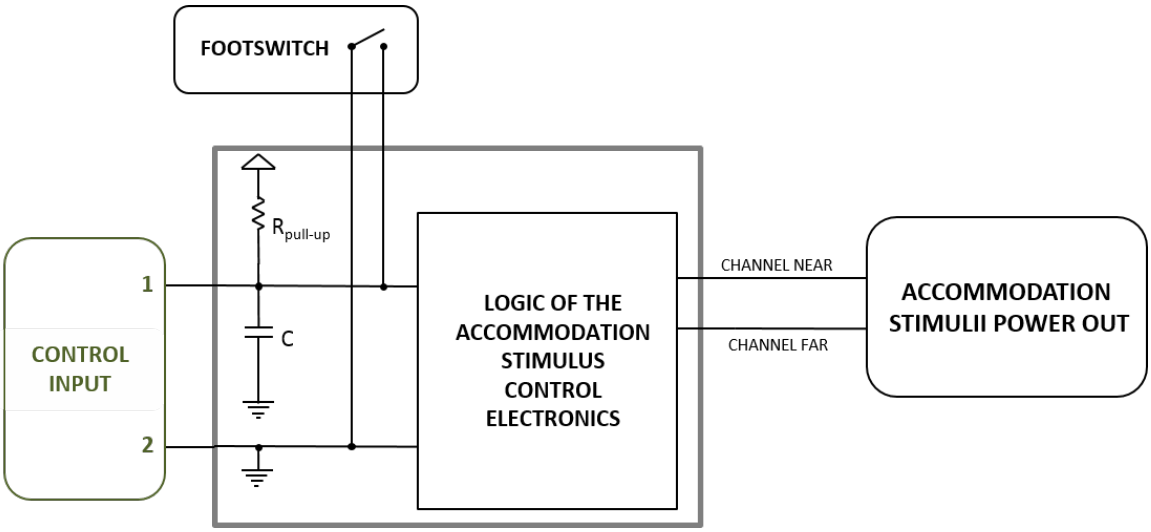

Figure 30 Internal electronics of the Accommodation Stimulus Control Electronics

3.1.4 Clock Signal

In order to synchronize all the parts of the extended-depth OCT system, we chose to run every component on the same clock signal. The line scan camera has the option of being internally or externally controlled by a clock signal. Every other system in the OCT system uses the clock from the line scan camera as the master clock signal. To reduce complexity and ensure precise synchronization, we drive the system clock (CLK) with the microcontroller inside the control unit instead of detecting the clock signal from the line scan camera. In our experience, an imaging speed of 12.5 kHz produces the best compromise between speed and image quality.

3.2 Electronic System Overview

The electronic control unit is required synchronize the various elements of the SD-OCT device to allow for extended-depth imaging. The proposed control unit will receive the X-galvanometer control signal from the galvanometer driver board, and will

output control signals for the Z-galvanometer driver board, the accommodation stimulus and line scan camera as shown in Figure 31.

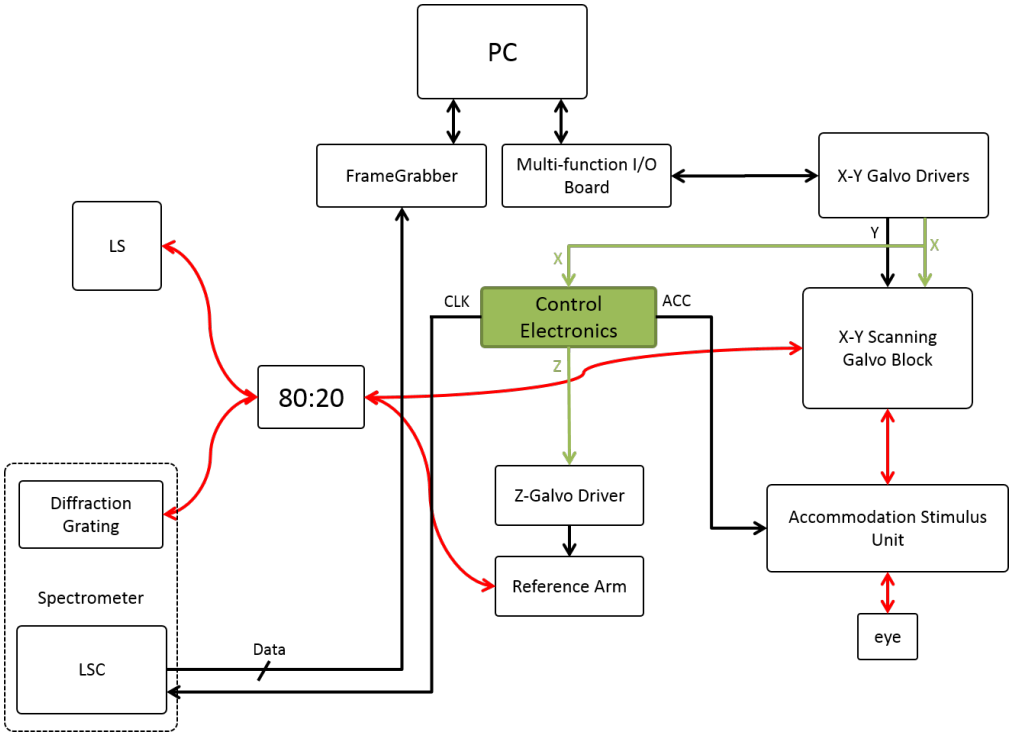

Figure 31 Shows a schematic overview of the entire OCT System. Digital signal lines are shown in black. Analog signal lines are shown in green. Optical fibers are shown in red. The control electronics needed to interface the reference arm with a signal named Z, line scan camera (LSC) with the clock signal CLK, The accommodation stimulus Unit with a signal named ACC. SLD: superluminescent diode. LS: light-source.

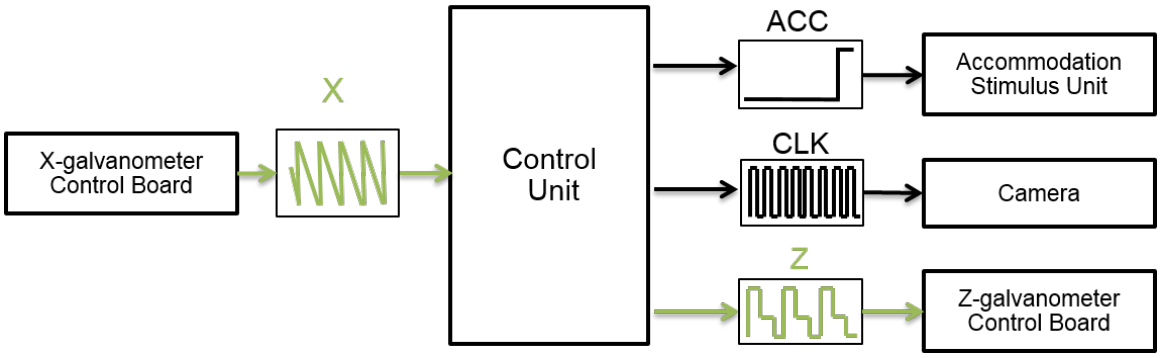

Figure 32 Overview of system electronics. The system responds to an analog saw-tooth wave (X) and outputs an analog step-wise function (Z) and two TTL signals: ACC provides a step change to trigger the accommodation stimulus and CLK provides an adjustable high frequency clock signal to power the clock on the line scan camera.

The block diagram of the control unit with its inputs and outputs is shown in Figure 32. The electronic control unit does the following:

1. *Inputs* an analog voltage waveform from the X-galvo control board
2. *Outputs* an analog voltage tri-state square waveform that is used to control the optical switch's galvanometer.
3. *Outputs* a clock signal (CLK) which sets the acquisition speed (A-line rate) on the line-scan camera
4. Triggers an accommodation stimulus change at a specific time during the acquisition.

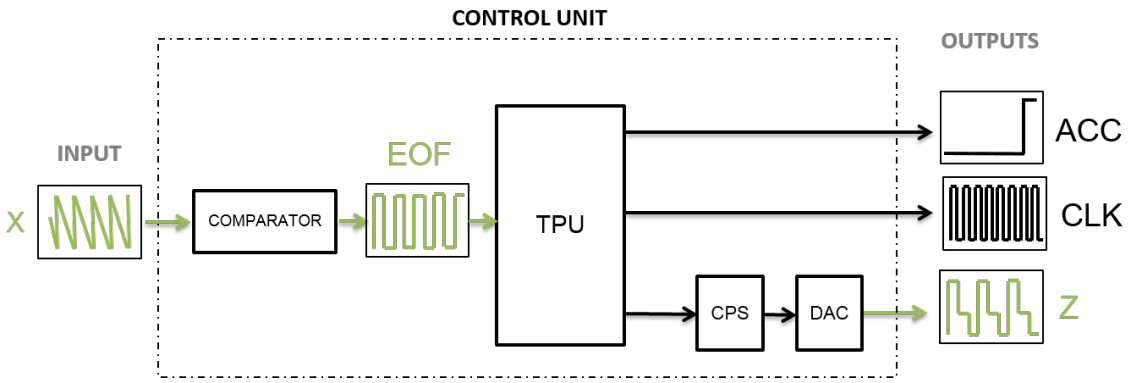

Figure 33 Overview of electronic system which uses three sub-systems to decode the X analog input and produce two TTL outputs: ACC (Accommodation stimulus) and CLK (clock, controls the line scan camera speed) and one analog output, Z. A: Comparator Block. B: Time Processing Unit and C: Cross point switch and Digital-to-Analog Converter.

The control unit is comprised of four subsystems, shown in Figure 33:

1. A Comparator block that receives the X galvo signal and translates it into an end-of-frame (EOF) signal with the same period of the x-galvo waveform.
2. A Time-Processing Unit (TPU):
    - A microcontroller inputs the EOF and launches a software routine to sequentially change the galvanometer voltage on each falling edge of EOF.
    - Interprets whether the OCT is alignment or acquisition mode.
    - Outputs a 4-bit digital code that encodes the geometry for the 3 positions of the optical switch galvanometer.
    - Outputs a CLK signal that dictates the speed on the line scan camera.
    - Triggers an ACC signal at specific point in time during acquisition.
3. A Cross-point Switch (CPS) codes and bit-pads the 4-bit code generated by the microcontroller into a 16 bit input code.
4. The Digital to Analog Converter (DAC) converts the 16-bit code to a precise analog voltage between 0 and 10V corresponding to the necessary angular position of the optical switch galvanometer specified in Table 6.

3.3 Comparator Block

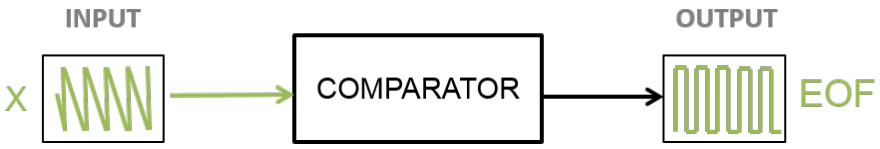

Figure 34 Comparator block diagram

The comparator block is designed to process the X-galvanometer control signal to produce an EOF (end-of-frame) signal with the same frequency to inform the Time-Processing Unit that a frame has been completely acquired.

The comparator block must convert the X-galvanometer analog saw-tooth waveform into a TTL signal. This TTL signal is interpreted by the TPU for the end-of-frame event.

Figure 35shows a simulation of the X-galvanometer control signal and the ideal output from the Comparator Block. The rising ramp of the X-galvanometer control signal corresponds to the fly-back time. Ideally, the end-of-frame event should occur at the most negative voltage reached by the falling ramp of the saw tooth wave to take advantage of the entire fly-back time to move the galvanometer mirror. The most negative voltage varies with the number of A-lines required in the scan as shown in Table 1. The control unit is required to function for a variety of scan densities, and thus the comparator must be designed to account for the variety in scan parameters.

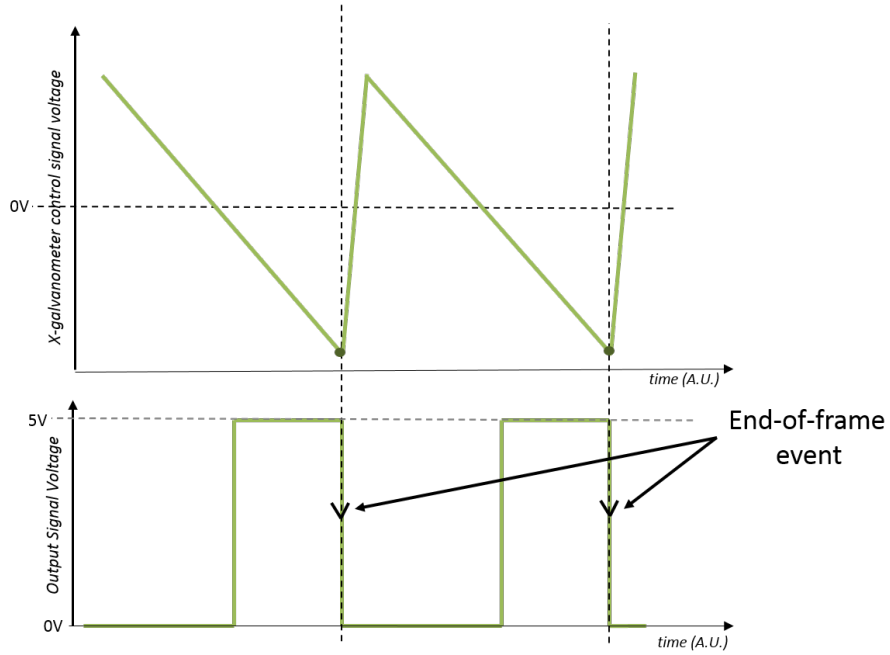

Figure 35 Simulation of the X-galvanometer control signal (top) and the ideal EOF signal generated by the Comparator Block (bottom). For every falling edge of the X-galvanometer control signal, we want to generate a TTL signal of the same period with a sharp falling edge at the zero-crossing point or before to signal the end-of-frame.

In order to convert the saw-tooth X-galvanometer position signal into a digital TTL signal with a falling edge for every end-of-frame, a cascade of a comparator and a hex-inverting Schmitt-trigger was used.

3.3.1 Inverting Voltage Comparator with Hysteresis

In order to accomplish the precise timing of the end-of-frame signal generation, we use a window inverting comparator circuit and set the threshold voltages accordingly. We use a comparator with hysteresis to minimize the circuit's sensitivity to noise.

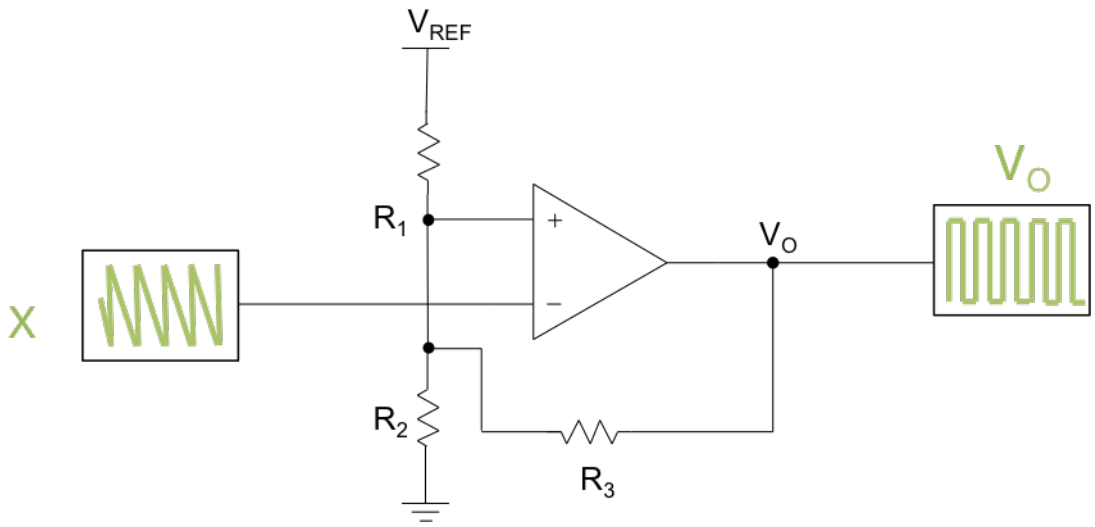

Figure 36 The comparator is shown. Three resistors and a feedback loop are used to set the voltage thresholds and hysteresis.

The inverting window comparator circuit, shown in Figure 36, uses a single op-amp comparator and has a hysteresis window that depends on R_1, R_2, R_3 and the reference voltage, V_{REF}. Hysteresis arises because the voltage seen at the op-amp's positive input varies with the op-amp's output voltage, V_O. Figure 37 shows the inverting window comparator circuit operation. When the input voltage crosses the high threshold, V_{TH}, the output of the op-amp comparator switches from high (V_{OH}) to low (V_{OL}), where V_{OH} and V_{OL} are the thresholds of the op-amp comparator. The input voltage of a periodic signal will proceed to its maximum and then begin to decrease. When the input voltage passes the low threshold, V_{TL}, the output voltage switches to high (V_{OH}).

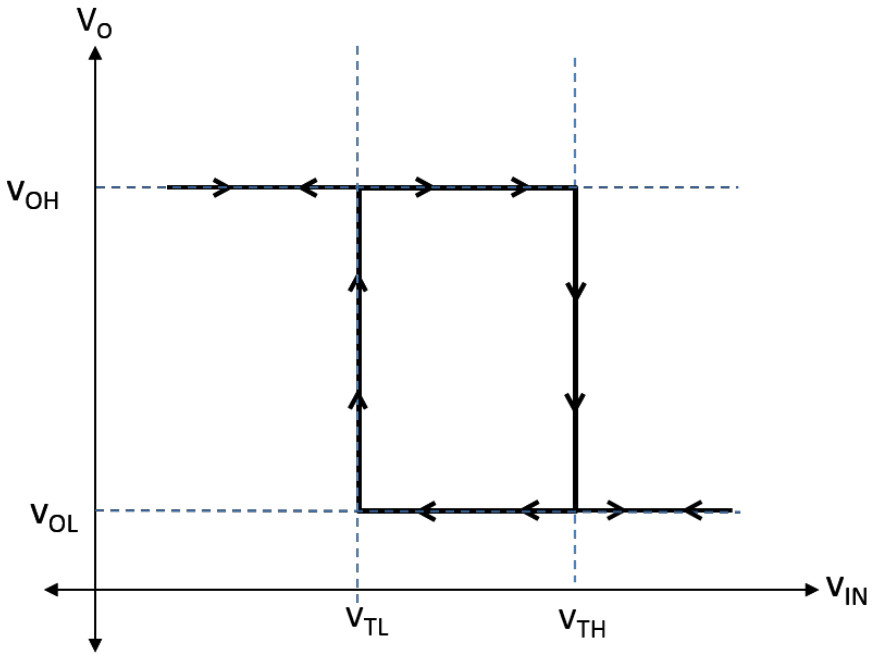

Figure 37 Inverting window comparator circuit operation: The input voltage increases from minimum to maximum. When the input voltage crosses the high threshold, V_{TH}, the output switches from high (V_{OH}) to low (V_{OL}). The input voltage of a periodic signal will proceed to its maximum and then begin to decrease. When the input voltage passes the low threshold, V_{TL}, the output voltage switches to high (V_{OH}).

When V_O is at logic high (V_{OH}, near the supply voltage), the threshold is set by:

$$V_{TH} = V_{REF}\frac{R_1 \| R_2}{R_2 + R_1 \| R_3} + V_{OL}\frac{R_1 \| R_2}{R_3 + R_1 \| R_2} \qquad (8)$$

When V_O is at logic low (V_{OL}, near the ground if the supply is unipolar or near the negative supply voltage), the threshold is set by:

$$V_{TL} = V_{REF}\frac{R_1 \| R_2}{R_2 + R_1 \| R_3} + V_{OH}\frac{R_1 \| R_2}{R_3 + R_1 \| R_2} \qquad (9)$$

Subtracting these voltage from each other gives the hysteresis window width;

$$\Delta V = V_{T,High} - V_{T,Low} = [V_{OH} - V_{OL}]\frac{R_1 \| R_2}{R_3 + R_1 \| R_2} \qquad (10)$$

where $R_1 \parallel R_2 = \left(\frac{1}{R_1} + \frac{1}{R_2}\right)^{-1}$.

3.3.2 Op-Amp Comparator Selection

We select the AD790 Comparator from Analog Devices due to its fast speed and the ability to use negative thresholds. The AD790 accepts a variety of supply voltages and boasts built-in hysteresis to minimize glitches and unwanted oscillations on the output pin.

3.3.3 Comparator Dimensioning

Ideally, the threshold should be near the most negative voltage of the saw tooth wave to take advantage of the entire fly-back time to move the galvanometer mirror. The system is required to maintain the flexibility of capturing images with different scanning widths, thus, the comparator must respond to a variety of amplitudes of the saw tooth wave input. We then set the threshold near the most negative voltage of the smallest peak-to-peak amplitude; a 600 mV peak-to-peak amplitude corresponds to a scan width of 4 mm and has a minimum voltage of -300 mV. We maintain a 100 mV distance from the extremes of the input signal and between the thresholds to account for any noise in the input signal. We thus choose a window width of 100 mV centered at -150 mV. This sets our lower threshold at V_{TL}=-200 mV and the high threshold as V_{TH} = -100mV. The consequent idealized hysteresis plot for these conditions is shown in Figure 38. With this implementation we expect the comparator to produce a square wave with a rising edge when the input crosses -200 mV, and a falling edge when the input crosses -100 mV, as simulated in Figure 39.

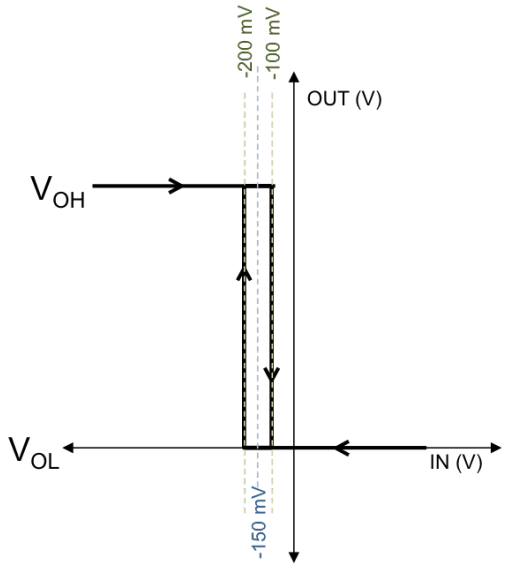

Figure 38 Idealized hysteresis plot

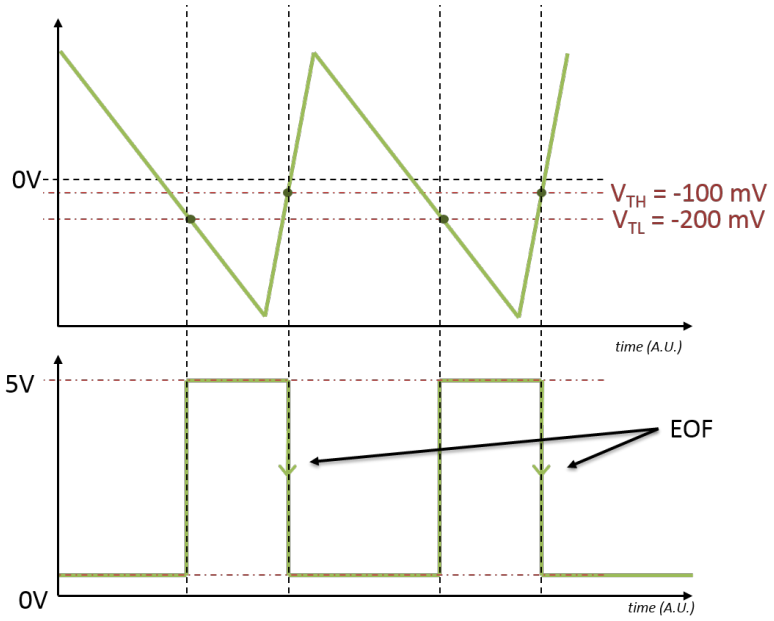

Figure 39 Ideal voltage thresholds and corresponding idealized output signal (bottom) with end-of-frame (EOF) event marked as the falling edge.

Since we are setting a voltage threshold, we must consider all the possible amplitudes of the X-galvanometer control signal wave.

From the datasheet of the AD790 the high output voltage of the comparator is, V_{OH} = 4.45 V and the low output voltage of the comparator, V_{OL} = 0.35 V. We select the feedback resistor, R_3 to be high, at 1 MΩ and solve the series of equations presented in Section 3.3.1 for these values to determine R_1 and R_2. The best-fit values found were R_1 = 27 kΩ and R_2 = 560 kΩ.

We also select a stable negative reference voltage integrated circuit, ADR550A, to supply a stable -5V (V_{REF}) to the comparator.

These values set our theoretical thresholds at V_{TH} =-110 mV and V_{TL} = -220 mV which are near to the ideal thresholds. In the final version of the design, 100kΩ and 10kΩ variable resistors were placed in series with the 560 kΩ and 27 kΩ resistors, respectively – allowing for fine adjustment if needed.

3.3.4 Buffer Gate

To ensure the EOF signal has sharp edges, two cascaded logical inverters with hysteresis were placed between the comparator and the following stage. Adding this element to the circuit provides the added benefit of further de-noising the signal and ensuring a very sharp transient between TTL levels of the signal for input into the microprocessor. The high-impedance of the buffer gate also helps avoid current flow from the comparator towards the next stage while protecting the thresholds of the comparator. We choose a 7404 Hex Inverting Schmitt Trigger, which operates within 15 ns and thus does not introduce a significant delay.

The final comparator block with the comparator and the cascaded buffer gate are shown in Figure 40.

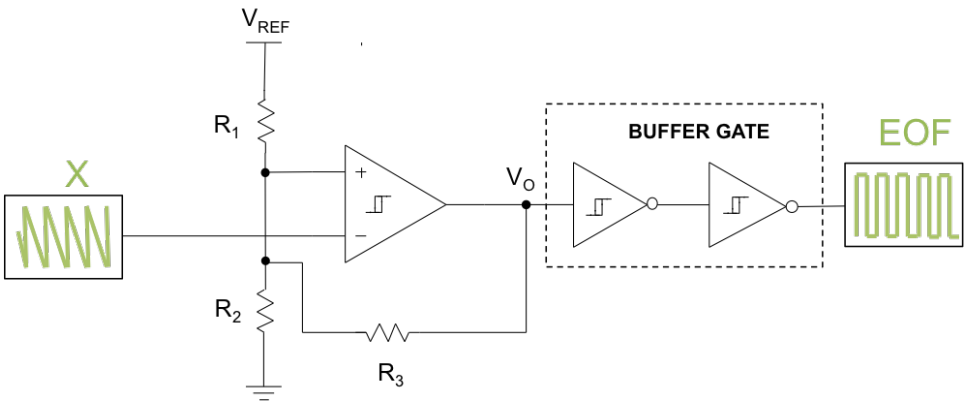

Figure 40 Complete comparator block with buffer gate.

3.4 Time Processing Unit

A Time-Processing Unit (TPU) has been built to interpret the EOF signal output from the comparator block and output an alternating digital code. The TPU, shown in Figure 41, is primarily responsible for generating the four-bit binary code, digitalZ_4, which is used to control the Z galvanometer position. The TPU does the additional tasks of generating a clock signal (CLK) to control the acquisition speed of line scan camera and generating a signal to switch the status of the accommodation stimulus unit (ACC).

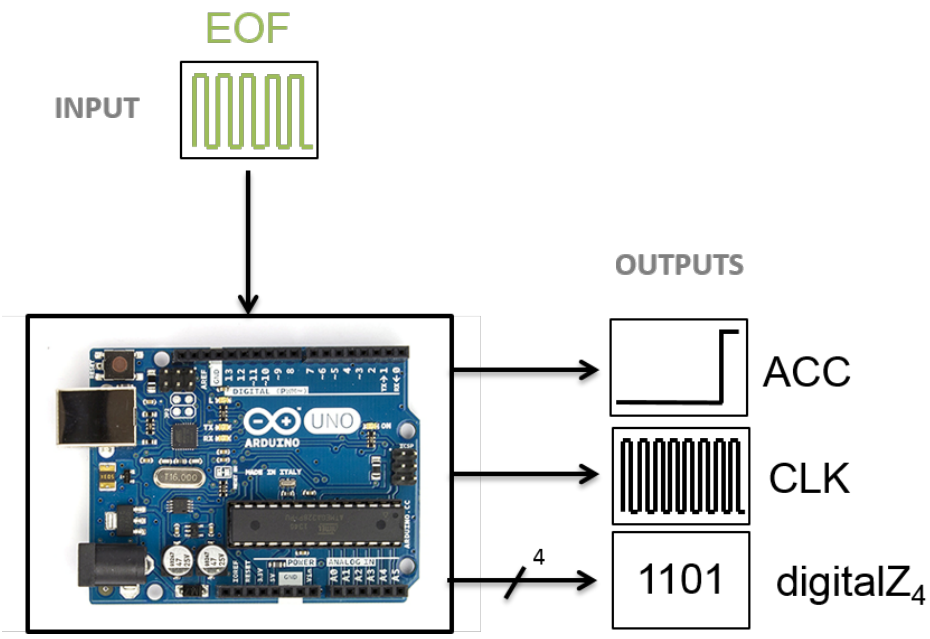

Figure 41 Block diagram showing the inputs and outputs of the Time-Processing Unit.

The TPU is responsible for three tasks:

1. The TPU inputs the EOF signal and must, for every end-of-frame event, control through a four-bit digital code, digitalZ_4, the next galvanometer position of the optical switch. This operation must be done well within the fly-back time of the X-galvanometer to prevent any frame mismatch in the final acquisition.
2. The TPU is also responsible for providing a CLK signal to the Line Scan camera. This CLK signal serves as the master clock for the acquisition process of the entire SD-OCT and ensures all the elements of the device are synchronized. This simplifies the synchronization of the camera with the TPU.
3. The TPU is also responsible for triggering a changing in the status of the accommodation stimulus. In order to accomplish this, the TPU must

be able to understand if the SD-OCT is in alignment or acquisition mode, since the accommodation stimulus change is only provided during acquisition. This detection is accomplished by measuring the downtime in the EOF frame signal. When in acquisition mode, the TPU counts how many frames have been acquired based on the EOF input. The user defines how many frames are acquired before changing the accommodation stimulus, and once that many frames have been recorded, the TPU triggers a stimulus change (ACC).

3.4.1 Microcontroller

The core of the TPU is a microcontroller. The Arduino platform was chosen for the microcontroller because it is reliable hardware at a low price coupled with a breadth of open-source software and literature available on the Internet. It is sufficiently fast (16 MHz) and operates on both digital TTL signals as well as analog signals with an amplitude dynamic between 0 and 5V. At the heart of the Arduino UNO microcontroller lies an ATmega328 8-bit microcontroller with 14 digital input/output pins, 6 analog inputs, a 16 Hz ceramic resonator and a USB jack[30, 31]. The microcontroller can be programmed through specialized C-based software through a USB interface: This allows the controller to be easily and quickly modified.

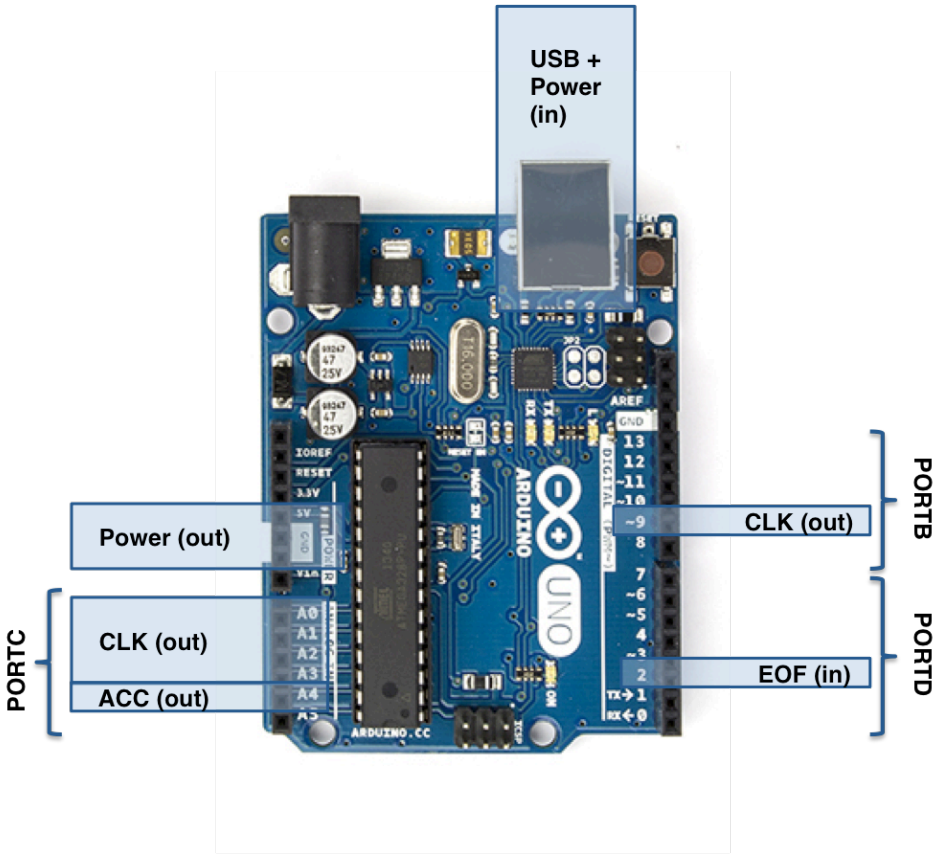

Figure 42 Physical Configuration of the Arduino Microcontroller

The physical configuration of the Arduino microcontroller is shown in Figure 42. PORTC corresponds the I/O pins A0 through A5. These pins can function as both digital and analog I/O pins. We chose to output from the Arduino digitally and convert our output to an analog signal with a more precise digital-to-analog converter (DAC) because the on-board DAC only outputs up to 5V and one analog voltage of at least 5.2V was required as specified by Table 6. The CLK out is wired on Digital Pin 9 on PORTB because it is hard-wired to the hardware timer on the Arduino Board. The Arduino board boasts two pins that are interrupt-enabled: Digital Pins 2 and 3 of PORTD. We connect the EOF signal to Digital Pin 2.

3.4.2 Control Software

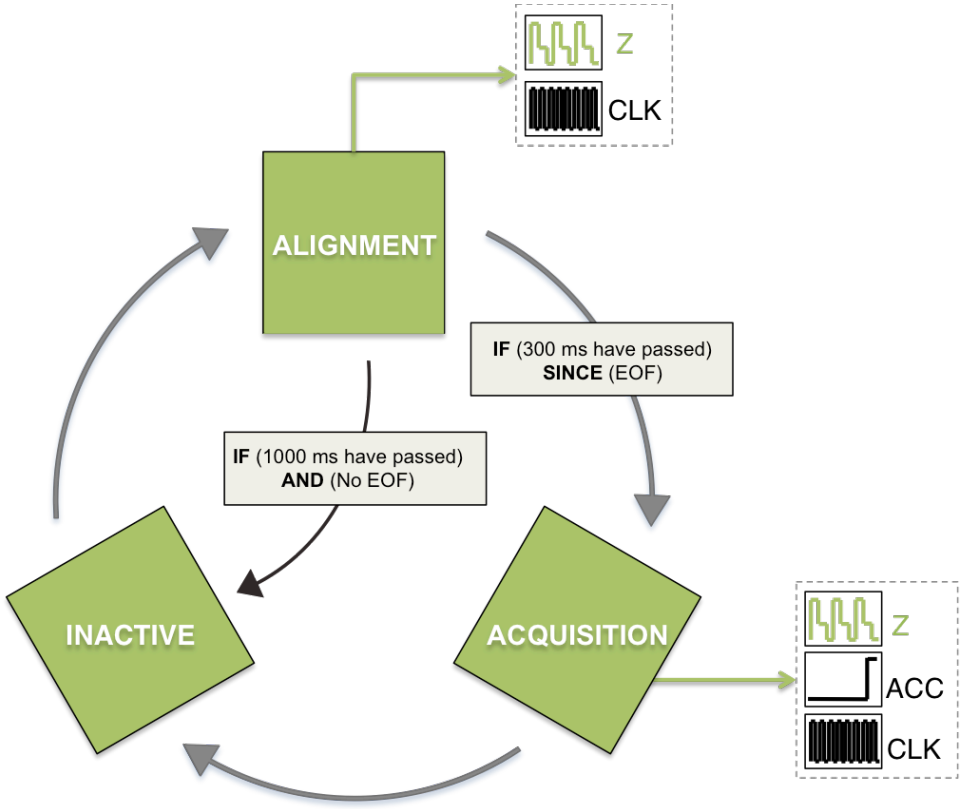

Figure 43 Finite-State Machine diagram showing how the software on the Arduino is designed to work: The software transitions between the three states shown sequentially unless sufficient time (1000 ms) has passed to imply Alignment Mode has ended and Acquisition mode was never initiated, in which case the software skips the Acquisition state.

A custom software routine was designed as a finite–state-machine transitioning between three states (Figure 43). The software uses the input EOF signal to determine if the commercial software is in alignment or acquisition mode, and outputs the Z-galvanometer position code and triggers the accommodation stimulus change if the commercial software is in acquisition mode. The software's timing parameters were set according to the measured downtime between Alignment and Acquisition (Figure 22).

The commercial software always transitions from state 1: Inactive, to State 2: Alignment state and then to State 3: Acquisition state. Unless the user has elected to terminate Alignment state, in which case the commercial software will return to State 1: Inactive. For this purpose it was necessary to implement a time-keeping function to check that sufficient time (at least 300 ms) has passed since the last end-of-frame event to imply that an acquisition could happen soon, and not so much time (no more than 1000 ms) has passed that the system has returned to State 1: Inactive.

The software has been written in a way to optimize the speed of the microcontroller as much as possible:

1. The software detects the falling edge of the EOF signal with an interrupt function.
2. The software responds to the interrupt with an interrupt service routine, which runs a small loop to check how much time has passed since the previous interrupt, and what the last output code was. During alignment, the software compares the current time against a timekeeping function that is constantly running in the background to determine if enough time has passed since the last end-of-frame event to imply that an acquisition is eminent. The downtime shown in Figure 22, between alignment and acquisition varies between 300ms and 1000 ms. If more than 1000 ms have passed since the last end-of-frame event, the software resets the optical switch galvanometer mirror position and prepares for another alignment routine. If more than 300 ms and less than 1000 ms have passed since the last end-of-frame event; the software resets the optical switch galvanometer position and prepares for an acquisition.

3. The software utilizes the Arduino's PortManipulation command, which allows for low-level and faster manipulation of the I/O pins of the microcontroller on the Arduino board. By outputting a single command to PORTC the software can output all 4 bits of digitalZ_4 at once. The output on PORTC includes digitalZ_4 which is used to control the optical scanner mirror position as well as a 1-bit binary pulse for controlling the accommodation stimulus unit (ACC).

If the system is in acquisition mode, a counter in the control software also keeps track of which frame is currently being acquired. Before the beginning of the imaging process, the user can set how many frames during the acquisition routine they would like recorded before triggering a change in accommodation stimulus (ACC).

The microcontroller is also responsible for providing the clock signal (CLK) to the line scan camera. This signal is transmitted to the line scan camera through the FrameGrabber board installed on the computer. The camera is set to an imaging speed of 12.5 kHz, which allows for better image quality.

3.5 Cross-Point Switch and Digital-to-Analog Converter

The last blocks of the Control unit are responsible for converting the digital binary code generated by the TPU to an analog voltage, which corresponds to the voltage necessary to drive the Z-galvanometer according to the vales found in Table 6. As shown in Figure 44, this is accomplished through a cascade of a cross-point switch (CPS) and a digital-to-analog converter (DAC).

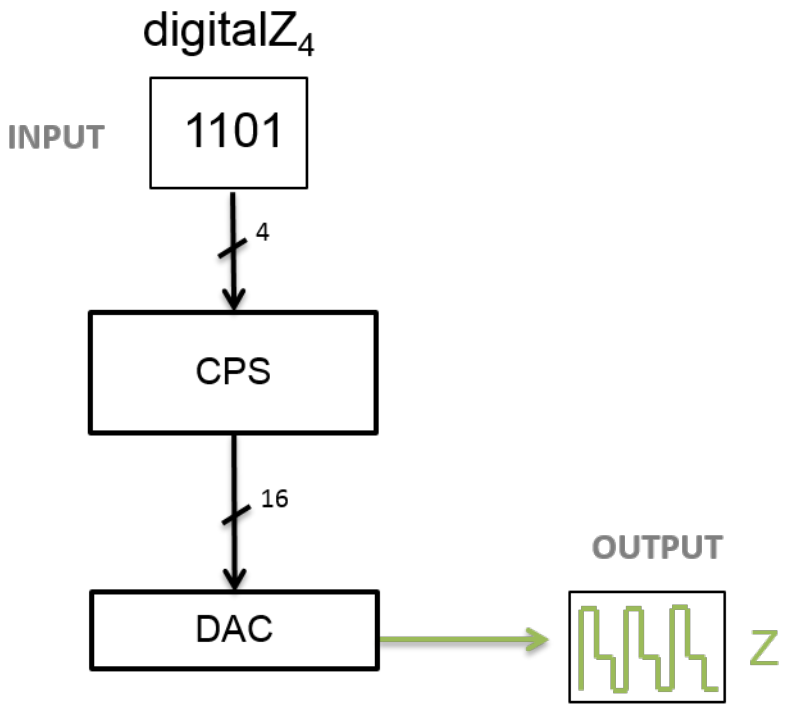

Figure 44 The Cross-Point Switch (CPS) and Digital-to-Analgog Converter (DAC) are placed in series and together accomplish the task of converting the 4-bit digtialZ output from the TPU to an analog voltage, Z.

3.5.1 Digital-to-Analog Converter (DAC)

The Control Unit is designed to interface with the Servo Driver (67121 Cambridge Technologies, MA). The Servo Driver allows for a bipolar position input of ±10V. In our implementation, a fast response time, stable voltage output and high precision are paramount. We chose to implement a DAC with a 16-bit parallel input. An 8-bit DAC would only provide a voltage resolution output of 0.039 V, while the tolerances listed in Table 6 are on an order of magnitude smaller, at 0.004V; the precision afforded by an 8-bit DAC was not sufficient for this application. A 16-bit DAC provides a 0.00015V output resolution, which introduces much more flexibility in setting the output voltages.

We chose the Analog Devices AD669. The AD669 can provide unipolar or bipolar output and features an on-board precision Zener reference to ensure stable reference voltage and output and make the AD669 suitable for signal generation applications. The DAC is configured in a unipolar configuration, which enables control the analog output with a resolution of less than 0.153 mV.

In order to generate the desired voltages listed in Table 6, we require the following 16-bit digital binary input to the DAC (Table 7).

Table 7 The Voltages required for the optical scanner control and the corresponding 16-bit input for the DAC

Area of Interest	Voltage Input Required (V)	DAC input (digital binary)
Cornea	5.202	1000010101000110
Retina	4.345	0110111101010101
Lens	3.097	0100111101010100

3.5.2 Cross-Point Switch

The digital-to-analog converter (DAC) chosen requires 16-bits of input to control precisely. The arrangement of the microcontroller limits the digital output to 4 pins. In order to interface the microcontroller and the DAC we implement a cross-point switch (CPS) to bit-pad and route the microcontroller output.

The three 16-bit codes from Table 7 are shown in Figure 45 (left). As is shown in the figure, of the 16-bits necessary to set the necessary outputs for the DAC, only 8 change dynamically during the switching routine.

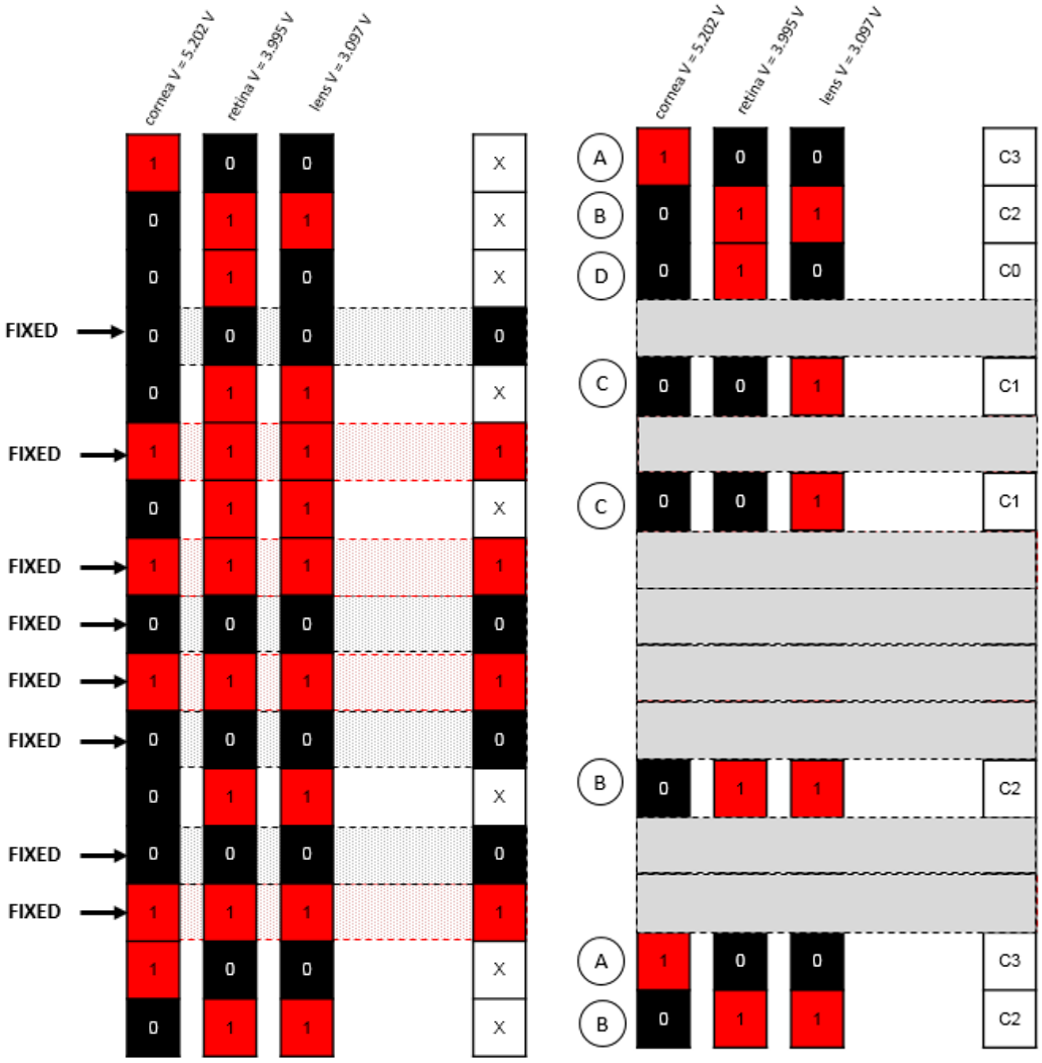

Figure 45 (Left) Setting the Cross-Point Switch requires understanding which input pins to the DAC need to be changed in order to generate the three voltages needed. Shown is a graphical representation of the digital input for each voltage. Most significant bit is at the top. From this graphic it is easy to see 8 pins do not change throughout the switching routine. (Right) Occluding the bits that do not change, we can easily identify how many independent combinations are necessary to produce the three 16-bit codes; A, B, C and D are each independent combinations are then routed to pins C3, C2, C1 and C0 on the Arduino microcontroller, respectively.

Furthermore, inspecting the bits that change, we find there are only 4 independent combinations of those bits. By occluding the unchanging bit and marking the four bit combinations as A, B, C and D in Figure 45 (right), we can more easily identify the four independent combinations. We assign each of these lettered routines to a pin on the output port C of the microcontroller as C3, C2, C1 and C0. From Figure 45, we see that 8 bits stay the same throughout the switching routine, and those 8 bits can be statically

connected directly to +5V or GND. The cross-point switch allows us to only change 4 output pins on the Arduino and route those outputs and +5V (digital 1) and GND (digital 0) to the 16-bit input of the DAC.

The required output code on PORTC for each area of interest in the eye and the final voltages to which they correspond are shown in Table 8.

Table 8 List of the voltages, 16-bit input to DAC and corresponding 4-bit output from the Arduino.

	Voltage Input	DAC input	PORTC			
Area of Interest	Required	(digital binary)	C3	C2	C1	C0
Cornea	5.202	1000010101000110	1	0	0	0
Retina	4.345	0110111101010101	0	1	1	1
Lens	3.097	0100111101010101	0	1	0	0

The final implementation of the CPS is shown in Figure 46.

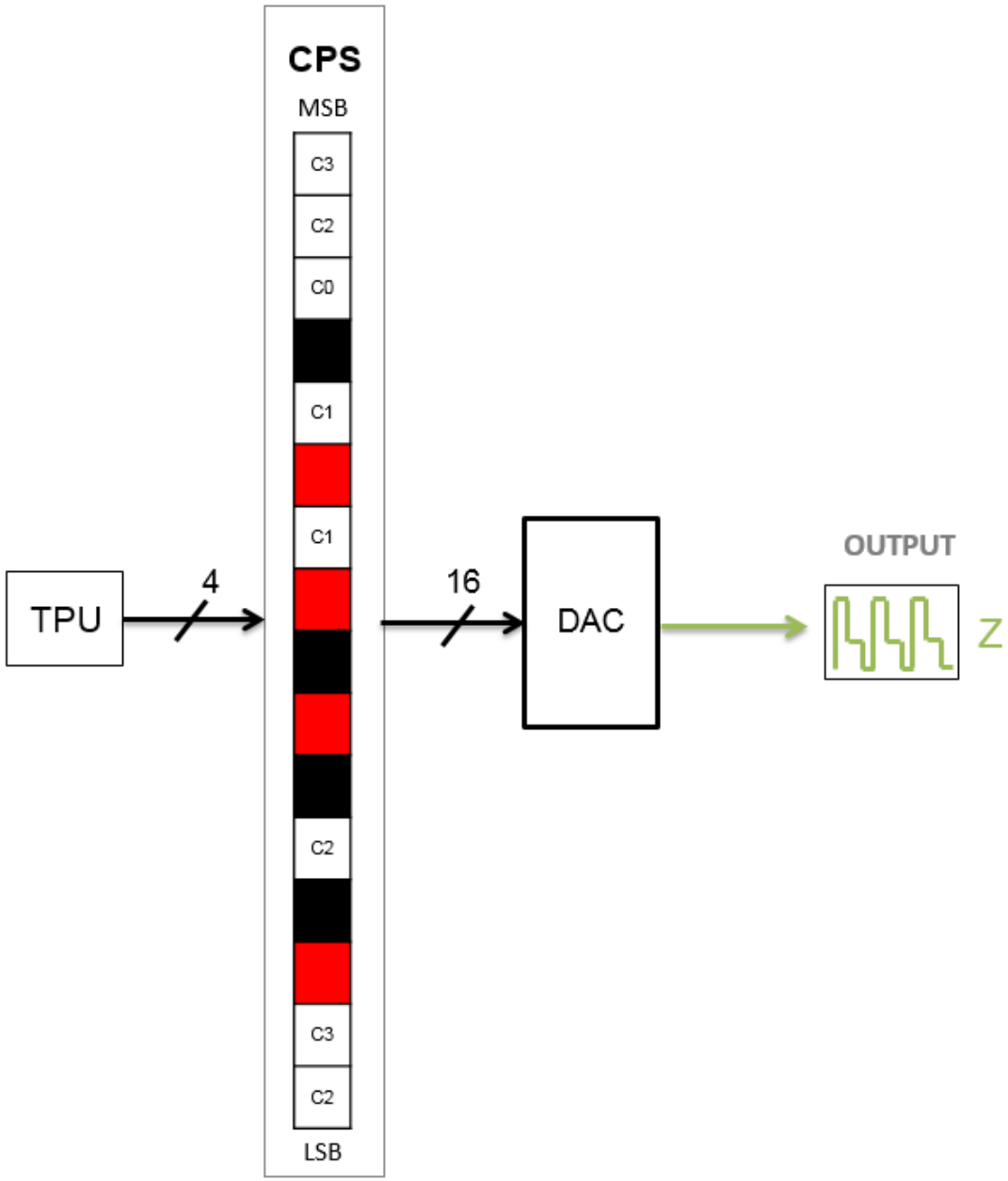

Figure 46 The Cross-Point Switch is shown as a column of 16 bits, converting a 5-bit output signal from the Arduino to a 16-bit control signal to the DAC.

3.6 Accommodation Target Integration Electronics

The circuit provided with the external accommodation target electronics, shown in Figure 30, has been designed to respond to a short of the positive (pin 1) and negative

(pin 2) input pins: pin 1 is connected to ACC_1 in Figure 47, and pin 2 is connected to ACC_2 in Figure 47. To this end, an opto-isolator (4N33) was used to convert the rising edge of the TTL signal from the microcontroller to a short, while keeping the two electronic units electrically isolated. The implementation of the opto-isolator is shown in Figure 47. The resistor, R_F, was dimensioned to ensure the forward current across the opto-isolator did not exceed 10mA as per the specifications of the 4N33. According to the data sheet, the typical forward voltage across the diode is V_F = 1.25 V. The resistor, R_F is dimensioned according to:

$$R_F = \frac{V_{CC} - V_F}{I_F} \tag{11}$$

Solving for V_{CC} = 5V, the maximum output from the microcontroller for the ACC signal and above values, yields: R_F = 375 Ω. We choose R_F = 390 Ω as it is the nearest value of in the series E24 of resistors.

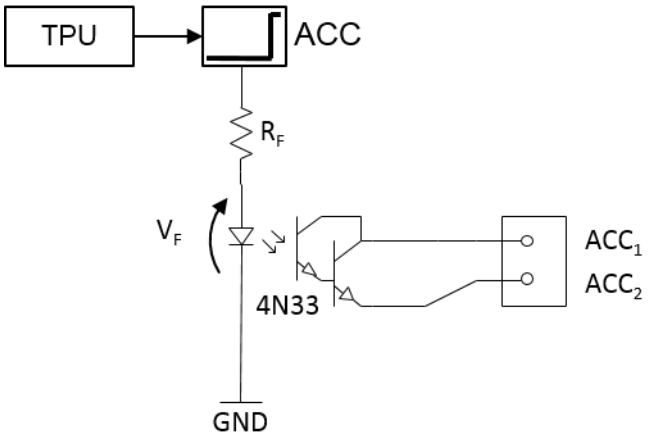

Figure 47 The Accommodation Stimulus target output is sent through an opto-isolator to provide a short across ACC_1 (positive) and ACC_2 (negative) on the Accommodation Stimulus Control Electronics.

3.7 Final Design

The final compiled design of the electronic control unit with all intermediate signals as well as inputs and outputs is shown in Figure 48.

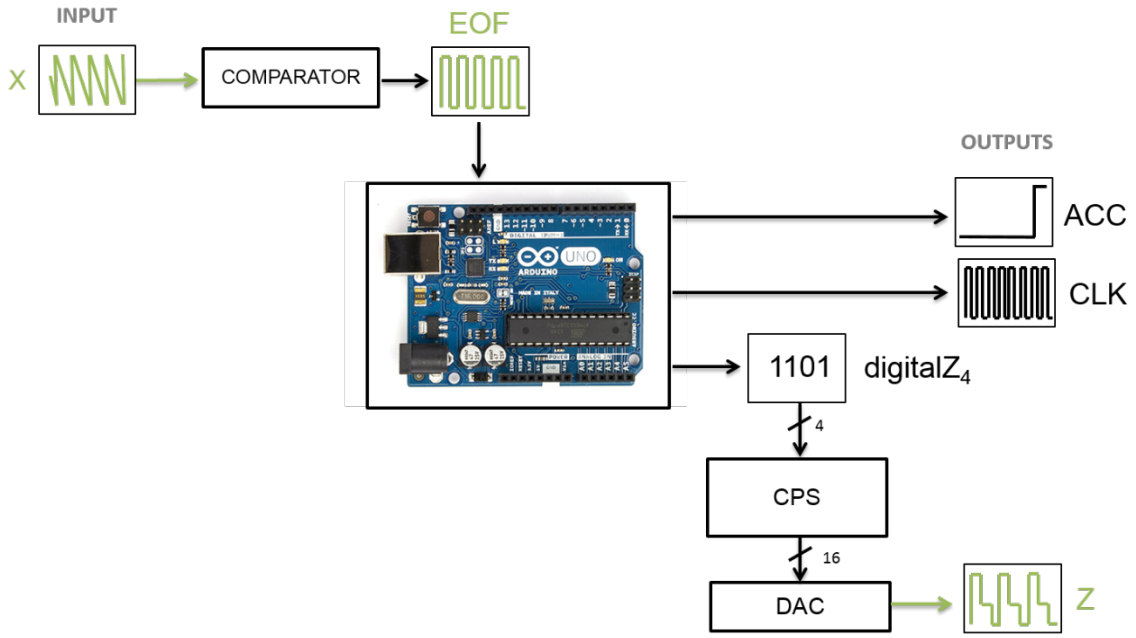

Figure 48 Schematic of the final electronic design featuring all four sub-parts. CPS: Cross-Point Switch, DAC: digital-to-analog converter

Chapter 4

Implementation and Circuit Testing

The electronics were assembled and placed on a Printed Circuit Board (PCB). The PCB was designed using a combination of the ExpressSCH V 7.0.2 and ExpressPCB V 7.0.2 Software, and the PCBs were printed via ExpressPCB.com.

Ultimately, this electronic was integrated into a portable cart where space for electronic components was minimal. Limited space within the existing control box limits the PCB dimensions to 3.8" x 2.5". The circuit designed, along with all the other electronic components, is shown installed into the cart in Figure 49.

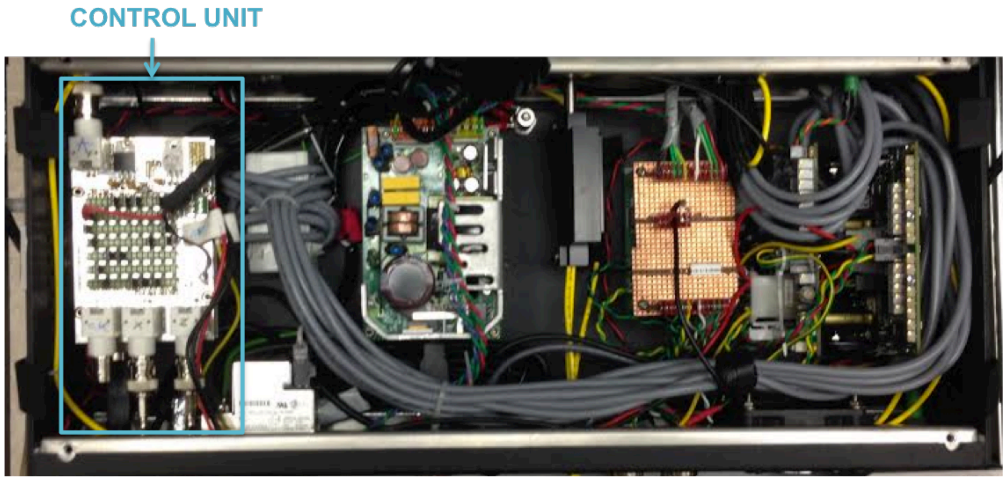

Figure 49 Inside view of the existing control box. The control unit is shown on the left.

The Cross-point switch monopolizes a lot of board space, as do the individual traces for the DAC; to fit all the components and their traces into the existing control box, we were forced to split the electronics into two PCBs. To save space within the existing system control box, we stacked the two PCBs on top of each other using breakaway headers both as physical supports and electrical connections between the boards. The Arduino microcontroller is connected the PCBs via the breakaway headers and is the

most bottom layer of the stack. The vertical organization of the PCBs is shown in Figure 50 and the transfer of signals between them is also marked.

This implementation makes the control unit modular, allowing us to quickly trade out a non-functioning board throughout the testing process. All inputs and output signals exit/enter the electronic through a series of BNC headers placed on the top board.

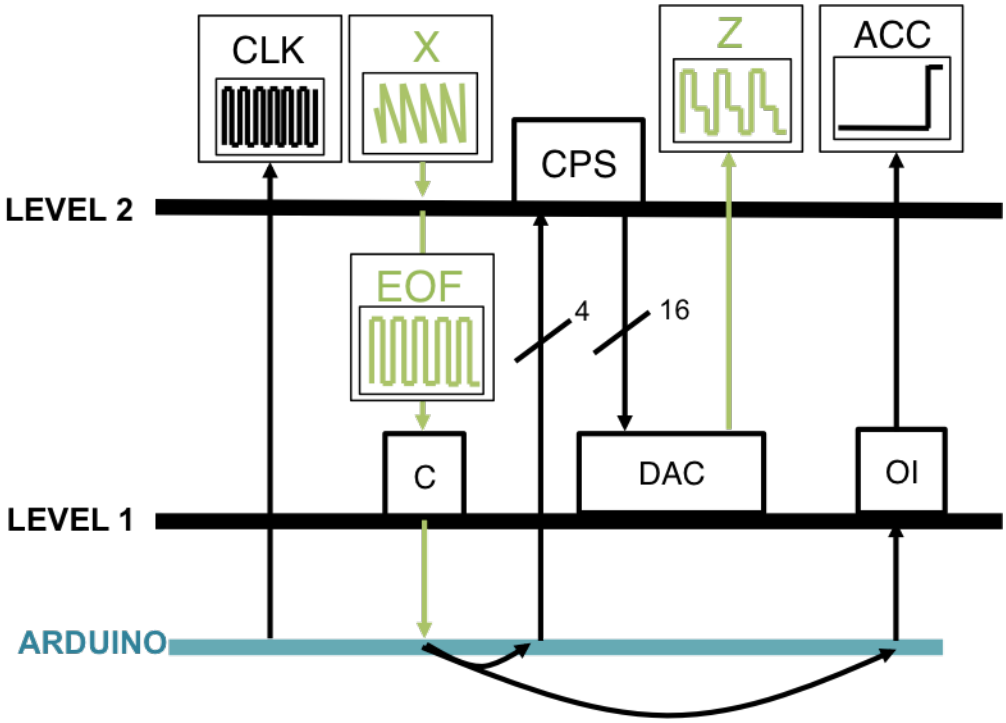

Figure 50 Vertical organization of the control unit. Signals are transferred vertically from one level to the other through a series of headers, which also serve as the physical connection between each level. C: comparator. DAC: digital-to-analog converter. OI: opto-isolator. Green lines indicate analog signals and black lines indicate digital TTL signals.

4.1 Schematic

Schematics for each level of the control unit were created separately. Each schematic file is linked to its corresponding PCB file to auto check the traces on the PCB before printing. All connectors have been labeled with the letter J and a number except for the 16 pins connecting the DAC input and the CPS output. Those are grouped into two connectors of 8 pins each, labeled CPS1 and CPS2. All components were wired according to their respective data sheets, any resistors required by the datasheets were

added and each integrated circuit was mounted with a 0.1 nF capacitor between the V_{CC} and GND terminals as a decoupling capacitor. The DAC requires ± 15V power supply – to this end two voltage regulators (LM7915 and LM7815) were used to convert the existing ±24V power inside the control box for the transverse galvanometer drivers to ± 15V.

Level 1 is shown in Figure 51. Level 2 is shown in Figure 58.

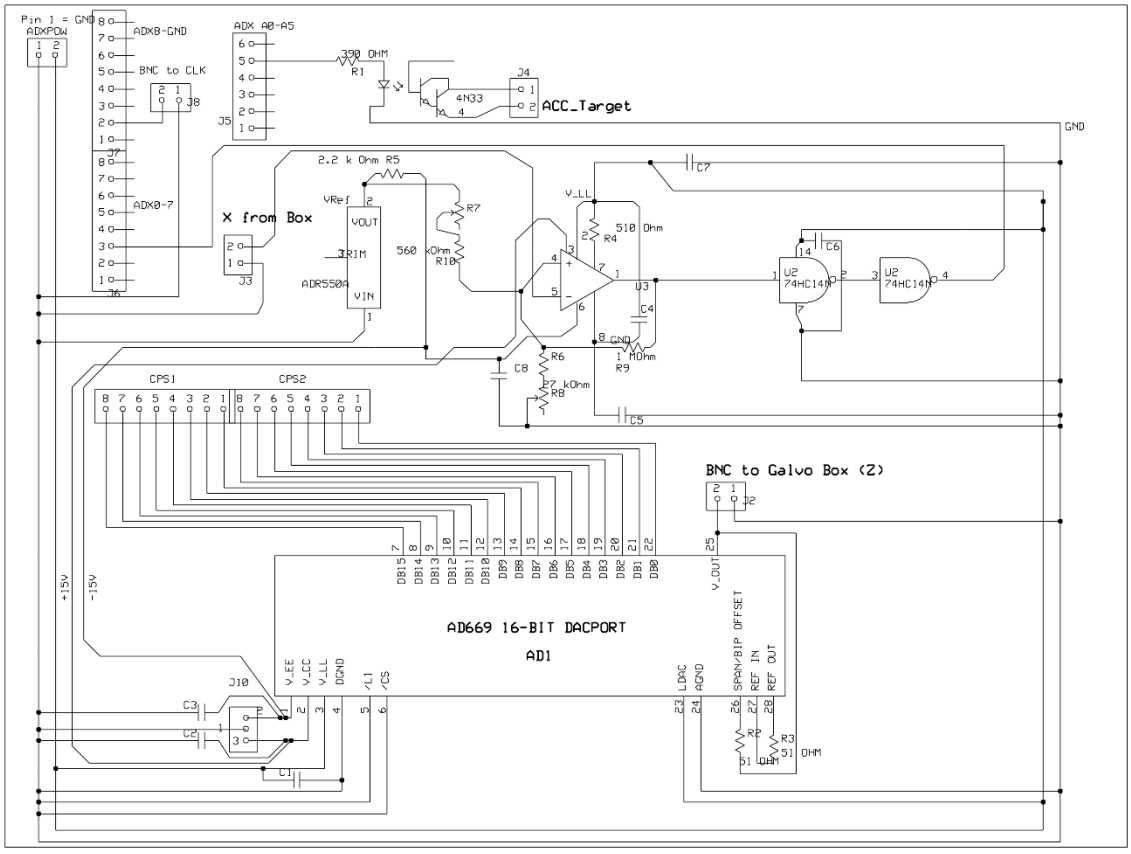

Figure 51 Electrical Schematic of Level 1. Schematic generated with ExpressSCH.

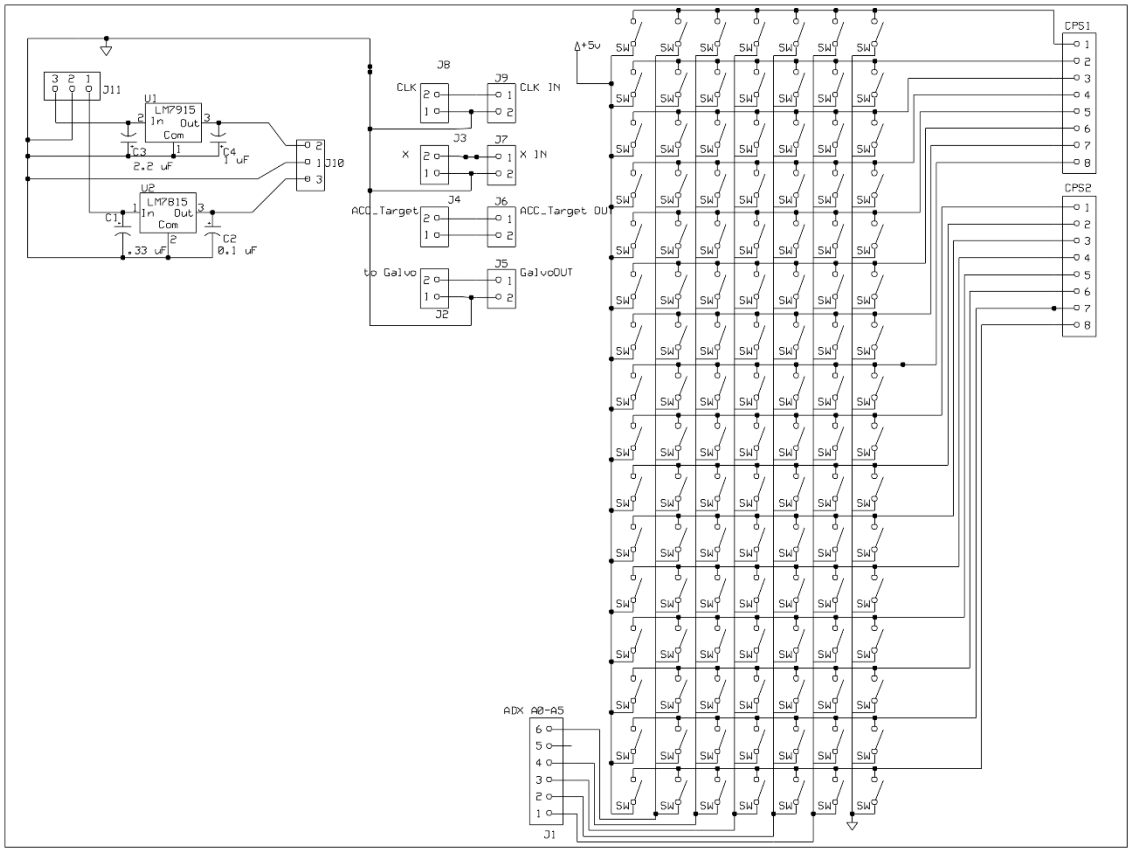

Figure 52 Electrical Schematic of Level 2. Schematic generated with ExpressSCH.

4.2 PCB Design

In order to produce the PCB, the components were laid out in Express PCB.

4.2.1 Level 1

The level directly above the microcontroller is referred to as Level 1 and includes the major components of the Comparator Block, the DAC, and the opto-isolator.

Comparator Circuit

The comparator block, highlighted in Figure 53, includes the AD790 comparator as well as through double hex Schmitt trigger (74HC14N). Additionally, a -5V voltage reference is implemented in the comparator block to provide the negative reference voltage required for the comparator.

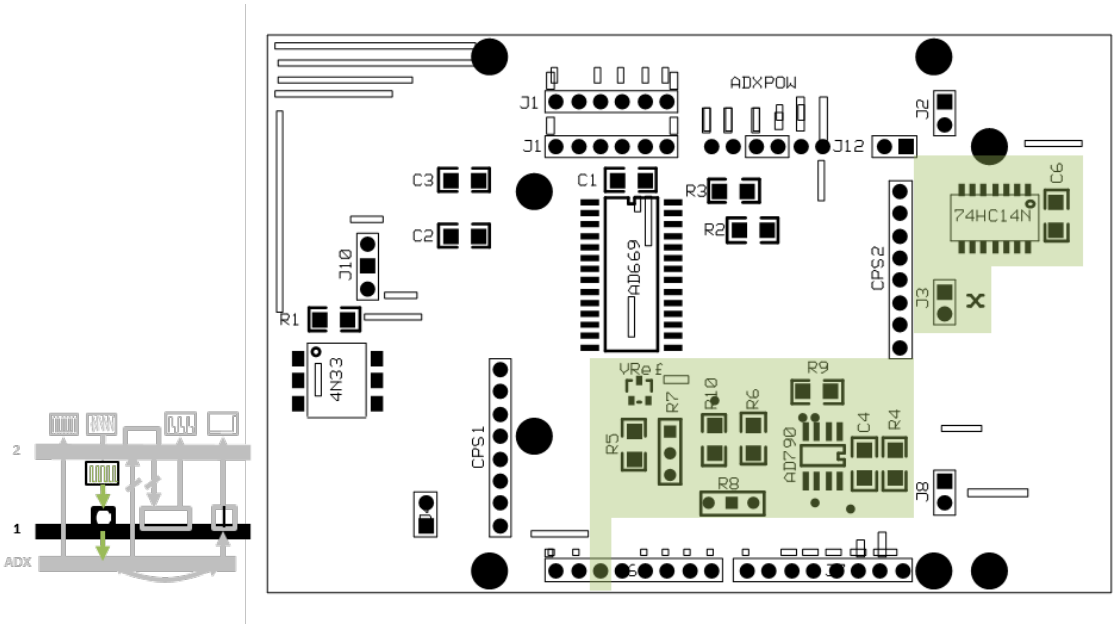

Figure 53 Comparator Block is highlighted in green

DAC Circuit

The digital-to-analog converter block, highlighted in Figure 54, includes the AD669 IC as well as all the resistors and capacitors required by specification on the datasheet. Additionally, the two 8-pin connectors CPS1 and CPS2 function to transmit the outputs from the cross-point-switch to the DAC.

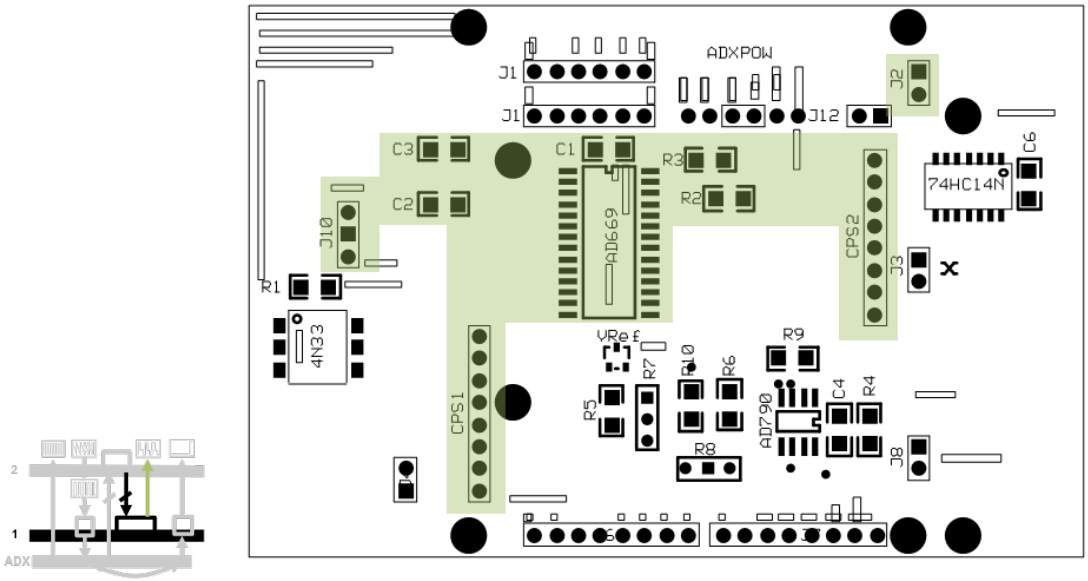

Figure 54 the DAC block is highlighted in green

Opto-Isolator

The 4N33 opto-isolator, highlighted in Figure 55, is used to control the input pins on the accommodation stimulus control electronics.

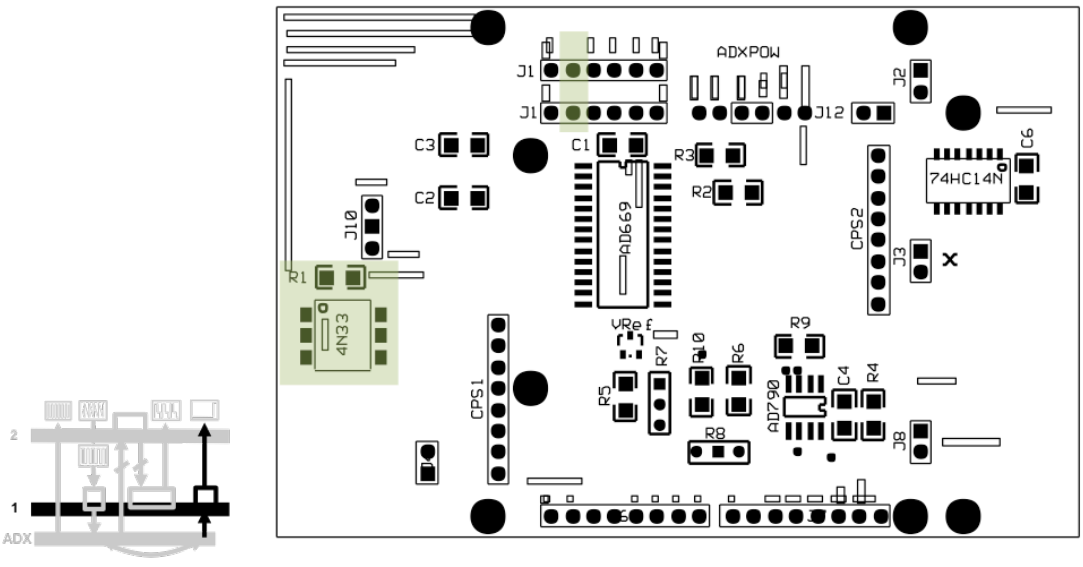

Figure 55 the Opto-isolator and associated output pins from the microcontroller are highlighted in green

PCB with traces

In Figure 56 and Figure 57, we show the top and bottom layers of the Level 1 PCB with all the traces shown.

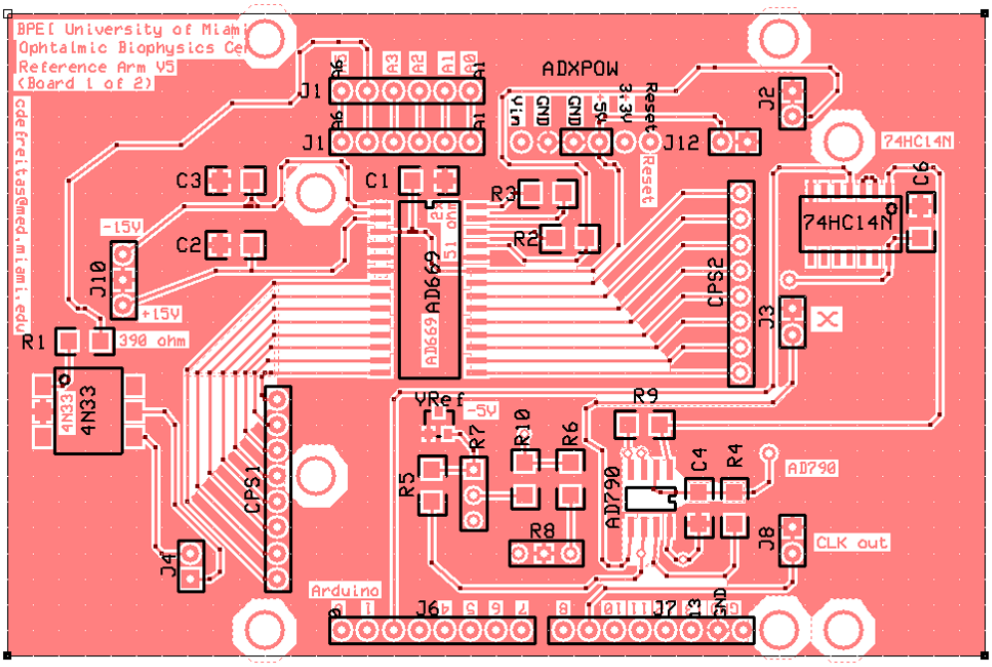

Figure 56 Top Level traces on Level 1

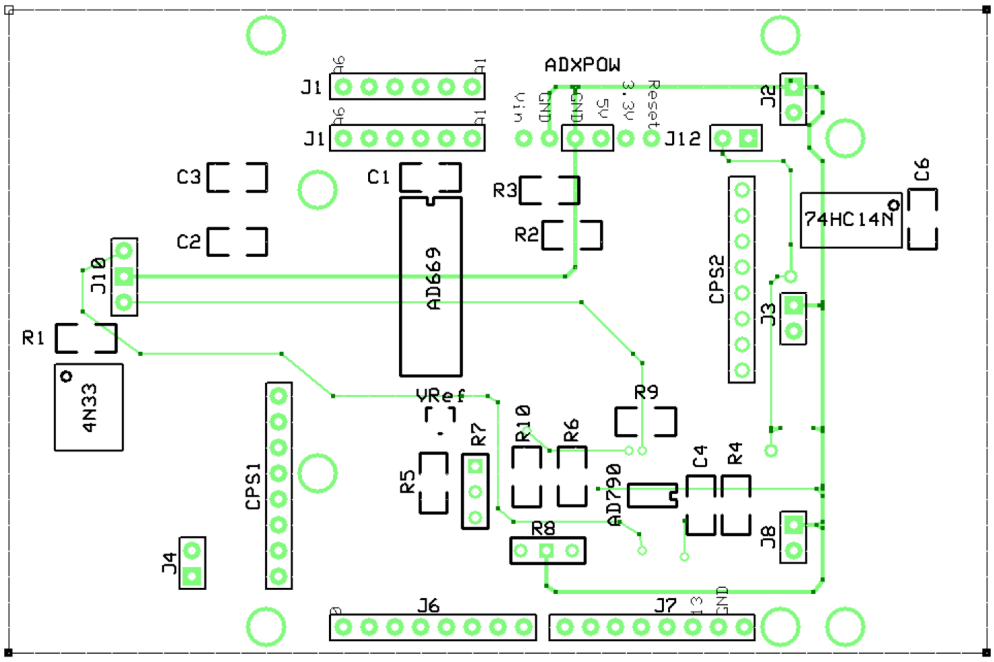

Figure 57 Bottom Layer traces on Level 1 PCB Level 1

Populated Final PCB

An image of the final assembled Level 1 PCB is shown in Figure 58.

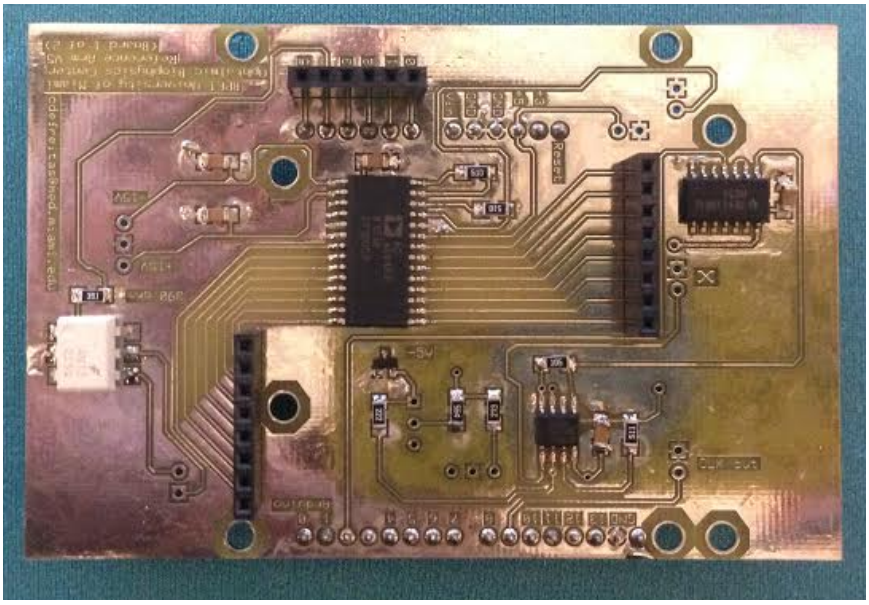

Figure 58 First level of the PCB. The integrated circuits shown correspond to (clockwise) the Comparator, the 5V voltage reference, the opto-isolator, the digital to analog converter and the hex Schmitt trigger.

4.2.2 Level 2

Placing the CPS on the top layer allows us easy access to the CPS should we need to re-program it in the future. Additionally, all of the connectors transmitting signals into or out of the control unit are placed on this top level for ease of access.

CPS Block

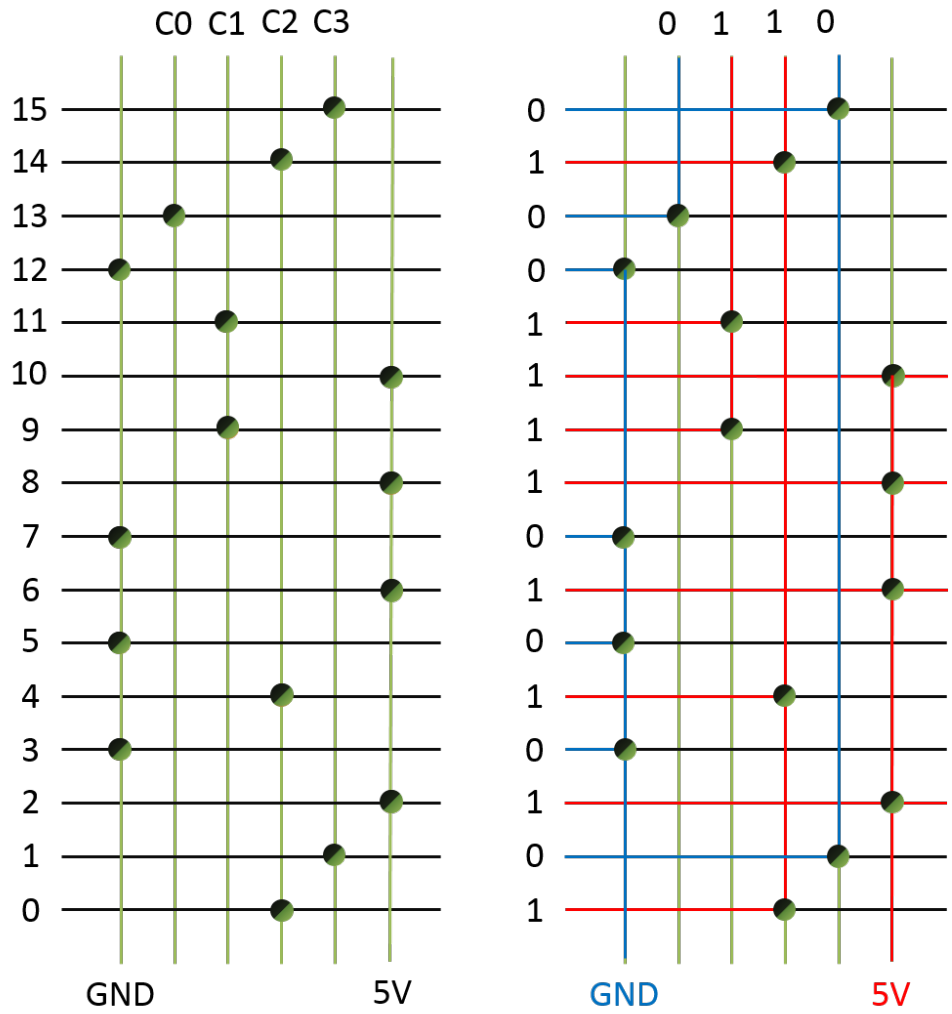

Figure 59 (Left) Cross-Point Switch implementation: vertical lines carry digital signals out from the Arduino. Horizontal lines carry digital information into the DAC. By placing a short at the intersection of the vertical and horizontal traces, a signal is physically routed from the microcontroller to the DAC. (Right) Cross-Point example for PORTC = B0110, binary 1 is shown in red and binary 0 is shown in blue.

We chose to implement the cross-point switch with a matrix of breakaway headers we can physically short with 2-pin jumpers (shunts).

The physical cross-point switch is implemented on a PCB by tracing 16 voltage traces to the input of the DAC on the top of the PCB and crossing them over 5 traces that run vertically along the bottom of the board and connect to the output of the microcontroller. Figure 59 shows, graphically, how these traces are placed, and uses circles to represent where the jumpers are placed to short two traces together. On the right side of Figure 59 an example of how the output from the microcontroller is transmitted to the DAC input through the rails is drawn.

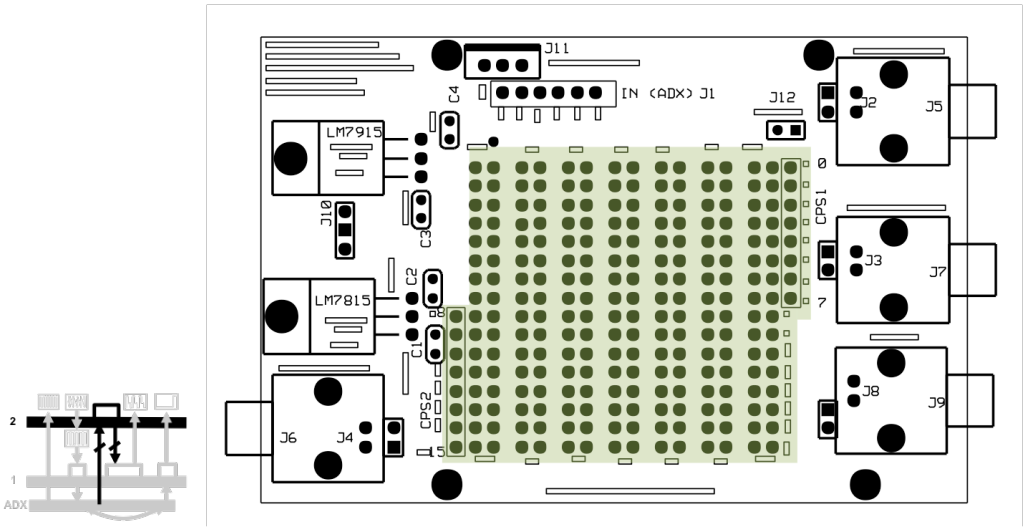

Figure 60 CPS is highlighted in green

Power Conditioning Block

As mentioned in the previous section, the DAC requires ±15V for proper operation. Two voltage regulators from Fairchild Semiconductor (LM7915 and LM7815) are placed on the top level PCB to convert existing ±24 V power to ±15V. All of the capacitors required by the datasheets are also included. Power is routed into the PCB from the control box through a 3-position, board-mounted, terminal block power connector (J11, on Figure 61). The power-conditioning block is shown in Figure 61.

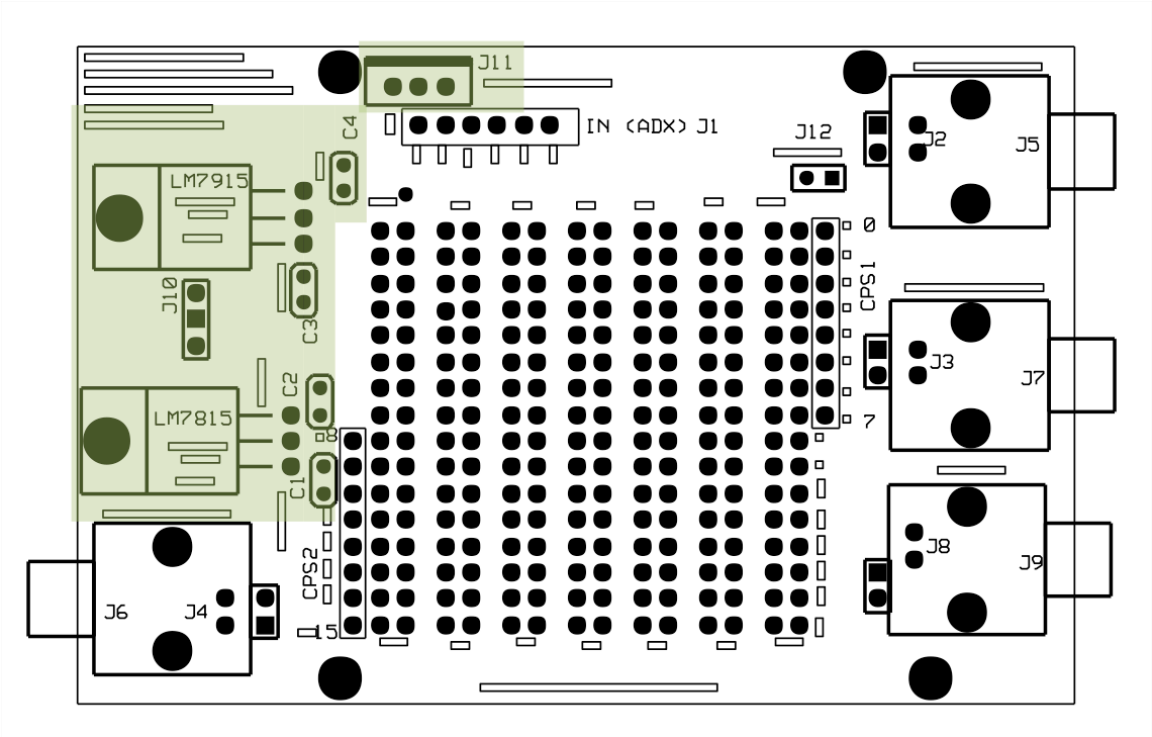

Figure 61 Power conditioning block is highlighted in green.

I/O Block

The PCB receives one analog input (X) and produces two analog outputs (Z and ACC) and one digital output (CLK). These signals are all transmitted through coaxial cables with BNC headers to their corresponding elements inside and outside of the control box. The top of the control unit is lined with 4 right angle BNC headers (Figure 62)

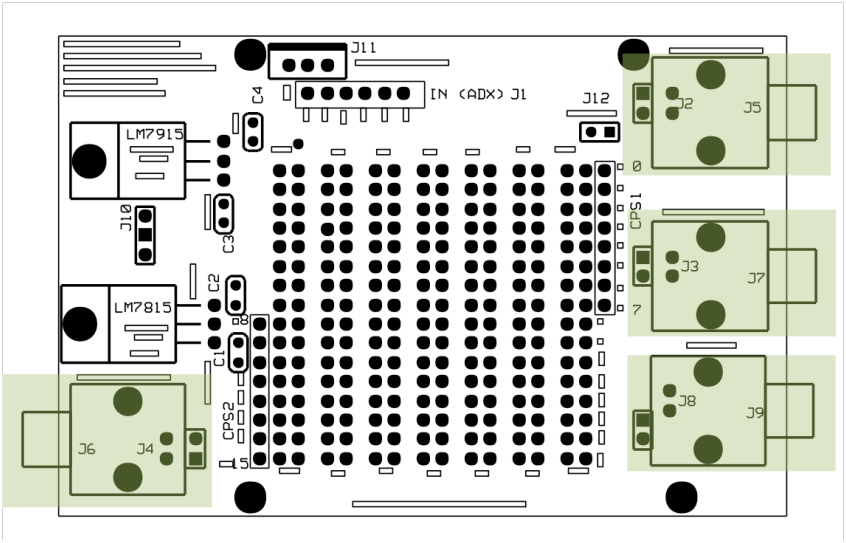

Figure 62 I/O Block is highlighted in green

PCB with Traces

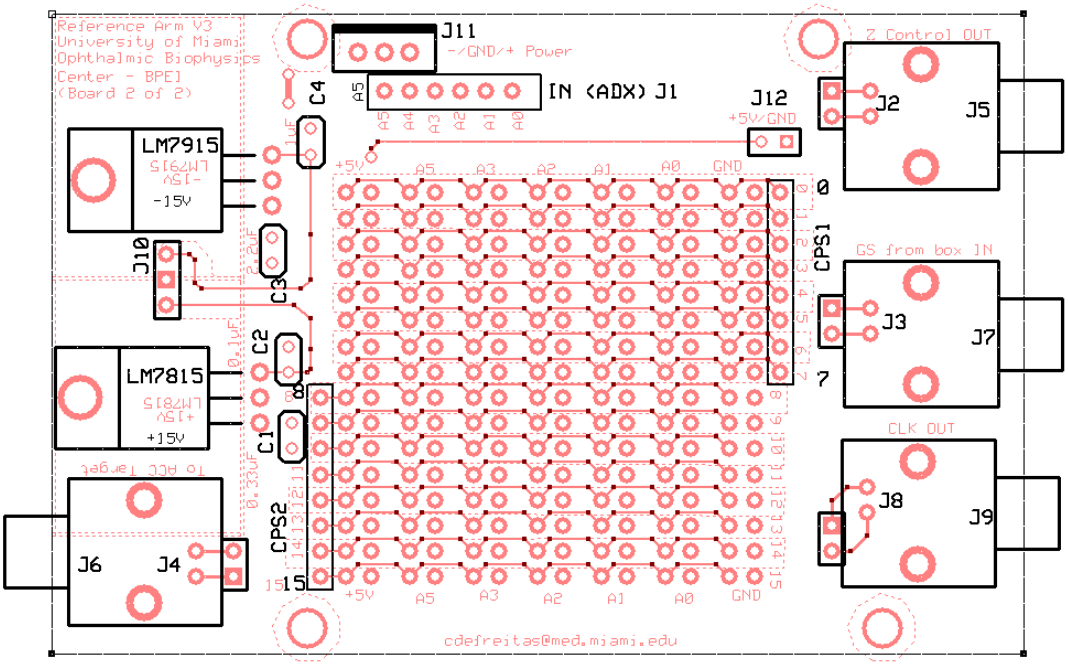

Figure 63 Top level traces on Level 2

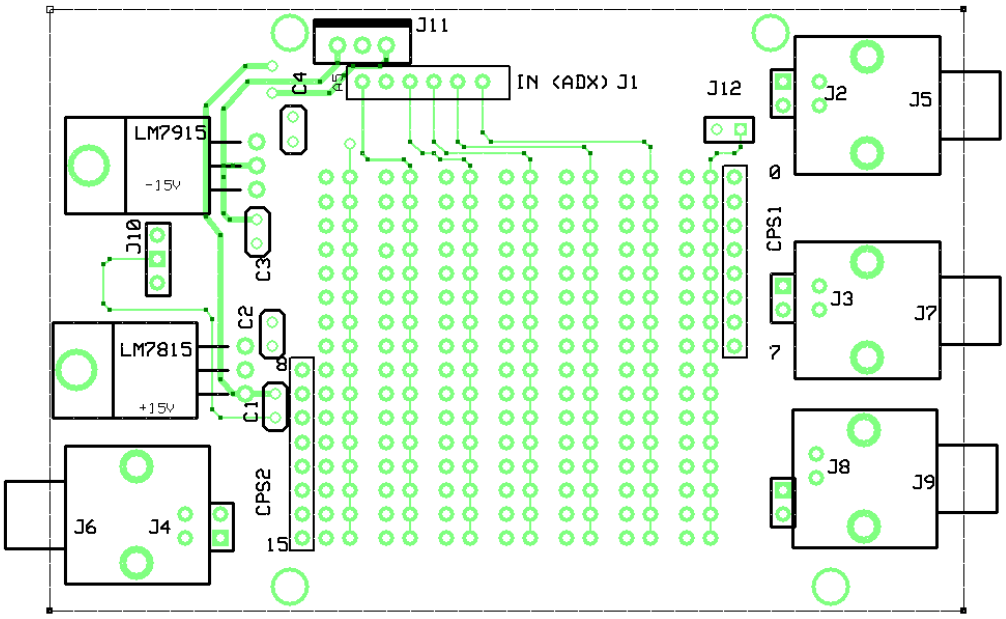

Figure 64 Bottom layer traces on Level 2

Populated Final PCB

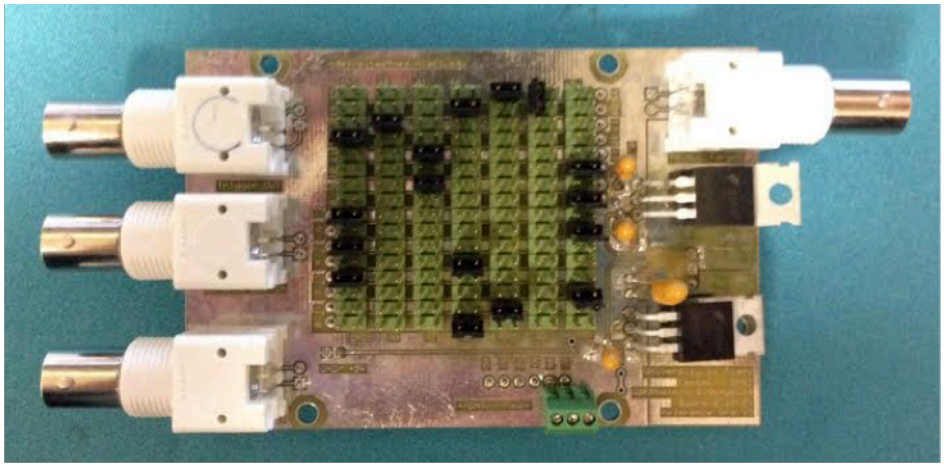

Figure 65 Top level of the PCB. The integrated components shown correspond (clockwise) to the I/O block (four BNC headers), the power block with the ±15 V Voltage regulators and associated capacitors, the 3-terminal power block, and the Cross Point Switch is in the center.

4.2.3 Assembled PCB Stack

As shown in Figure 66, the level 2 PCB stacks on top of the Level 1 PCB, which stacks onto the Arduino. The boards are all physically and electrically connected through breakaway headers.

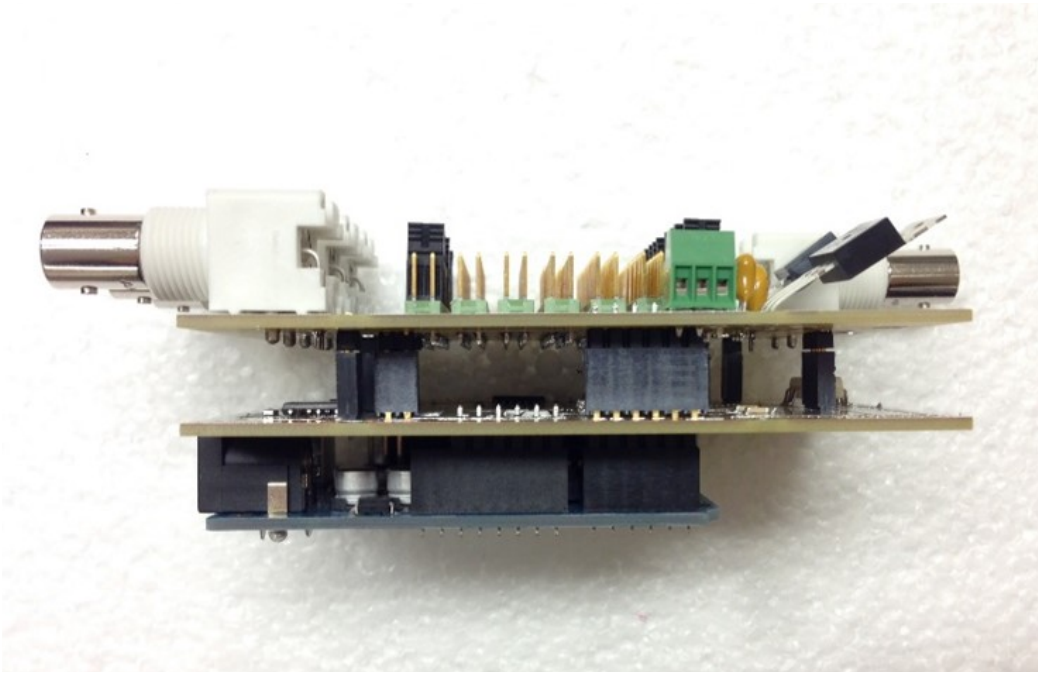

Figure 66 The three levels of the completed PCB are shown in side view. The Arduino Microcontroller is the bottom-most level. The Level 1 PCB is mounted on top of it and the Level 2 is the top-most layer.

4.3 Circuit Characterization

Major elements such as the comparator and the digital-to-analog converter went through characterization testing on the individual components to ensure the outputs were as expected.

4.3.1 Comparator Block

The first of these elements is the comparator. As previously mentioned, this assembly was necessary to generate an end-of-frame (EOF) signal from the X-galvanometer control. The EOF signal was required to alternate between TTL levels and have sharp edges.

Hysteresis of the Comparator

The comparator is used to convert the X-galvanometer signal to a digital EOF signal. In order to test if it works as expected we must make sure the threshold voltages are correct and that the hysteresis plot is as expected. Recall from section 3.3.3 and Figure 38 that we have designed the comparator for the ideal thresholds of $V_{T,\,H}$ =- 100 mV and $V_{T,\,L}$ = -200 mV, but with the resistors chosen to most closely meet the specification, we expect thresholds of $V_{T,\,H}$ =- 110 mV and $V_{T,\,L}$ = -220 mV.

By probing the X-galvanometer control signal and the output EOF signal with an oscilloscope (Tektronix TDS 2014) and plotting the recorded values against each other as in Figure 67, we find that the measured thresholds are V_{TH} =- 88 mV and V_{TL} = -224mV. While the high threshold, V_{TH} =- 88 mV, is higher than expected, it is not critical to the operation of the control unit: Recall that the high threshold is responsible for generating the falling edge of the EOF signal, which is ultimately discarded by the microcontroller. No delay is introduced due the higher threshold. The low threshold, $V_{T,\,L}$ =- 224 mV is sufficiently close to the theoretical value to allow for effective operation of the comparator block. A comparison of the theoretical, ideal and measured threshold values for both the low and high thresholds is found in Table 9.

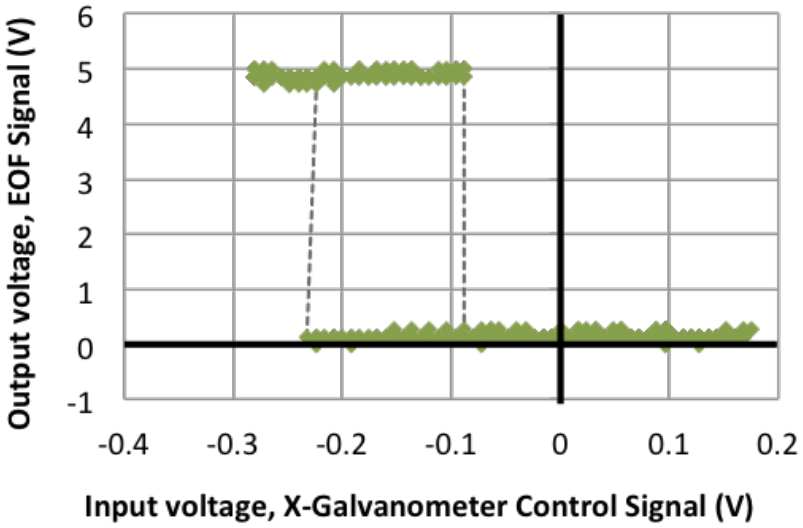

Figure 67 Characterization graph, on the X-axis is the input voltage and the Y-axis is the output of the comparator. This shows that the threshold voltages are near -224 mV and -88 mV as expected

Table 9 Summary of threshold values of the comparator. The ideal values are those that we dimensioned for. Theoretical values are those that are expected with the resistors chosen and measured values represent the values found as the threshold levels in the hysteresis plot in Figure 67.

Conditions	$V_{T,H}$	$V_{T,L}$
Ideal	-100 mV	-200 mV
Theoretical	-110 mV	-220 mV
Measured	-88 mV	-224 mV

Output waveforms

The main function of the comparator block is to produce a square wave within TTL levels of the same frequency as the input X-galvanometer control signal. To prove the efficacy of the system, we probed the input and output of the comparator block with an oscilloscope (Tektronix TDS 2104) and recorded the output to confirm the output is of the same frequency as the input (Figure 68). For a clock speed of 12.5 kHz and a 400 A-line acquisition, the EOF is shown to be synchronized with the X-galvanometer control signal, with a repeatable period of 33.6 ms.

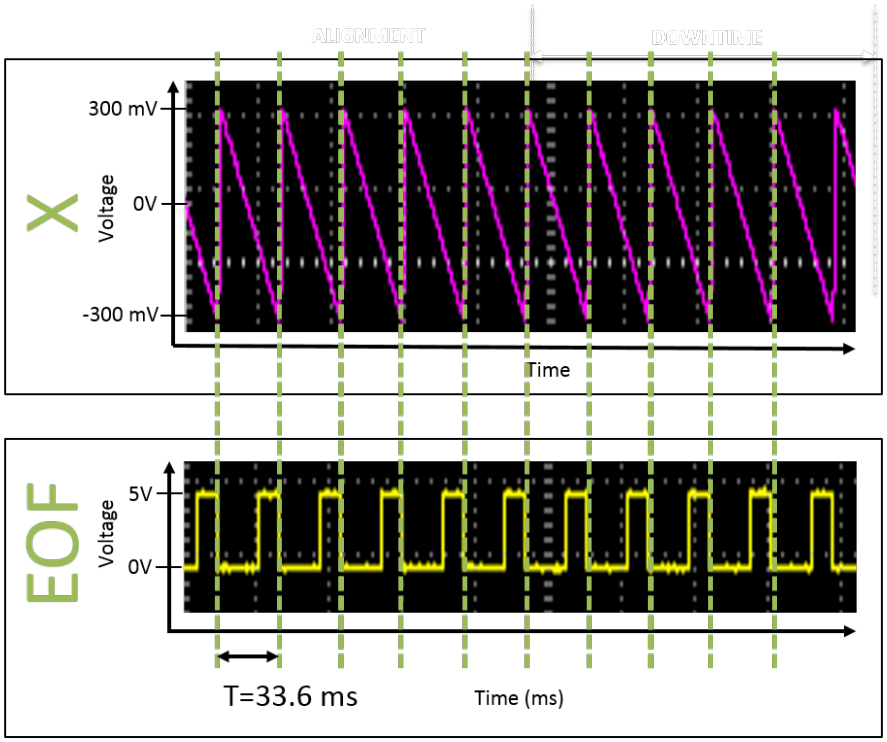

Figure 68 The waveforms of the X-galvanometer control signal input (pink) and the output of the EOF signal output (yellow)

4.3.2 Digital to Analog Converter

Output Voltages

The signals that exit DAC must correspond to the voltages the DAC was designed for. The voltages required are listed in Table 6. We measured the output of the DAC for the three inputs we provided to the DAC, given in Table 10, in binary. The output was measured with a precision voltage meter (RIGOL DM3068 Digital Multi-meter) for the binary inputs given in Table 10. The measured output voltages are sufficiently within the tolerances given in Table 6, except for the M2. However, the 4.3455 V measurement is still within the tolerances to obtain a 90% power coupling efficiency from the mirror. Since, in practice, this frame collects the least amount of structural information and

detail, as it corresponds to a very small slice of the retina, we can afford the slight decrease in optical power returned for this image.

Table 10 Measured output of the DAC for the given 16-bit Input

Reference Mirror/Area of interest	PORTC Output	16-Bit input to DAC	Theoretical Voltage (V)	Switching Output Voltage from DAC (V)
Cornea (M3)	B0100	1000010101000110	5.2050 V	5.2020 v
Retina (M2)	B0111	0110111101010101	4.3489 V	4.3455 V
Lens (M1)	B0011	0100111101010100	3.0988 V	3.0970 V

Voltage Stability Measurements

The stability of the voltages output from the DAC is critical for reliable functionality of the switch: if the galvanometer-mounted mirror were to move significantly during imaging, a power loss would be evident in the final frame. There is an inherent warm-up time with the electronics. To this end, we measured, using a precision multi-meter (RIGOL DM3068 Digital Multi-meter) the initial voltage response for one output position from system off over the first 13 minutes; Figure 69. During the warm-up time, the voltage was well within the tolerances set in Table 6 for voltages that would provide a 95% coupling efficiency or greater. Recall, for this particular mirror, we require a stable output voltage between 5.1986 V and 5.207V for a 95% coupling efficiency and the entirety of our measurement is well within those bounds.

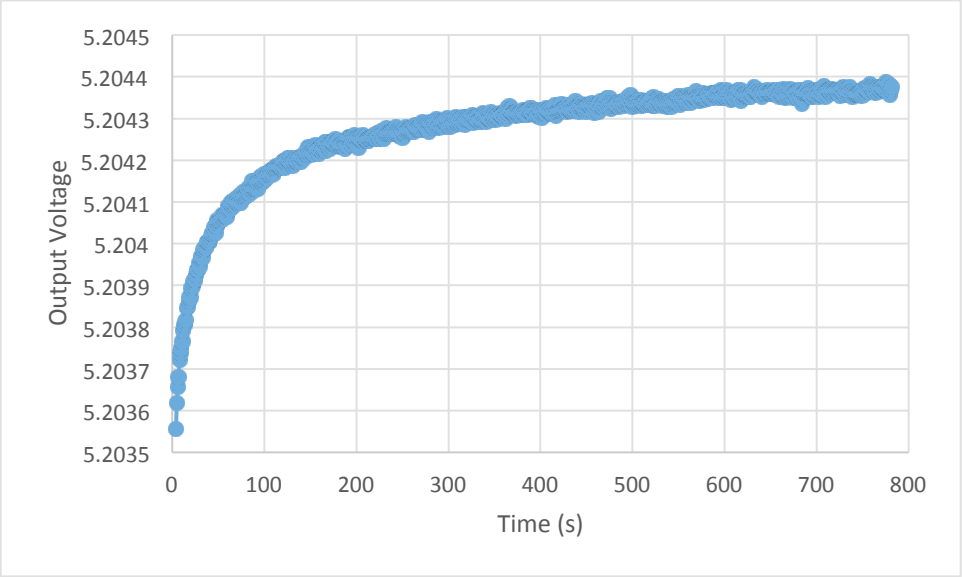

Figure 69 Initial voltage response of the system showing a settling time of about 300 seconds to reach within 2% of the final value of 5.2044 V.

4.3.3 Timing Analysis

It is imperative that the circuit responds within the fly-back time of the X-galvanometer mirror. We use an oscilloscope to probe the X-galvanometer control signal as the input and the EOF and Z-galvanometer control signal as the output. The waveforms are recorded over 5 ms simultaneously during a switching event. These waveforms are shown in Figure 70. From these recorded data, we can measure the total propagation delay within the system. Recall that the fly-back time is 1.6 ms.

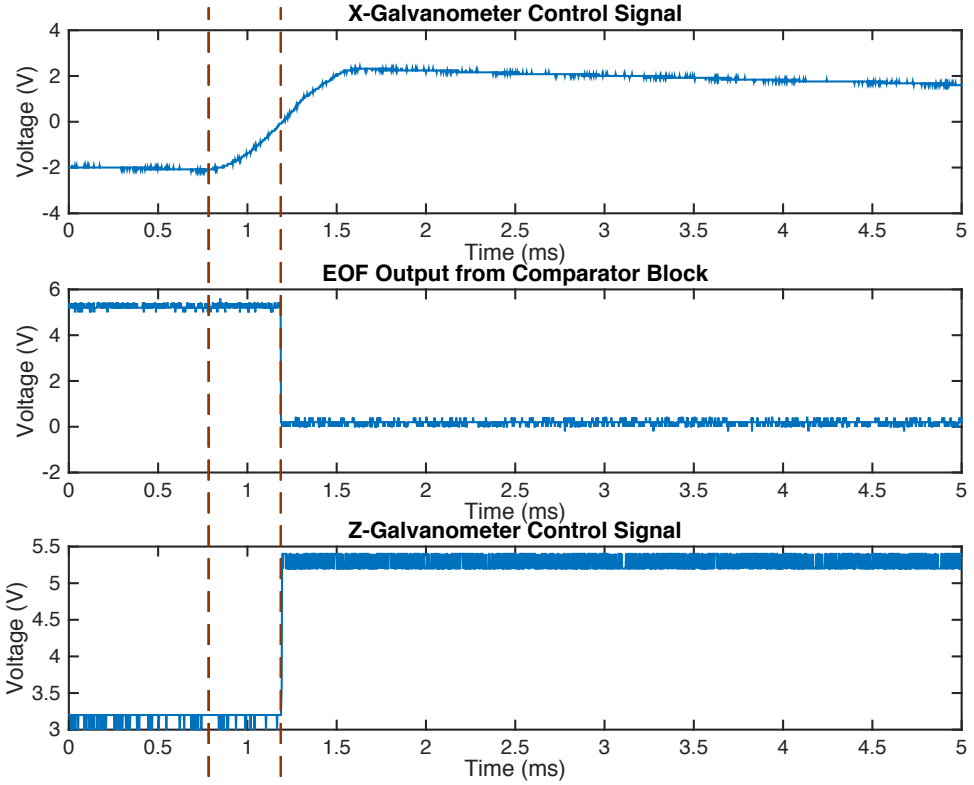

Figure 70 The recorded waveforms. The vertical red lines are at t = 0.786 ms and t = 1.187 ms and represent the beginning of fly-back time, and the EOF switching event time, respectively.

Using the time scale presented in the waveform graphs in Figure 70, the X-galvanometer control signal voltage begins rising, signaling the beginning of fly-back time, at approximately t = 0.768 ms. The EOF signal switches from 0 to 5V after 0.419 ms have elapsed, at 1.187 ms. The final Z-Galvanometer control signal switches from 3.097 V (M1) to 5.202 V (M3) after 0.006 ms, at 1.193 ms. The propagation delays are summarized in Table 11 and all sum to a total delay of d_{delay}= 0.425 ms.

Table 11 Propagation delays in the electronic

Delays	Time of switch	delay
$t_{(x)delay-x-EOF}$	0.786 ms	
$t_{(EOF)}$	1.186 ms	0.419 ms
$t_{(z)}$	1.193 ms	0.006 ms
$\sum t_{delay}$		0.425 ms

We present this measurement on one switching event: the delay is identical for all three events.

The response time of the electronics is measured, but the galvanometer actuator introduces a delay that depends on the scanning geometry. To account for this delay, we measure the optical power returned into the interferometer after a switching event. In order to measure the power returned into the interferometer from the reference arm, we replace the spectrometer with a photodiode (Optiphase, V-600 Tunable Optical Converter) connected directly to the interferometer, as shown in Figure 71. The photodiode translates optical power to voltage; this signal can then be probed with an oscilloscope and the transient optical power can be measured as the mirror is changing position. This is an indicator of how long it takes for the optical switch mirror to physically scan the light beam from one reference mirror to the next. Once the beam has settled its final location, optical power returned will also settle to a final resting value.

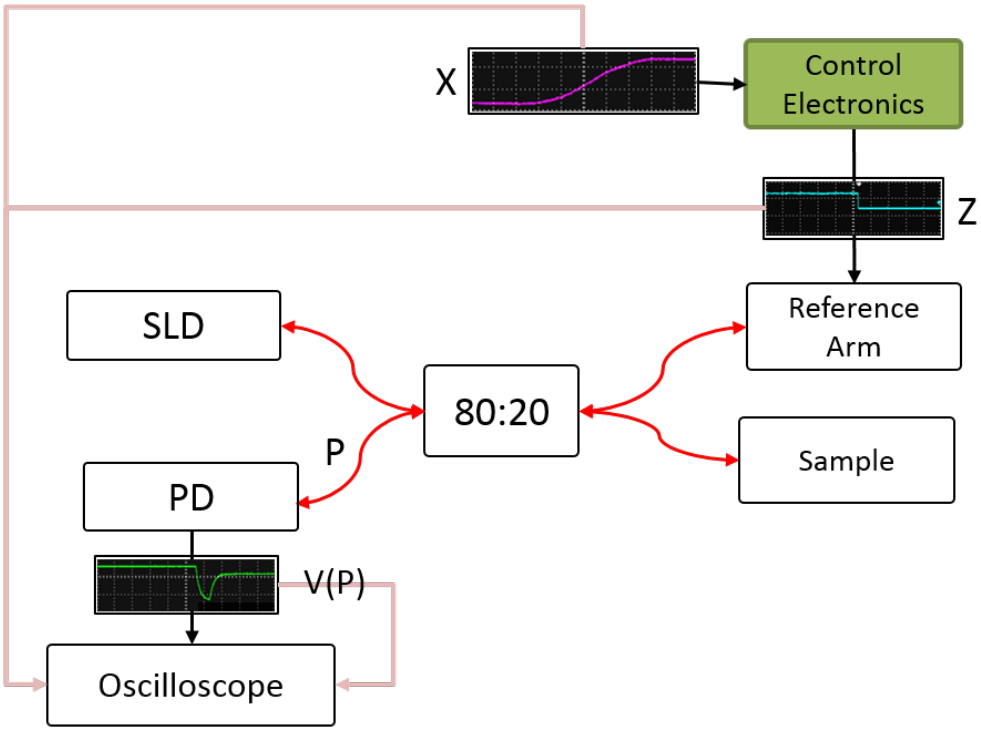

Figure 71 Schematic of the experiment used to measure the delay introduced by the physical movement of the Z-galvanometer-mounted mirror in the optical switch. The spectrometer was replaced with a photodiode that converts the optical power (P) to a voltage (V(P)).

The transient relative optical power returned for each switching event is shown in Figure 72, Figure 73 and Figure 74 as well as X-galvanometer control signal and the Z-galvanometer control signal for that switching event.

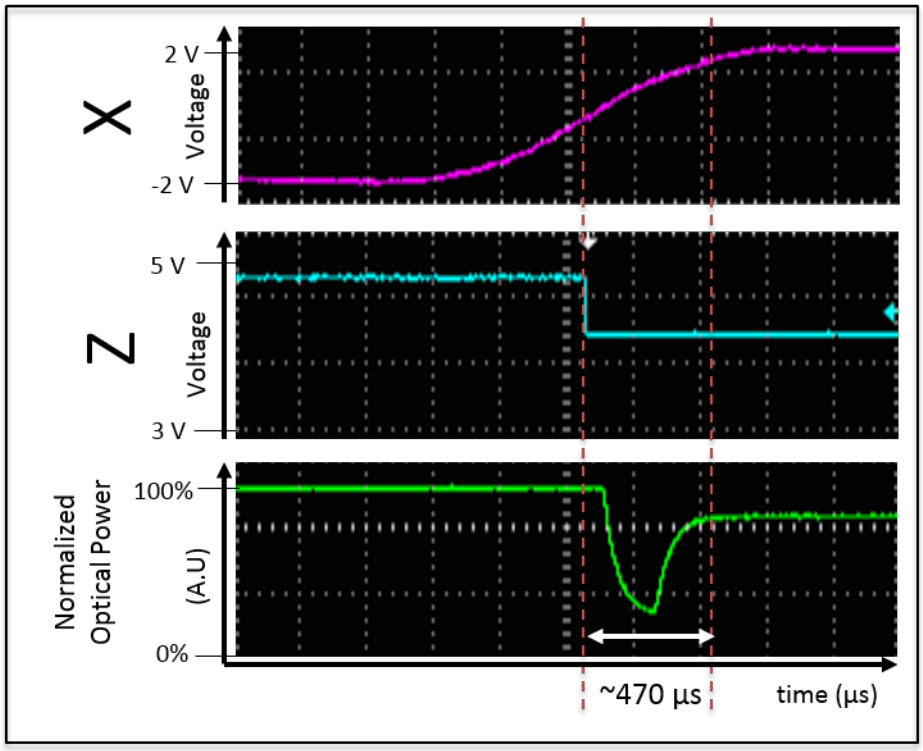

Figure 72 The X-galvanometer control signal, the Z-galvanometer control signal and the normalized relative transient returned optical power from when the optical scanning mirror switches from M3 (Cornea) to M2 (Retina). The measured delay of the mirror moving is 0.47 ms.

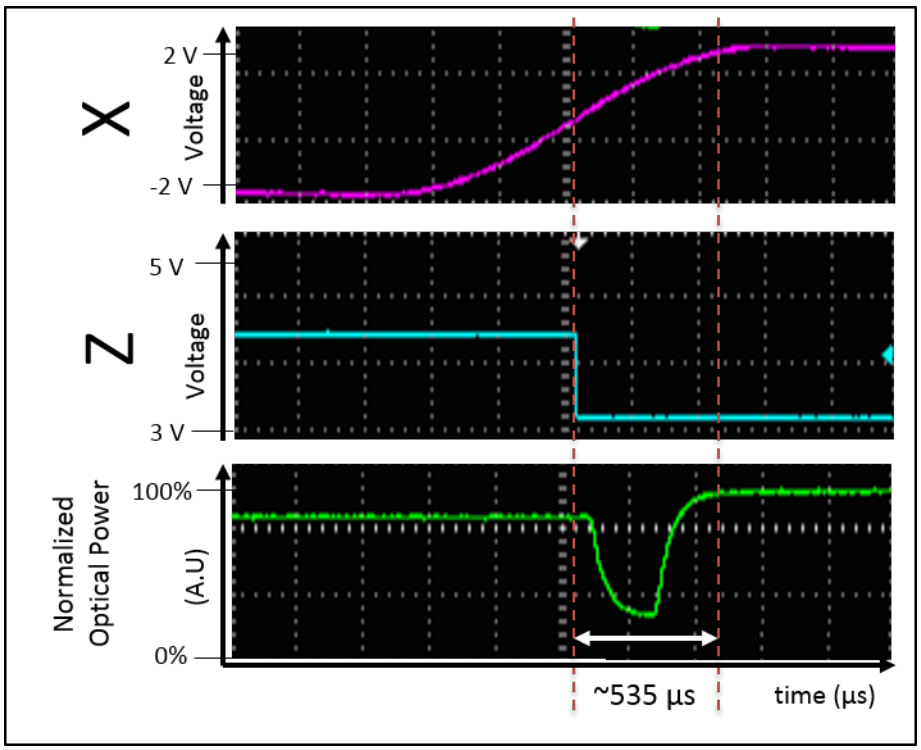

Figure 73 The X-galvanometer control signal, the Z-galvanometer control signal and the normalized relative transient returned optical power from when the optical scanning mirror switches from M2 (Retina) to M1 (Lens). The measured delay of the mirror moving is 0.535 ms.

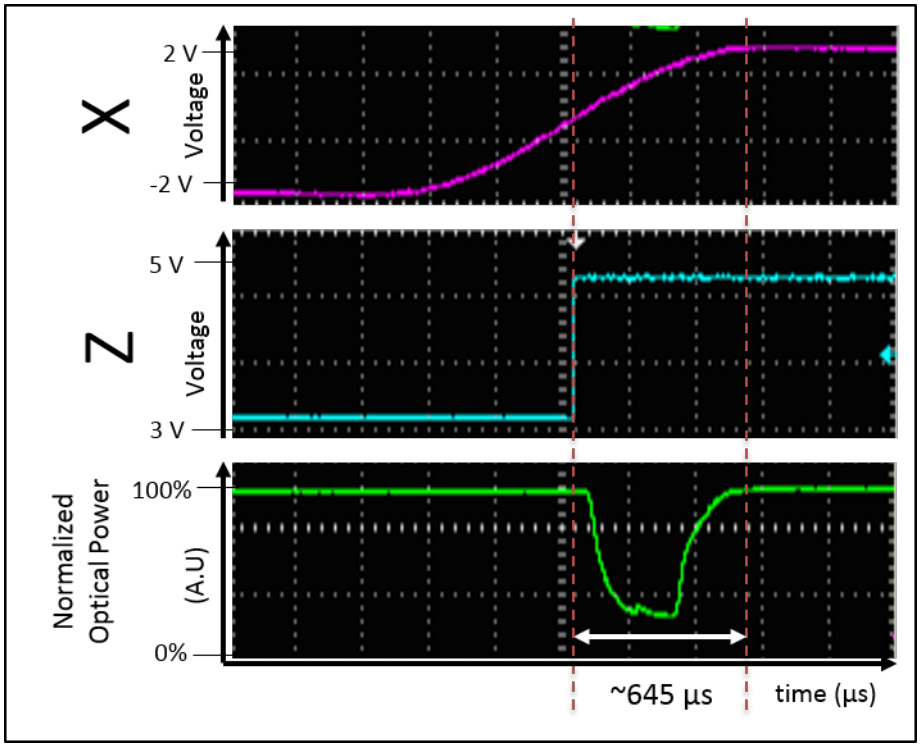

Figure 74 The X-galvanometer control signal, the Z-galvanometer control signal and the normalized relative transient returned optical power from when the optical scanning mirror switches from M1 (Lens) to M3 (Cornea). The measured delay of the mirror moving is 0.647 ms.

Summing the measured delays for the mirror moving and the previously mentioned delays due to the propagation results in a maximum delay time of the entire mirror switching process. The total delays for each switching event are summarized in Table 12. The largest total delay measured is 1.07 ms, which is still within the 1.6 ms constraint measured in Section 3.1.1.

Table 12 Propagation delays

Delays	M1-M3	M3-M2	M2-M1
$t_{d-electronics}$	0.425 ms	0.425 ms	0.425 ms
$t_{d-mirrormove}$	0.645 ms	0.470 ms	0.535 ms
$\sum t_{delay}$	1.07 ms	0.895 ms	0.96 ms

Additionally, if we probe the signals for a longer amount of time, we can see that the synchronization of the output signal remains synchronized with the X-galvanometer control signal. This is shown in Figure 76.

Using the same method described above, we can also measure the optical power coupled back into the interferometer as the mirror switches for several switching events.

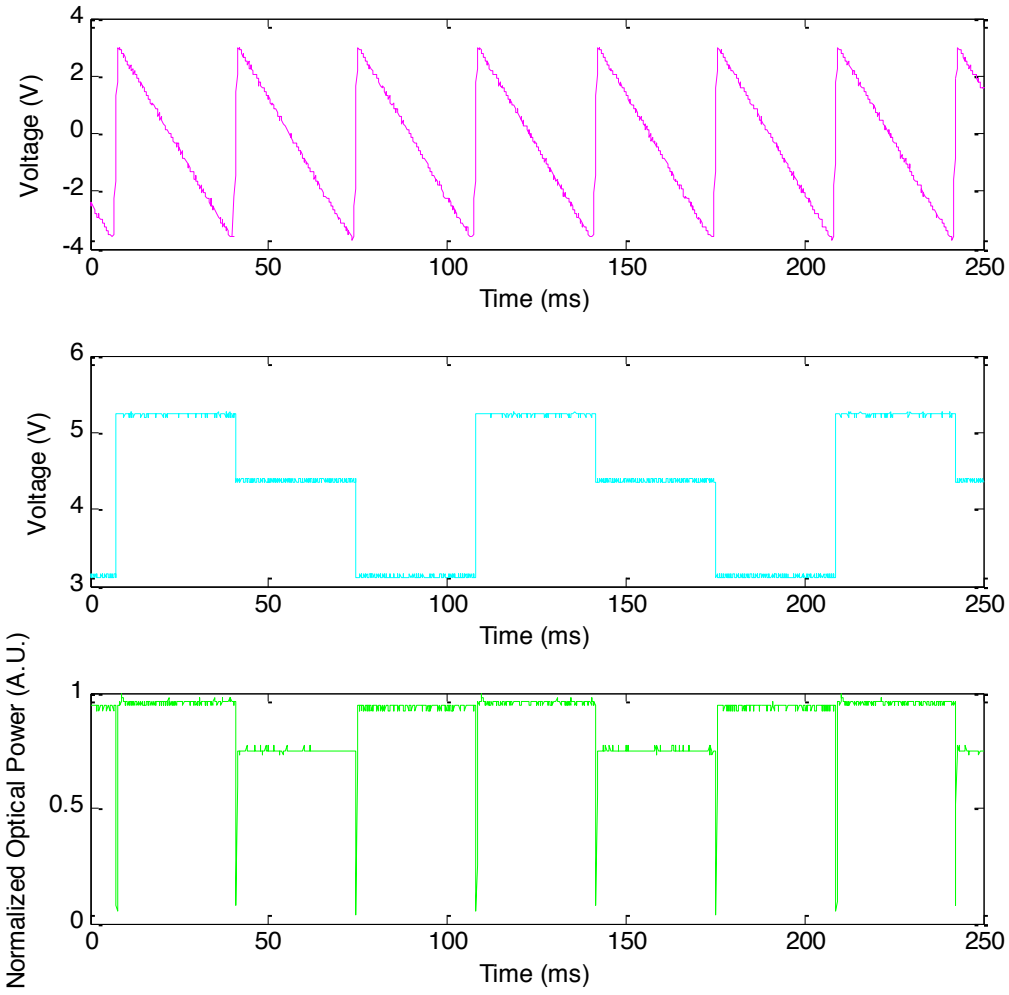

Figure 75 (Top) X-Galvanometer control signal. (Middle) Z-galvanometer control signal (Bottom) Normalized optical power measured over several frames.

As expected, Figure 72, Figure 73 and Figure 75 indicate that the power returned from the mirror M2 (Retina) is slightly lower than the relative power returned from mirrors M1 and M3. The M2 mirror is associated with the reference mirror that allows the system to image the retina. The normalized returned power on this mirror is approximately 0.75.

4.3.4 Accommodation Target Characterization

In order to quantify the delay in the system for switching the accommodation stimulus, we acquired the waveforms shown in Figure 76 from the oscilloscope. The top waveform (green) is the output from the X-galvanometer control board. The yellow square wave is the EOF output from the comparator, the blue signal is the output from the DAC, and the pink is the input voltage to the accommodation target, set to switch after acquiring 10 B-scans, or 5 frames, in this example. The waveforms shown correspond to a scanning routine that only switches between two mirrors instead of three; this is used for imaging only the anterior segment. The waveforms of Figure 76 correspond to the first 6 frames acquired in an acquisition routine, which is marked as beginning at Time = 0 ms. From Figure 76, we can see that the voltage applied to the retro-illumination of the far target on the accommodation stimulus goes high towards the beginning of the acquisition of the sixth frame. The sixth frame begins at Time = 168 ms, and approximately 18 ms later, the accommodation stimulus is switched, indicated by the pink vertical line.

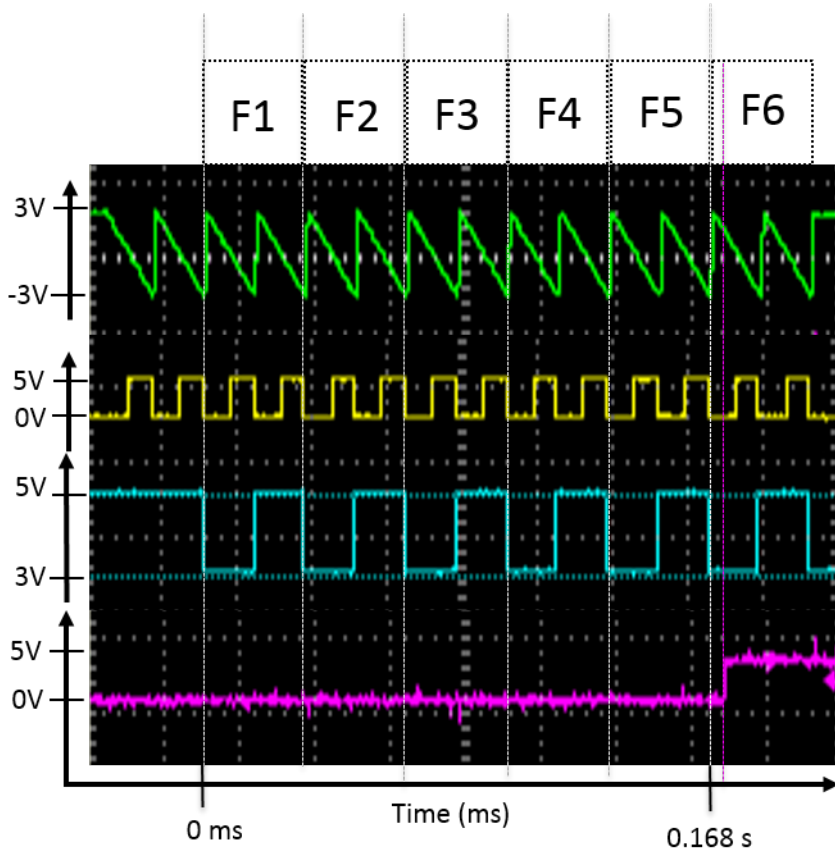

Figure 76 Blue is the output of the Z-galvanometer from the top of the Arduino. Green is the output of the X-galvanometer from the box. The pink is the power input into one accommodation target and yellow is the filter X-galvanometer signal that is input to the Arduino and serves as the interrupt trigger.

Chapter 5

Application and Measurements

In the following section a brief summary of the extended depth images that can be acquired using the implemented optical switch, as well as some preliminary dynamic measurements of the anterior segment as the eye responds to an accommodation stimulus change is presented.

5.1 Whole Eye Images and Length Measurements

Figure 77 Single cross-sectional image spanning the length of the eye. The non-imaged vitreous is shown in black.

Ultimately, we would like to accomplish the acquisition of three consecutive frames spanning the cornea, anterior chamber, crystalline lens and then the retina. We can recombine these images into a single cohesive frame with custom in-house software. The final composite image, an example is shown in Figure 77, includes the anterior segment imaged with high sensitivity throughout.

From a single composite acquisition, we can extract biometric data regarding the distance along the central A-line of the eye between several biological structures including: corneal thickness, anterior chamber depth, crystalline lens thickness and the depth of the vitreous.

The ability to acquire several composite frames sequentially allows our team to investigate the effects of a change in accommodative stimulus on the length of the eye.

We can understand how the biometry of each element is changing directly with the stimulus.

5.2 Real-Time Accommodation Dynamics Measurements

In order to demonstrate the system can acquire whole eye images and make real-time accommodation dynamics measurements, 3 emmetropic subjects, ages 20, 21 and 26 were imaged using the system following an IRB approved Human Research Subject Protocol (IRB # 20121041). The patient was asked to sit in front of the delivery optics and rest their head on a chin rest to ensure the subject remained stable during imaging. The accommodation unit integrated in the OCT delivery path provided monocular accommodative step stimuli stepping between 0D to 2D for the first acquisition and between 0D and 4D for the second. The subject was asked to maintain their focus on the retro-illuminated target in the accommodation stimulus unit. Each B-scan consisted of 400 A-lines acquired at a rate of almost 15 frames/second and spanned 8 mm across. In both cases, the accommodative stimulus was changed after imaging 25 frames. A total of 80 composite images (“frames”) of the full-length anterior segment were consecutively acquired during an accommodative response for a total time of 5.376 ms. The accommodative response was measured twice for each subject: once for each accommodative stimulus change. Once the images are acquired they are processed through custom-developed stitching and segmentation software that measures the optical distances for the thickness of the cornea, depth of the anterior chamber and thickness of the crystalline lens along the central axis of the image. Each of these thicknesses is converted into true geometrical distance by dividing by the refractive index of each

element [32, 33] and those distances can be plotted over time to show quantitative evidence of how the dynamics of the anterior chamber change with response to accommodation.

In Figure 78 we show the results of a 21-year-old test subject responding to both 2D and 4D of step-change in accommodation stimulus. In Figure 79, we present the images associated with t=0 (the unaccommodated, resting state) and t=2.5 s, the fully accommodated state.

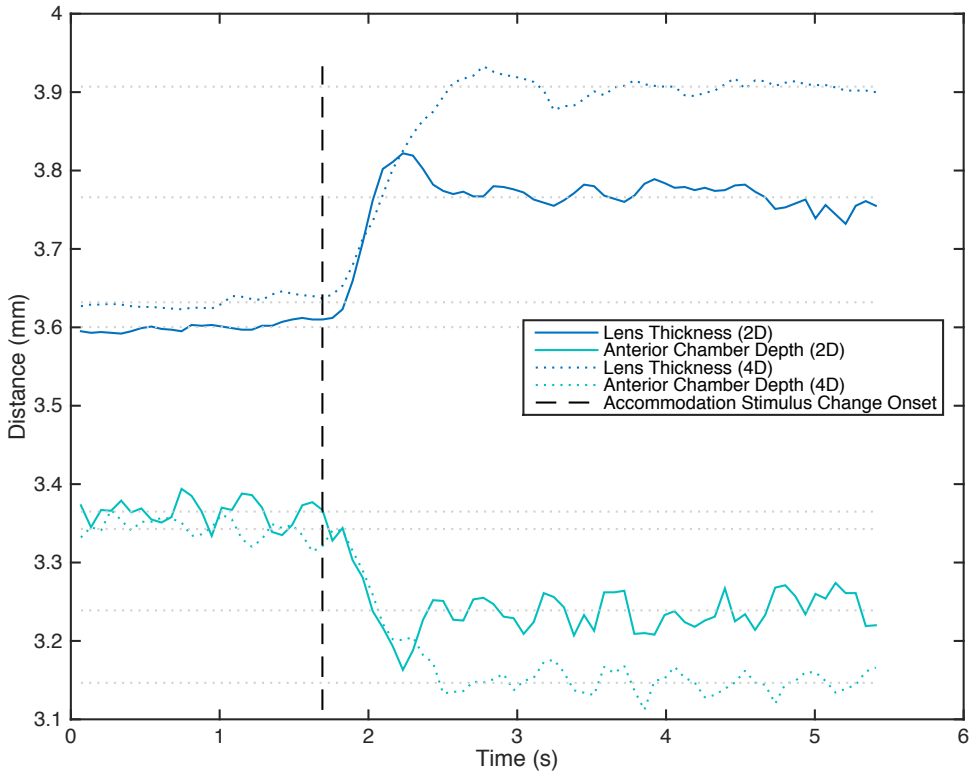

Figure 78 shows the dynamic accommodative response of a 20 year old male subject over 5 seconds where the vertical black dotted line shows when the accommodation stimulus change was applied. All distances are measured along the central optical axis.

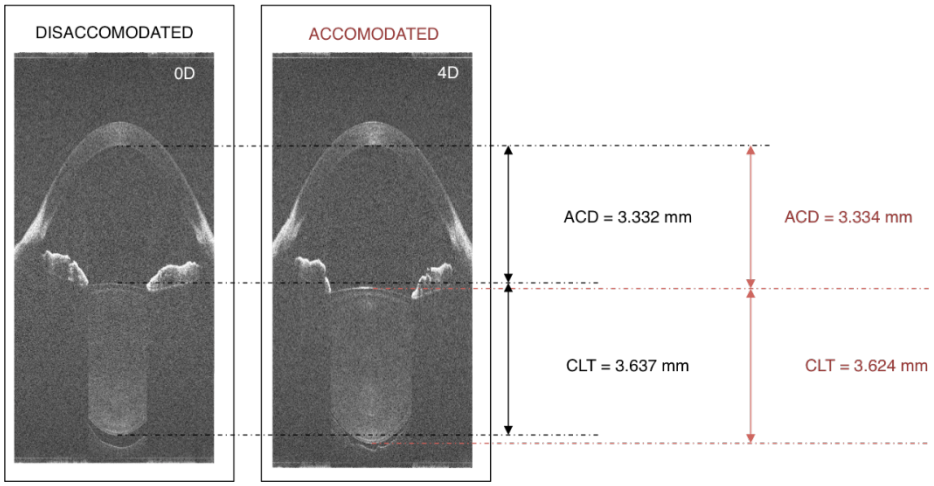

Figure 79 Snapshots of the acquisition at t = 0 and t = 2.5 seconds (after the accommodation stimulus has been applied). The dimensions for the Anterior Chamber Depth (ACD) and Crystalline Lens Thickness (CLT), before and after, are shown.

For each subject we can measure average crystalline lens thickness for the relaxed and accommodative states as well as how much time elapsed between the onset of accommodation stimulus change and reaching the stable accommodated state. We present the dynamic histories of the change in biometry of the anterior segment for two more subjects in Figure 80 and Figure 81.

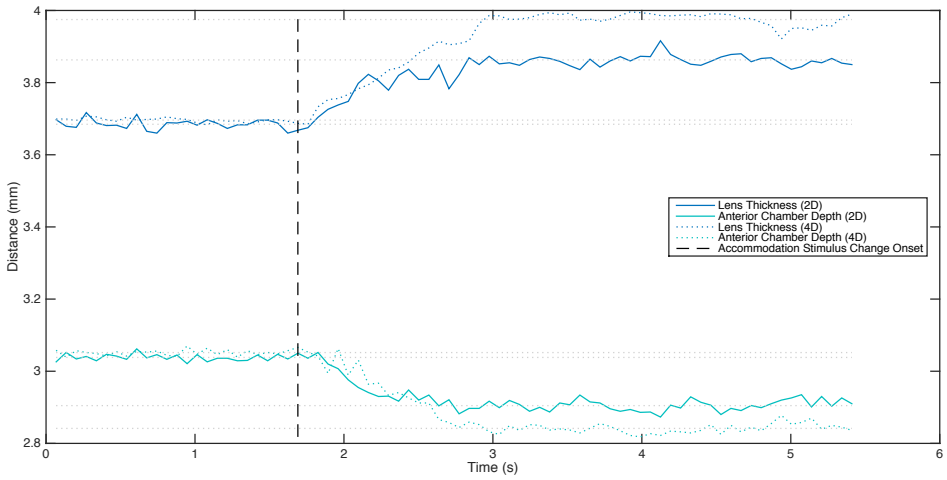

Figure 80 22 year old Female, responding to 2D and 4D accommodation stimulus change

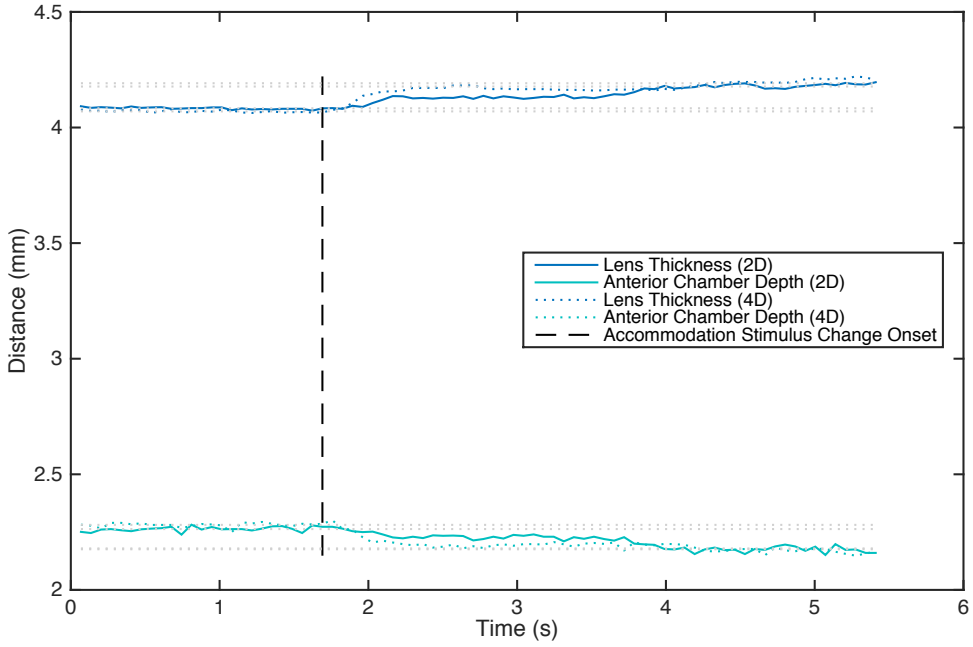

Figure 81 24 year old Female, responding to 2D and 4D accommodation stimulus change

From the plots shown in Figure 78**,** Figure 80 and Figure 81 we can extract measurements on the dynamic response of the eye to a change in accommodative stimulus. We can quantify the thickness change in the crystalline lens as well as the change in anterior chamber depth. Additionally, having multiple successive frames allows us to determine the settling time of the accommodative response.

From these dynamic measurements, we can also measure the amount of time it takes the eye to reach an accommodated state, or the settling time. We use the average of the final 20 measurements of the intraocular distances as the accommodated dimensions and can then determine how long it takes, from the onset of the accommodation stimulus change, to reach that settled value. In Table 13, we include a summary of the thickness changes and settling times for the three subjects corresponding to Figure 78**,** Figure 80 and Figure 81.

Table 13 Summary of the dynamic measurement results. We can quantify changes in depth with accommodation as well as time elapsed to reach an accommodative state after stimulus.

Subject	Accommodation Stimulus	Change in Anterior Chamber Depth (mm)	Change in Crystalline Lens Thickness (mm)	Settling time (ms)
21 M	2D	-0.12	0.17	338
	4D	-0.19	0.28	879
22 F	2D	-0.13	0.18	946
	4D	-0.21	0.28	1,217
24 F	2D	-0.08	0.09	2,231
	4D	-0.11	0.12	879

5.3 Conclusions

These experiments show that with the integration of the optical switch we can perform a variety of quantitative measurements on the dynamics of the accommodative response of the eye. We have the ability to record and quantify the dynamics of the anterior segment and the retina as the subject responds to a change in accommodative stimulus. We can measure changes in depths of the anterior and vitreous chamber as well as changes in thickness of the crystalline lens. We can also quantify how long it takes the eye to reach a stable accommodated state.

Chapter 6

Summary and Future Work

We have developed an electronic control unit that can successfully dictate a switching routine for an existing optical switch in a custom-built SD-OCT device. The control unit is responsible for synchronizing different elements of the OCT device, including a custom-built delay-line optical switch and a custom-built accommodation stimulus unit.

The Control Unit successfully integrates with the commercial SD-OCT software, InVivoVue (Bioptigen, NC), to record successive images at different imaging depths. From a single signal generated through the software to control the X-galvanometer transversal scanning mirror position, the control unit can determine if the SD-OCT system is in Acquisition mode or Alignment mode and generate a square wave of alternating voltage values to dictate the position of the optical switch's galvanometer-mounted mirror as well as a signal to trigger an accommodative stimulus change.

The control unit is sufficiently flexible through the application of several software routines, allowing several parameters to be changed with software including: the number of delay lines employed during scanning, the timing of the accommodation stimulus change and the camera's acquisition speed.

We have demonstrated that for the acquisition speed of interest, the control unit can switch the position of the optical switch mirror within the fly-back time and can repeatedly output the precise voltages required for the galvanometer-mounted mirror position control.

With this system in place, we can dynamically image the accommodative response with sufficient depth to cover the entire anterior segment and extrapolate dynamic biometric measurements from those images. Additionally, we can image the retina as a third successive frame, allowing for axial eye length measurements with the SD-OCT system.

We have demonstrated that we can effectively quantify the axial biometric changes during accommodation of the anterior chamber for young subjects. We can image these subjects for sufficiently long to gather information on both the relaxed and accommodative states of the eye during one imaging session.

6.1 Future Work

Future comprehensive randomized clinical studies on a larger set of subjects are necessary to truly understand the dynamics of the anterior segment during accommodation. In order to facilitate these studies, a graphical user interface (GUI) is required to act as a front-end for the software that controls to digital electronics used in the system. This would allow technicians to more easily adjust the parameters of the scan and the accommodation stimulus.

Additionally, it would be beneficial space-wise to integrate the electronics that control the accommodation unit into the same physical PCB that is used for the galvanometer control – simplifying the entire device and minimizing the number of cables routes through the control box.

Currently the software provided for the galvanometer control electronics only allows for successive linear B-scans. In the future, it could be beneficial to adjust the

output scanning Z patterns so that they can allow for volumetric, radial and cylindrical scans of the anterior segment as well.

The optical switching method presented in this document lends itself well to the implementation of even more delay lines into the SD-OCT. In future iterations, it is possible to acquire more than 3 frames across the length of the eye through the implementation of more radially distributed reference arm mirrors. These extra reference arm mirrors were not implemented into the initial iteration of the optical switch because they provide no structural information at a high time cost.

In future iterations, it would be beneficial to omit the cross-point switch and instead output 16-bits of position data directly from the TPU itself. This would reduce complexity in the control unit electronics without adding a substantial delay. We have found the combined delay introduced by the TPU, the CPS and the DAC amount to 0.006 ms, or less than 1% of the fly-back time of the X-galvanometer mirror. We thus determine the delay introduced by outputting more information from the TPU should not affect the overall switching time significantly. Outputting the 16-bit Z-galvanometer position directly from the microcontroller allows for more flexibility in reference mirror position, and easier re-calibrating should the system require adjustment.

6.2 Conclusions

The above document shows that successful development and implementation of control electronics for the integration of an existing optical switch with a commercial SD-OCT system. This system can now acquire several images across the axial range of the eye in rapid succession to determine accommodative amplitude in normal subjects and also those implanted with devices designed to restore accommodation in presbyopia.

Works Cited

1. A. P. A. Beers G.L. van der Heijde. Age-related changes in the accommodation mechanism. Optometry and Vision Science 1996;16:216-221.

2. A. P. A. Beers G.L. van der Heijde. In vivo determination of the biomechanical properties of the component elements of the accommodation mechanism. Vision Research 1994;34:2897-2905.

3. M. Ruggeri. S. Ulhorn C de Freitas, A. Ho, F. Manns, J. M. Parel. Imaging and Full-Length biometry of the eye during accommodation using spectral domain OCT with an optical switch. Biomedical Optics Express 2012;3:1506-1520.

4. J. A. Mordi KC. Dynamic aspects of accommodation: age and presbyopia. Vision Research 2004;44:591-601.

5. C. M. Schor, Bharadwaj SR. A pulse-step model of accommodation dynamics in the aging eye. Vision Research 2005;45:1237-1254.

6. J. M. Parel, Gelender H, Trefers WF, Norton EWD. Phaco-Ersatz: cataract surgery designed to preserve accommodation. Graefe's archive for clinical and experimental ophthalmology 1986;224:165-173.

7. G. L. van der Heijde, Weber J. Accommodation used to determine ultrasound velocity in the human lens. Optometry and Vision Science 1989;66:830-833.

8. G. L. van der Heijde, A. P. A. Beers, Dubbelman M. Microfluctuations of steady-state accommodation measured with ultrasonography. Ophthalmic and Physiological Optics 1996;16:216-221.

9. W. Drexler, A. Baumgartner, O. Findl, C. K. Hitzenberger, Fercher AF. Biometric investigation of changes in the anterior eye segment during accommodation. Vision Research 1997;37:2789-2800.

10. R. Subramanian CC, M. Croft, K. L. De Paul, M. Neider, N. J. Ferrier, P. L. Kaufman, J. F. Koretz. Unilateral real-time Scheimpflug videography to study accommodation dynamics in human eyes. Investigative Opthalmology and Visual Science 2003;44.

11. J. F. Koretz, P. L. Kaufman, M. W. Neider, Goeckner PA. Accommodation and presbyopia in the human eye—aging of the anterior segment. Vision Research 1989;29:1685-1692.

12. J. F. Koretz, P. L. Kaufman, M. W N, Goeckner PA. Accommodation and presbyopia in the human eye. 1: Evaluation of in vivo measurement techniques. Applied Optics 1989;28:1097-1102.

13. I. Grulkowski MG, M. Sxkulmowski, I. Gorczynska, D. Szlag, S. Marcos, A. Kowalczyk, M. Wotkowski. Anterior segment imaging with spectral OCT system using a high-speed CMOS camera. Optics Express 2009;17:4842-4858.

14. M. Ruggeri, Extended Depth Optical coherence tomography for anterior segment and accommodation imaging in real-time. Biomedical Engineering. Miami, FL: University of Miami, 2011.

15. A. F. Fercher, W. Drexler, Hitzenberger CK, Lasser T. Optical coherence tomography-principles and applications. Reports on Progress in Physics 2003;66:239.

16. Brezinski ME, Fujimoto JG. Optical coherence tomography: high-resolution imaging in nontransparent tissue. Selected Topics in Quantum Electronics, Journal of IEEE 1999;5:1185-1192.

17. J.M. Schmitt, Optical coherence tomography (OCT): a review. Selected Topics in Quantum Electronics, Journal of IEEE 1999;5:1205-1215.

18. A. M. Rollins, Izatt JA. Optimal interferometer designs for optical coherence tomography. Optics Letters 1999;24:1484-1486.

19. Line Scan Camera Selector: Basler AG.

20. M. Wojtkowski, R. Leitgeb, A. Kowalczyk, A. F. Fercher, Bajraszewski T. In vivo human retinal imaging by Fourier domain optical coherence tomography. Journal of Biomedical Optics 2002;7:457-463.

21. Z. Hu, Y. Pan, Rollins AM. Analytical model of spectrometer-based two-beam spectral interferometry. Applied Optics 2007;46:8499-8505.

22. S. Yun, G. Tearney, J. de Boer, N. Iftimia, Bouma B. High-speed optical frequency-domain imaging. Optics Express 2003;11:2953-2963.

23. R. A. Leitgeb, C. K. Hitzenberger, A. F. Fercher, Bajraszewski T. Phase-shifting algorithm to achieve high-speed long-depth-range probing by frequency-domain optical coherence tomography. Optics Letters 2003;28:2201-2203.

24. C. Dai, C. Zhou, S. Fan, Z. chen, X. Chai, Q. Ren, S. Jiao, Optical coherence tomography for whole eye segment imaging. Optics Express 2012;20:6109-6115.

25. B. Potsaid, V. Jayaraman, J. G. Fujimoto, J. Jiang, P. J. S. Heim, Cable AE. MEMS tunable VCSEL light source for ultrahigh speed 60kHz-1MHz axial scan rate and long range centimeter class OCT imaging. SPIE BiOS: International Society for Optics and Photonics, 2012:82130M-82130M-8.

26. J. Jungwirth, B. Baumann, M. Pircher, E. Götzinger, C.K. Hitzenberger, Extended in vivo anterior eye-segment imaging with full-range complex spectral domain optical coherence tomography. Journal of Biomedical Optics 2009;14:050501-050501-3.

27. E. Götzinger, M. Pircher, R. Leitgeb, C.K. Hitzenberger CK. High speed full range complex spectral domain optical coherence tomography. Optics Express 2005;13:583-594.

28. B. Baumann, M. Pircher, C. K. Hitzenberger. Full range complex spectral domain optical coherence tomography without additional phase shifters. Optics Express 2007;15:13375-13387.

29. H. Wang, Y. Pan, Rollins AM. Extending the effective imaging range of Fourier-domain optical coherence tomography using a fiber optic switch. Optics Letters 2008;33:2632-2634.

30. Arduino Uno, 2014.

31. ATMEL. 8-bit AVR Microcontroller with 4/8/16/32K Bytes In-System Programmable Flash, Rev 8161D ed: Atmel, 2009.

32. S. R. Uhlhorn, D. Borja, F. Manns, J. M. Parel. Refractive index measurement of the isolated crystalline lens using optical coherence tomography. Vision Research 2008;48:2732-2738.

33. D. A. Atchison, G. Smith, Chromatic dispersions of the ocular media of human eyes. Journal of the Optical Society of America 2005;22:29-37.